



저작자표시-비영리-변경금지 2.0 대한민국

이용자는 아래의 조건을 따르는 경우에 한하여 자유롭게

- 이 저작물을 복제, 배포, 전송, 전시, 공연 및 방송할 수 있습니다.

다음과 같은 조건을 따라야 합니다:



저작자표시. 귀하는 원저작자를 표시하여야 합니다.



비영리. 귀하는 이 저작물을 영리 목적으로 이용할 수 없습니다.



변경금지. 귀하는 이 저작물을 개작, 변형 또는 가공할 수 없습니다.

- 귀하는, 이 저작물의 재이용이나 배포의 경우, 이 저작물에 적용된 이용허락조건을 명확하게 나타내어야 합니다.
- 저작권자로부터 별도의 허가를 받으면 이러한 조건들은 적용되지 않습니다.

저작권법에 따른 이용자의 권리는 위의 내용에 의하여 영향을 받지 않습니다.

이것은 [이용허락규약\(Legal Code\)](#)을 이해하기 쉽게 요약한 것입니다.

[Disclaimer](#)

공학박사 학위논문

**Characteristics of Hydrogen Negative
Ion Production depending on
Electron Energy Distributions
in Inductively Coupled Plasmas**

유도 결합형 수소 플라즈마에서 전자 에너지
분포에 따른 수소 음이온 생성 특성 연구

2015년 2월

서울대학교 대학원

에너지시스템공학부

허 성 렬

Characteristics of Hydrogen Negative Ion Production depending on Electron Energy Distributions in Inductively Coupled Plasmas

지도 교수 김 곤 호

이 논문을 공학박사 학위논문으로 제출함

2014 년 11 월

서울대학교 대학원

에너지시스템공학부

허 성 렬

허성렬의 박사 학위논문을 인준함

2014 년 12 월

위 원 장 _____ 황 용 석 (인)

부위원장 _____ 김 곤 호 (인)

위 원 _____ 정 승 호 (인)

위 원 _____ 노 태 협 (인)

위 원 _____ 정 경 재 (인)

Abstract

Characteristics of Hydrogen Negative Ion Production depending on Electron Energy Distributions in Inductively Coupled Plasmas

Sung-Ryul Huh

Department of Energy Systems Engineering

The Graduate School

Seoul National University

The goal of the RF driven hydrogen negative ion (H^- ion) source driver developments is to promote the generation of H^- ions and their precursors for a large extracted H^- ion beam current with a high RF efficiency. Without full understanding the underlying physics of the hydrogen plasma chemistry and the inductively coupled plasma (ICP), it cannot comprehend phenomena in RF H^- ion source drivers, then cannot also achieve this goal. To understand the underlying physics, the electron energy distribution function (EEDF) and H^- ion generation in low-pressure inductively coupled hydrogen plasmas is investigated using both theoretical and empirical approaches.

A global model was developed to investigate the densities of H^- ions and other species in a low-pressure inductively coupled hydrogen plasma with a bi-Maxwellian EEDF. Compared to a Maxwellian plasma, bi-Maxwellian plasmas have higher populations of low-energy electrons and highly vibrationally excited hydrogen molecules that are generated efficiently by the high-energy electrons. This leads to higher reaction rates of the dissociative electron

attachments responsible for H^- ion production. The model indicated that the bi-Maxwellian EEDF at low pressures is favorable for the creation of H^- ions.

The dual frequency antenna ICP was developed to bi-Maxwellize the EEDF by controlling the driving frequency-dependent collisionless heating. The dual frequency antenna ICP consists of a 2 MHz-driven solenoidal antenna wound around a cylindrical chamber and a 13.56 MHz-driven planar antenna placed on the top of it. Compared to the conventional single frequency antenna ICPs, the dual frequency antenna ICP reveals two distinctive characteristics, i.e., an increase in the power transfer efficiency and the bi-Maxwellization of the EEDF due to the collisionless heating. These characteristics allow the dual frequency antenna ICP to accomplish the enhanced generation of H^- ions and their precursors with a high RF efficiency.

In addition, the source pulsing for the enhancement of the volume H^- ion production was investigated by introducing the newly devised time derivative of EEDF – electron energy characteristic. The experimental result shows that H^- ion density in the after-glow is about 17 times of that in the active-glow. It was found that this is due to the electron cooling in the after-glow and the long lifetime of highly vibrationally excited molecules.

Keywords: hydrogen, plasma, inductively coupled plasma, negative ion, pulse, electron energy distribution function
Student Number: 2009-30262

*Dedicated to
my dear late grandfather who will be most proud of me when I complete my
Ph.D.
and to my faithful parents, grandmother, sister and in-laws who have
encouraged me with their endless love and have taught me the wisdom,
required to tackle challenges head on, that helped me to be what I am now
and to my beloved wife Hui-Chen Tsou whose amazing support, remarkable
patience and unwavering love provided me the strength I needed to
accomplish this work
and finally to him who always told me “Be thankful for what you have and
help others”.*

Contents

Chapter 1 Introduction	1
1.1 Historical review of RF hydrogen negative ion source.....	1
1.2 Aims and objectives	9
Chapter 2 Fundamentals	13
2.1 Production and destruction of H^- ion.....	13
2.2 H^- ion source configuration	18
2.3 Electron energy distribution function	22
2.4 Inductively coupled plasma	25
2.5 Plasma Diagnostics	47
Chapter 3 Modeling of an inductive coupled hydrogen plasma.....	61
3.1 Global model of a hydrogen plasma	61
3.2 Electromagnetic model of an ICP	82
3.3 Analytic model of collisionless heating.....	87
Chapter 4 The relation between H^- ion generation and EEDF	90
4.1 Experimental setup.....	90
4.2 Global model analysis of bi-Maxwellian H_2 plasmas.....	93

Chapter 5 H ⁻ ion generation enhanced by ICP heating.....	121
5.1 Experimental setup.....	122
5.2 Bi-Maxwellization of the dual frequency antenna ICP.....	126
5.3 H ⁻ ion generation enhanced by bi-Maxwellization.....	140
 Chapter 6 H ⁻ ion generation enhanced by pulsing.....	 143
6.1 Experimental setup.....	145
6.2 H ⁻ ion generation in a pulsed ICP.....	147
6.3 The optimum pulse condition for obtaining the maximum average H ⁻ ion density in repetitive pulsed ICPs.....	 165
 Chapter 7 Conclusion	 169
 Appendix A Floating harmonics method for determination of EEDF	 175
 Appendix B Laser-assisted H _α spectroscopy for measurement of H ⁻ ion density.....	 181
 Bibliography.....	 186
 Abstract	 198

List of Tables

Table 3.1	Volume and surface reactions for the model and their references.	65
Table 5.1	Calculated $T_{e, low}$, $T_{e, high}$, and β of EEDFs in the dual frequency antenna mode	136

List of Figures

Figure 1.1	Dependence of neutralization efficiencies for the positive and negative ions on beam energy, from [7].	6
Figure 1.2	Calculated relative reaction rates of the electron impact collisions and the heavy particle collisions in a hydrogen plasma at 2 mTorr pressure and 900 W ICP RF power.	10
Figure 1.3	Cross sections of major electron impact reactions in hydrogen plasmas and the normalized Maxwellian EEDF with an electron temperature of 7 eV. (DA: the dissociative electron attachment, ED: the electron detachment, VE: the vibrational excitation, IZ: the ionization, and DIZ: the dissociative ionization)	11
Figure 2.1	Negative ion current as a function of the work function of the plasma grid, from [25].	16
Figure 2.2	Schematic representation of the filament driven tandem multicusp H^- ion source as an example of the tandem source, from [7].	18
Figure 2.3	Electron temperature profile in the negative ion source with a magnetic filter, from [7].	20
Figure 2.4	(a) rod filter and (b) external filter, from [7].	21
Figure 2.5	An example of the bi-Maxwellian EEPF (black solid line) of $T_{e,low} = 7$ eV (70%) and $T_{e,high} = 20$ eV (30%) in Equation (2.3.6). The blue dashed line and the red dash-dotted line represent the EEPF parts of low-energy and high-energy electron groups, respectively. The black dotted lines are to display two slopes of the bi-Maxwellian EEPF curve.	24
Figure 2.6	Configuration of ICPs: (a) solenoidal antenna ICP (cylindrical source) and (b) planar antenna ICP, from [37].	26
Figure 2.7	RF impedance matching circuits: (a) the standard circuit and (b) the alternate circuit, from [38].	27
Figure 2.8	Radial distributions of the amplitude and phase of the RF magnetic field in a cylindrical argon plasma, from [39].	31
Figure 2.9	Schematic diagram of the transformer model of an inductive discharge. The secondary circuit has been transformed into its series equivalent in terms of the primary circuit current, from [37].	32
Figure 2.10	Frequency dependence of the H^- ion current, from (a) [42] and (b) [43].	34
Figure 2.11	Electron density at the equilibrium as a function of the coil current for three different driving frequencies, from [37].	36
Figure 2.12	Ratio of the absorbed total to collisional power absorption as a function of frequency. The experimental data are denoted by symbols and the theory is represented by curves, from [44, 45].	37

Figure 2.13 (a) EEPF versus electron energy for discharge power of 12.5, 50, and 200 W at a gas pressure of 1 mTorr. The solid, dashed, and dotted lines represent EEPFs at 13.56, 6.78, and 3.39 MHz, respectively. (b) EEPF versus electron energy for five frequencies at a discharge power of 200 W and a gas pressure of 1 mTorr. The E_c energies of EEPFs at 3.39, 6.78 and 13.56 MHz are 0.65, 2.5, and 9 eV, respectively, from [41].	39
Figure 2.14 Comparison of the EEPF measured in the driver region for two different source-operating parameters, from [21].	40
Figure 2.15 Schematic diagram on time modulation of the RF power envelope and plasma properties during the source pulsing, from [46].	43
Figure 2.16 Simulated phase-dependent I – V characteristics with a plasma potential oscillation of 10 V. The solid lines represent the I – V characteristic at different points in phase of the oscillation. The time-averaged trace \bar{I}_{avg} is shown by open circles while the effective DC I – V characteristic I_{dc} is shown by solid circles.	49
Figure 2.17 Equivalent circuit for the probe, sheath, and measurement system, from [50].	51
Figure 2.18 Illustration of harmonic generation caused by non-linear sheath impedance, from [47].	52
Figure 2.19 Average collected current plotted versus time and probe bias. Each line of constant probe bias corresponds to an ensemble average over 200 shots taken, from [51].	54
Figure 2.20 Schematic diagram of the boxcar sampling technique.	55
Figure 2.21 Photodetachment cross sections of H^- and C^- as a function of laser wavelength, from [53].	56
Figure 2.22 Variation of $\Delta n_{H^-}/n_{H^-}$, where Δn_{H^-} is the density of H^- ions destroyed by the photodetachment and n_{H^-} is the H^- ion density, with laser pulse energy, for three wavelengths of laser light, from [53]. The saturation of $\Delta n_{H^-}/n_{H^-}$ at energies above a modest level (>20 mJ/cm ²) is attributed to full photodetachment.	58
Figure 2.23 Cylindrical metal probe tip aligned parallel to the laser beam axis, electrically biased and drawing a conduction current from the plasma, from [53].	59
Figure 3.1 Schematic of the ICP. The plasma is contained in a dielectric tube of inner radius r_0 , outer radius r_c and length $l \gg r_0$. The tube is surrounded by a coil with N turns uniformly distributed, in which flows an RF sinusoidal current $I_{RF}(t) = Re[\tilde{I}_{RF}e^{i\omega t}]$, where \tilde{I}_{RF} is the complex amplitude and t is time. The induced electric field \tilde{E}_θ is azimuthal, while the induced magnetic field \tilde{H}_z is axial. At high plasma density, both fields decay within the skin depth δ , from [37].	82

Figure 3.2 Ampère contours for the current in the plasma (1), in the dielectric tube (2), and in the coil (3), from [37].	84
Figure 3.3 Variation of the normalized stochastic frequency as a function of the normalized frequency $w = (\omega c)/(\bar{v}_e \omega_{pe})$, from [120].	89
Figure 4.1 Schematic diagram of the inductively coupled hydrogen plasma, from [123].	91
Figure 4.2 Normalized EEPFs measured at different pressures (RF power: 900W).	93
Figure 4.3 The dependence of (a) the electron density, (b) the voltage drop across the presheath and sheath regions and (c) the electron density on pressure at 900 W. Symbols denote the experimentally measured data. (For (b) and (c), the solid lines indicate the model results obtained using the measured EEDFs including the bi-Maxwellian EEDFs in the low-pressure regime; the dashed lines indicates those under the assumption that EEDFs are Maxwellian.)	96
Figure 4.4 The dependence of (a) the neutral densities and (b) the atomic and molecular hydrogen density ratios on pressure at 900 W. (The solid lines indicate the model results obtained using the measured EEDFs including the bi-Maxwellian EEDFs in the low-pressure regime; the dashed lines indicates those under the assumption that EEDFs are Maxwellian.)	99
Figure 4.5 The relative reaction rates ($R_j/\sum_j R_j$) of the dominant volume and surface processes for (a) the generation and (b) the destruction of H atom as a function of pressure at 900 W. The absolute total reaction rate ($\sum_j R_j$) for the generation and destruction of H atom is given on the right side of Figure 4.5(a). Numbers on the graph denote the corresponding reactions listed in Table 3.1. (The solid lines indicate the model results obtained using the measured EEDFs including the bi-Maxwellian EEDFs in the low-pressure regime; the dashed lines indicates those under the assumption that EEDFs are Maxwellian.)	101
Figure 4.6 The dependence of (a) the normalized and (b) the absolute vibrationally excited H ₂ molecule density on the vibrational quantum number and pressure, at 900 W. (The solid lines indicate the model results obtained using the measured EEDFs including the bi-Maxwellian EEDFs in the low-pressure regime; the dashed lines indicates those under the assumption that EEDFs are Maxwellian.)	103
Figure 4.7 The dependence of the positive ion densities on pressure at 900 W. (The solid lines indicate the model results obtained using the measured EEDFs including the bi-Maxwellian EEDFs in the low-pressure regime; the dashed lines indicates those under the	

	assumption that EEDFs are Maxwellian.).....	105
Figure 4.8	The relative reaction rates of the dominant volume and surface processes for (a) the generation and (b) the destruction of H^+ ions as a function of pressure at 900 W. The absolute total reaction rate is given on the right side of Figure 4.8(a). Numbers on the graph denote the corresponding reactions listed in Table 3.1. (The solid lines indicate the model results obtained using the measured EEDFs including the bi-Maxwellian EEDFs in the low-pressure regime; the dashed lines indicates those under the assumption that EEDFs are Maxwellian.)	107
Figure 4.9	The relative reaction rates of the dominant volume and surface processes for (a) the generation and (b) the destruction of H_2^+ ions as a function of pressure at 900 W. The absolute total reaction rate is given on the right side of Figure 4.9(a). Numbers on the graph denote the corresponding reactions listed in Table 3.1. (The solid lines indicate the model results obtained using the measured EEDFs including the bi-Maxwellian EEDFs in the low-pressure regime; the dashed lines indicates those under the assumption that EEDFs are Maxwellian.)	110
Figure 4.10	The relative reaction rates of the dominant volume and surface processes for the destruction of H_3^+ ions as a function of pressure at 900 W. The relative reaction rate of the reaction No. 20 listed in Table 3.1 ($R_j/\sum_j R_j = 1$) is not plotted for reasons of convenience because the reaction No. 20 is the only considered reaction for the H_3^+ ion production. The absolute total reaction rate is given on the right side of the graph. Numbers on the graph denote the corresponding reactions listed in Table 3.1. (The solid lines indicate the model results obtained using the measured EEDFs including the bi-Maxwellian EEDFs in the low-pressure regime; the dashed lines indicates those under the assumption that EEDFs are Maxwellian.)	112
Figure 4.11	The dependence of (a) the negative ion density and (b) the central electronegativity on pressure at 900 W. (The solid lines indicate the model results obtained using the measured EEDFs including the bi-Maxwellian EEDFs in the low-pressure regime; the dashed lines indicates those under the assumption that EEDFs are Maxwellian.)	114
Figure 4.12	The relative reaction rates of the dominant volume and surface processes for the destruction of H^- ions as a function of pressure at 900 W. The relative reaction rate of the reaction No. 15 listed in Table 3.1 ($R_j/\sum_j R_j = 1$) is not plotted for reasons of convenience because the reaction No. 15 is the only considered reaction for the	

H⁻ ion production. The absolute total reaction rate is given on the right side of the graph. Numbers on the graph denote the corresponding reactions in Table 3.1. (The solid lines indicate the model results obtained using the measured EEDFs including the bi-Maxwellian EEDFs in the low-pressure regime; the dashed lines indicates those under the assumption that EEDFs are Maxwellian.)

(b) The ratio of the absolute dissociative electron attachment reaction rate (R_{DA}) for a Maxwellian EED and that for a Maxwellian EED as a function of the vibrational quantum number ($v = 3-14$) at 3 mTorr and 900 W..... 116

Figure 4.13 The dependence of negative ion density in the vicinity of the magnetic filter on pressure at 900 W. Symbols denote the experimental data measured using the laser photodetachment technique. (The solid lines indicate the model results obtained using the measured EEDFs including the bi-Maxwellian EEDFs in the low-pressure regime; the dashed lines indicates those under the assumption that EEDFs are Maxwellian.)..... 119

Figure 5.1 Schematic diagram of dual frequency antenna ICP. 122

Figure 5.2 Measured impedance $Z_{circuit}$ of the notch filter circuits in the probe at the harmonic frequencies of 2 and 13.56 MHz. 124

Figure 5.3 Electron densities versus total RF power in single and dual antenna modes in the ICP. In dual antenna modes, RF power of the solenoidal antenna is fixed at 2 kW and only RF power of the planar antenna is varied. Symbols denote experimental data measured, and the dash-dot ($P_{abs}/P_{total} = 1$) and solid line represents the global model result. 127

Figure 5.4 Dependence of the electron density on absorbed power by plasma in the ICP. (Frequency: 2 MHz, RF power: 2 kW, pressure: 5 mTorr, antenna current: 13 A, and electron temperature: 6 eV)..... 129

Figure 5.5 Dependence of collision frequencies, i.e., stochastic frequencies ν_{sto} for $\omega = 2$ MHz and 13.56 MHz, electron – neutral collision frequency ν_{en} , and electron – electron collision frequency ν_{ee} on electron density at 5 mTorr H₂. 131

Figure 5.6 Normalized EEPFs of (a) 2 MHz single frequency antenna mode at 2 kW (b) 13.56 MHz single frequency antenna mode at 4 kW and (c) dual frequency antenna mode at 6 kW (2 MHz 2 kW + 13.56 MHz 4 kW). 133

Figure 5.7 Normalized EEPF evolution with RF powers (a) at 2 MHz and (b) 13.56 MHz in the dual frequency antenna modes. 135

Figure 5.8 Dependence of EEDF shape on electron density and ratio of $P_{13.56 MHz}$ and $P_{2 MHz}$ 137

Figure 5.9 Critical electron density of the bi-Maxwellization in the dual

frequency antenna ICP as a function of pressure.	138
Figure 5.10 The dependence of (a) H atom density and (b) H ⁻ ion density on $P_{13.56\text{ MHz}}$ in the dual frequency antenna ICP. The red solid lines represent model results obtained using measured EEDFs involving bi-Maxwellian EEDFs in Table 5.1, and the black dashed lines correspond to those with the assumption that EEDFs are Maxwellian.....	141
Figure 6.1 Electron and negative ion densities as a function of time, during the discharge and in the after-glow, for different source operating pressures, from [141].....	144
Figure 6.2 Schematic representation of the experimental setup with diagnostics.	145
Figure 6.3 Temporal variation of (a) RF power, (b) electron current and (c) electronegativity at a pulse frequency of 1 kHz and a pulse duty cycle of 50%.....	148
Figure 6.4 Temporal variation of (a) electron temperature (the black solid line: experimental data and the blue dashed line: global model results), (b) electron density and H ⁻ ion density at a pulse frequency of 1 kHz and a pulse duty cycle of 50%.	149
Figure 6.5 Magnified version of Figure 6.4(b) at a pulse frequency of 1 kHz and a pulse duty cycle of 50%.....	150
Figure 6.6 Schematic diagram for explanation of the newly devised d(EEDF)/dt – electron energy characteristic.....	151
Figure 6.7 Experimental d(EEDF)/dt – electron energy characteristics at 2, 8.5, 14.5 and 40 μs after RF power is turned off.....	153
Figure 6.8 Schematic diagram of the diffusive cooling mechanism. Here, Φ is the potential, $r = 0$ is the radial position of the plasma center, and $r = a$ is the radial position of a wall in the cylindrical plasma system.	155
Figure 6.9 Temporal evolution of the critical confinement energy associated with the electron wall loss by the diffusive cooling at a pulse frequency of 1 kHz and a pulse duty cycle of 50%.	156
Figure 6.10 Temporal evolutions of the diffusive cooling rate (the blue solid line), the electron – neutral elastic collisional cooling rate (the grey dash-dotted line), and the reaction rate of the vibrational excitation (the $v = 1 \rightarrow v' = 2$ transition) as one of the major contributors to the electron – neutral inelastic collisional cooling (the navy dashed line) at a pulse frequency of 1 kHz and a pulse duty cycle of 50%.	158
Figure 6.11 Dependence of the absolute H ₂ (v) molecule density in the after-glow on the vibrational quantum number and time at a pulse frequency of 1 kHz and a pulse duty cycle of 50%.	161

Figure 6.12	Calculated reaction rates of major reactions for the generation and the destruction of H^- ions in the after-glow as a function of time.	163
Figure 6.13	Electron current – time characteristics at different (a) pulse frequencies and (b) pulse duty cycles. Here, $t = 0$ is the time when the RF power is turned on. The green vertical dashed line refers to the characteristic time when the electron current reaches a steady-state value at a pulse frequency of 1 kHz and a pulse duty cycle of 50%.	166
Figure A.1.1	The Maxwellian and non-Maxwellian EEPFs in a semi-logarithmic scale. (from Equation (A.1) for $T_{e, eff} = 3.3$ eV and $x = 0.5, 1, 2$) $x = 1$, $x < 1$ and $x > 1$ correspond to the Maxwellian, bi-Maxwellian-like and Druyvesteyn-like EEPFs, respectively.	176
Figure B.1	Schematic diagram showing the principle of laser-assisted H_α spectroscopy.	182
Figure B.2	Schematic diagram showing the definition of the spatial factor. (The blue region: V_{OES} , the red region: V_{int}).	184

Chapter 1. Introduction

1.1 Historical review of RF hydrogen negative ion source

Low-pressure hydrogen plasmas are widely utilized in the fields of material processing and semiconductor processing. For example, they are used for cleaning of silicon substrate surfaces, [1] etching, [2] and plasma immersion ion implantation of semiconductors. [3] In addition, the ion source is an important application of the hydrogen (or deuterium[†]) plasmas for the neutral beam injection (NBI) systems that heat the plasma and drive plasma currents in fusion reactors [4] and for the accelerators such as positron emission tomography cyclotrons and synchrotrons based research facilities. [5]

The development of ion sources containing hydrogen ions started by E. Goldstein in 1886. [6] In the 1940s, the radio frequency (RF) plasmas were investigated for ion beam production. The detailed history of the hydrogen ion source development is beyond the scope of this study. In order to maintain transparency and to be concise, this section is limited in scope: Only a brief review on development of the hydrogen ion sources, especially RF hydrogen negative ion sources, is presented.

According to the review of Hemsworth and Inoue, [7] the first multi-ampere positive ion source appeared in 1972, and soon began to be used on NBI

[†] Unless otherwise mentioned, all the statements associated with hydrogen can apply equivalently to the case of deuterium.

systems. In the beam injection systems for the heating and current drive of the magnetic fusion reactors, only neutral beams can be injected into the plasma regardless of the magnetic confinement fields. They then transfer their energy to the plasma through collisions. These neutral beams can be produced by the neutralizations of the accelerated hydrogen ion beams via collisions with gas molecules in the NBI neutralizer. The ion sources for the NBI play a role in providing a flux of hydrogen ions that will be accelerated in the beam extraction system and then neutralized in the neutralizer. In the late 1970s, investigation of the RF driven positive ion source for the NBI was started at the University of Giessen. [8] Here, the RF driven ion source usually means the inductively coupled plasma (ICP) as an ion source. The ICP is generated by an RF excited coil surrounding the dielectric wall (or window) of the source. The purpose of the investigation was to substitute the conventional filament driven arc discharge source by the RF driven ion source. The filament driven ion sources require regular maintenance to replace deteriorated filaments caused by evaporation. The RF driven ion sources, on the other hand, are free from the maintenance problem due to absence of the filaments. [4, 7–10] This makes the RF driven ion sources attractive for long pulse NBI systems (e.g., international thermonuclear experimental reactor (ITER) NBI). Furthermore, they have a simpler structure composed of fewer parts (i.e., an antenna coil and an RF matcher), resulting in cost savings. After many tests and research RF driven positive ion sources were developed at Max-Planck-Institut für Plasmaphysik (IPP) Garching and have been successfully operated for the NBI systems of fusion devices, i.e., axially symmetric divertor experiment upgrade (ASDEX

Upgrade) and Wendelstein 7 – advanced stellarator (W7–AS) since 1997. [8, 9] They are capable of maintaining the RF power more than 100 kW and four of them can deliver positive ion currents of 90 A in hydrogen (or 65 A in deuterium).

The proton fraction, defined as the ratio of the number of H^+ ions to the number of positive ions, is one of important considerations only for the development of positive ion sources for NBI systems. [7] This is attributed to the intrinsic characteristic that the hydrogen plasmas contain three positive hydrogen ion species, i.e., H^+ , H_2^+ , and H_3^+ .[†] During the neutralization process in the NBI neutralizer, the molecular ions accompany by the dissociation, and then the energy of the dissociated atoms or ions becomes either 1/2 or 1/3 of the original ion beam energy. Hence, H_2^+ and H_3^+ ions require twice and three times the accelerating voltage for H^+ ions in order to have a neutral beam as mono-energetic as possible. An increase in the accelerating voltage can easily cause technical difficulties involved in the high-voltage beam extraction system. Because lower accelerating voltage is desirable, achieving a higher proton fraction was a main goal in the development of positive ion sources.

In a historical review Bacal et al. [5] traces the history of the negative ion sources back to 1959 when the possibility of extracting hydrogen negative ions, H^- , directly from a duoplasmatron ion source was first reported by researchers

[†] For the development of negative ion sources for NBI systems, the ion density fraction does not have to be taken into account because there is only one negative ion species, H^- , in the hydrogen plasmas.

at Oak Ridge. In 1965, a H^- ion current of tens of mA was extracted at Los Alamos scientific laboratory. High H^- ion densities were measured in hydrogen plasmas of several laboratory devices at École Polytechnique in 1977. Those were meaningful observations that indicate the existence of an unknown volume production mechanism for generating H^- ions. Soon after, several possible new mechanisms were suggested. The volume production mechanism or reaction for the H^- ion production was finally identified as the dissociative electron attachment both theoretically and experimentally the next year. More recently (in 2005), the volume production mechanism was experimentally verified at Universität Duisburg-Essen with the aid of laser-induced fluorescence (LIF) spectroscopy.

The basic concepts of the volume H^- ion source (e.g., the tandem multicusp volume H^- ion source, the Penning volume H^- ion source, etc.) optimized for the volume production mechanism were developed after 1980. [5] The (filament driven) tandem multicusp volume H^- ion source is the most typical concept. The first example of tandem source using tungsten filaments was *Camembert II*. The extraction of H^- ions from a tandem multicusp volume H^- ion source was studied at Lawrence Berkeley national laboratory (LBNL) in 1983, and an extracted H^- ion current of 1.6 A, at a high operating pressure, in the volume ion source at Japan atomic energy research institute (JAERI) was reported in 1987.

H^- ions can be also produced by collisions of hydrogen atoms and ions with wall surfaces of low work function. [5, 7, 11–13] At institute of nuclear physics (INP) Novosibirsk in 1971, the discovery of cesiation (or cesium (Cs) seeding)

opened a new chapter in the development of the surface H^- ion source based on the surface production mechanism. By the cesiation, the attainable H^- ion currents increased dramatically. A large amount of research activity regarding the surface H^- ion sources (e.g., the magnetron, the Penning surface H^- ion source, the tandem multicusp surface H^- ion source, etc.) surged in the 1980s and 1990s. In 1989, LBNL reported an increase in H^- ion current by injection of Cs vapor into a tandem multicusp volume H^- ion source. Moreover, in their tandem multicusp surface H^- ion source[†], it was observed that the H^- ion current density maintained high even at a low operating pressure.

The surface H^- ion sources began to receive much attention from the fields of high performance NBI systems due to two reasons: First, the H^- ions in the NBI neutralizer have a higher neutralization efficiency at a very high beam energy compared to the hydrogen positive ions. Figure 1.1 shows the neutralization efficiencies for the positive and negative ions as a function of the beam energy.

[†] The hybrid H^- production ion source may be an appropriate name for the source because the surface-produced H^- ions are added to the volume-produced H^- ions in the strict sense.

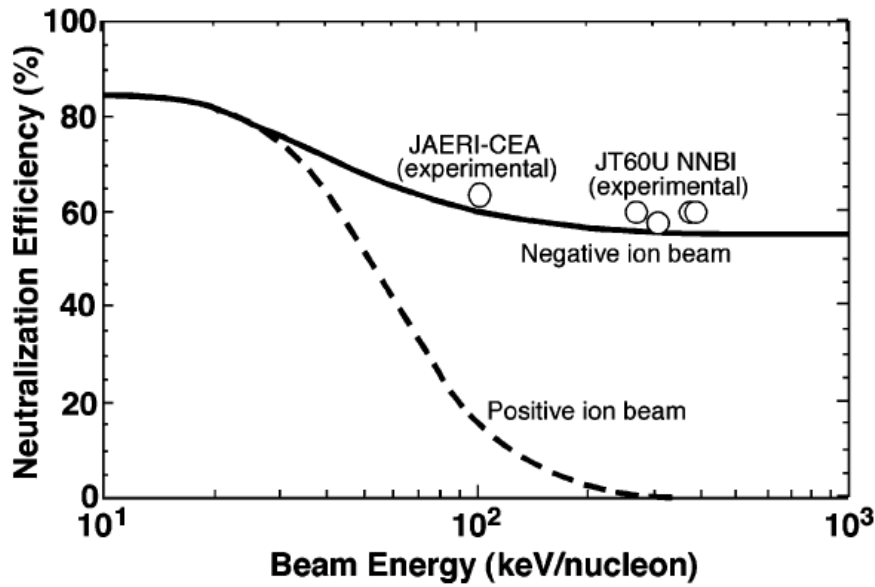


Figure 1.1 Dependence of neutralization efficiencies for the positive and negative ions on beam energy, from [7].

As an ion beam energy increases the neutralization efficiency of positive ions decreases and then becomes zero at 300–400 keV/nucleon. On the other hand, the efficiency of negative ions remains about 60 percent at energies greater than 200 keV/nucleon. [7, 14] For this reason, the negative ion based NBI (N-NBI) is highly necessary for fusion reactors that demand the high-energy neutral beam heating and current drive (e.g., ITER NBI: 1 MeV deuterium beam); second, the surface ion sources can easily achieve substantial H^- ion currents at a low operating pressure, compared to the volume ion sources. For N-NBI systems, a low pressure is required to keep stripping losses in the extraction system below acceptable levels. For example, the operating pressure of the ion source for ITER NBI should be 0.3 Pa or less. [7, 15]

In the 2000s, larger versions of the (filament driven) tandem multicusp surface H^- ion source were developed for the NBI systems of Japanese fusion devices. The KAMABOKO source at JAERI successfully produced H^- ion beams of 2 A (310 A/m^2) at an operation pressure of 0.1 Pa, which satisfies the requirements of the ITER negative ion source. The large ion sources running in NBIs for Japan torus – 60 upgrade (JT-60U) and large helical device (LHD) can currently produce more than 10 A of negative ions at low operation pressure of 0.3 Pa under cesiated conditions. [7]

The first RF driven H^- ion source was built at LBNL by converting a filament driven tandem multicusp volume H^- ion source in 1990. [5] Afterward other research institutes such as Oak Ridge national laboratory (ORNL), Deutsches elektronen-synchrotron (DESY), Seoul national university (SNU), IPP Garching also developed RF driven H^- ion sources. In particular, IPP Garching is deeply involved in the development of an ion source for the ITER NBI. Their development was started with much experience of RF driven positive ion sources in 1997. [8, 16] They initially considered the volume H^- ion source as a possible source that would meet the requirements of ITER NBI. However, it turned out that in this way it was difficult to achieve beyond a few mA/cm^2 . Since then, they have focused on the cesiated RF driven H^- ion sources to overcome the limits of volume H^- ion sources. The comparative advantages of the RF driven ion source over the filament driven ion source can apply equally to the cesiated H^- ion sources. Besides, the cesiated RF driven H^- ion sources have an additional advantage that Cs layer is not contaminated by the evaporation of filaments. The development programs at IPP Garching

progressed at three test facilities in parallel: (1) *Bavarian test machine for negative ions* (BATMAN) for optimization of current densities in hydrogen and deuterium at low pressure and electron/ion ratio, with a small extraction area and short pulses; (2) *multi ampere negative ion test unit* (MANITU) for long pulse (3600 s) operation test; (3) *re-use of the former radial injector of the decommissioned stellarator W7-AS* (RADI) for a size-scaling experiment on a half-size ITER plasma source. [4, 8, 9, 16–18] Since the tests were successful, the RF driven negative ion source was chosen by the ITER board as the reference source for the NBI of ITER in 2007. IPP Garching has recently developed a test facility *extraction from a large ion source experiment* (ELISE) for a feasibility study on the large-scale extraction of a negative ion beam, at ITER relevant conditions, using a half-size ITER RF source. [19, 20] RF driven H^- ion sources for NBI systems of *demonstration fusion power plant* (DEMO) and future fusion power plants require continuous operation. [5, 7, 13, 19] Unfortunately, the present cesiated RF driven H^- ion sources are not applicable to the continuous operation due to demanding challenges associated with Cs consumption. In this respect, the improvement of Cs management (i.e., a permanent Cs feed, a periodic cleaning of the ion source, and the measurement of the evaporated Cs flux) and development of Cs-free H^- ion source as an alternative to the present source have recently become major issues in this field of RF driven H^- ion source.

1.2 Aims and objectives

The source plasma region of the RF driven H^- ion sources, called the driver, ionizes, excites, and dissociates the gas, forming a plasma. [5, 7] It plays significant roles in providing both precursors of H^- ions and H^- ions themselves to the extraction region, whether the H^- ion source makes use of the volume production mechanism or the surface production mechanism. The ultimate goal of driver developments is to enhance both (1) the generation of H^- ions and their precursors for a large extracted H^- ion beam current and (2) the RF efficiency (defined as the extracted current per RF power). [19] However, optimizing the driver parameters, to achieve the goal, is not easy because ion sources have a complex nature that many physical and engineering design parameters of the ion sources are strongly related to each other. [21] Any change in one of these parameters induces a change in the others by the cause-and-effect relationship. The best way of overcoming this difficulty is to study the underlying physics of low-pressure hydrogen discharges and ICPs using theoretical and empirical approaches. It allows us to fully understand how the driver parameters affect the extracted beam current and hence to develop more efficient RF driven H^- ion sources. Therefore, in this work characteristics of low-pressure hydrogen plasmas including the H^- ion production and properties of ICPs associated with the RF efficiency are investigated, as a function of driver parameters, using a combination of experimental diagnostics, models and simulations.

Among the physical parameters mentioned above, the electron energy

distribution function (EEDF) is the most essential parameter to understand the underlying driver physics. Figure 1.2 shows the calculated relative reaction rates (defined as the reaction rate for a specific reaction per total reaction rate) of the electron impact collisions and the heavy particle collisions in a hydrogen plasma. It was obtained using the developed hydrogen plasma global model after-mentioned.

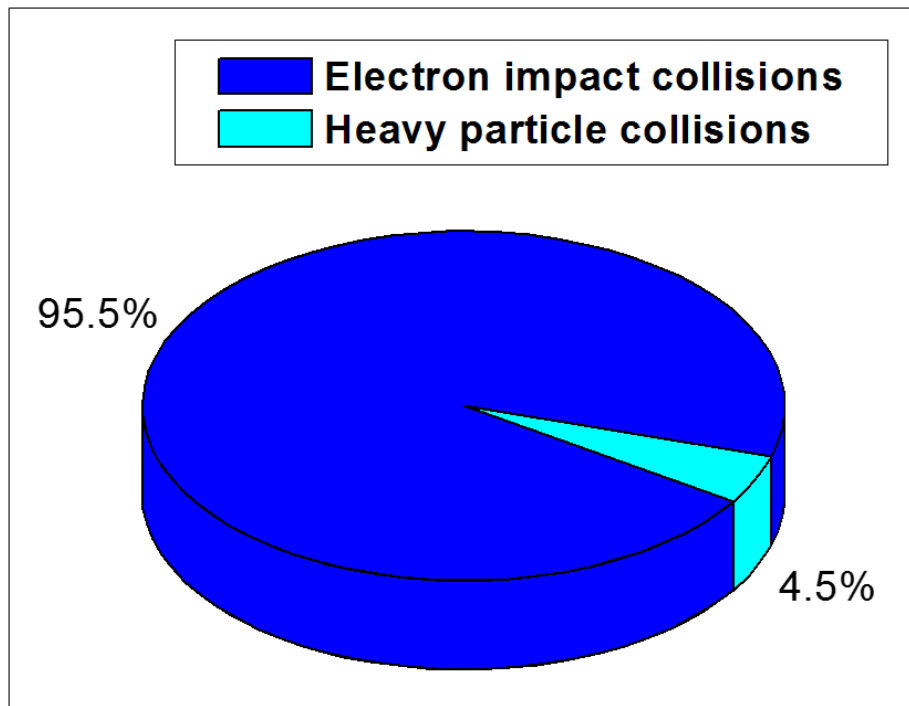


Figure 1.2 Calculated relative reaction rates of the electron impact collisions and the heavy particle collisions in a hydrogen plasma at 2 mTorr pressure and 900 W ICP RF power.

The contribution of the reaction rates of electron impact collisions to total

reaction rate is 95.5%, which indicates that electrons dominate almost all of collisions that take place in low-pressure hydrogen plasmas. Thus, the electrons are closely involved in the generation and destruction of H^- ions and their precursors, both directly and indirectly. The electron impact collisions relevant to H^- ions depend on the electron energy and have high rate constants in certain energy ranges due to intrinsic characteristics of their cross sections, as shown in Figure 1.3.

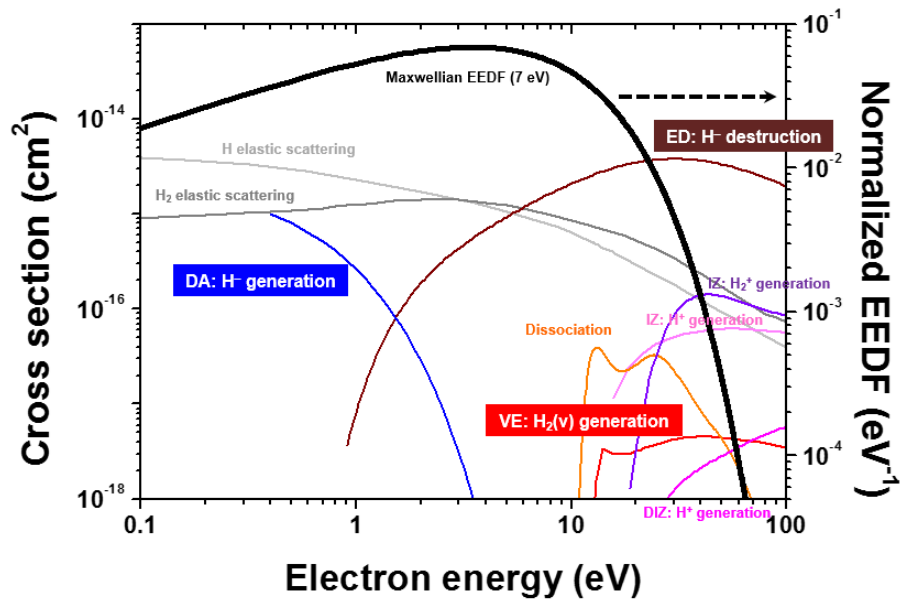


Figure 1.3 Cross sections of major electron impact reactions in hydrogen plasmas and the normalized Maxwellian EEDF with an electron temperature of 7 eV. (DA: the dissociative electron attachment, ED: the electron detachment, VE: the vibrational excitation, IZ: the ionization, and DIZ: the dissociative ionization)

Since the EEDF is also literally a function of energy, the shape of the EEDF

can affect considerably the generation and destruction reaction rates of H^- ions and their precursors. In other words, the H^- ion production is sensitive to changes in the EEDF shape.

Unfortunately, the influence of the EEDF in many previous research efforts for improving the H^- ion production was regarded as insignificant, but it is nevertheless important. Moreover, few studies, addressing the relationship between reaction kinetics of pure hydrogen plasmas and the EEDF in low-pressure ICPs, have been reported. In this study, in order to contribute to the development of more efficient RF driven H^- ion source drivers for widespread industrial and fusion applications,

- the reaction kinetics in hydrogen plasmas including H^- ion production depending on the EEDF, which is necessary to design and optimize the RF driven H^- ion sources, will be investigated.
- the physical natures of the power absorption and heating/cooling mechanisms to change EEDFs in ICPs will be understood using both theoretical and empirical approaches.
- a new concept of driver for more efficient RF driven H^- ion sources based on understanding of characteristics of low-pressure hydrogen plasmas and underlying physics of inductive discharges will be proposed.

Chapter 2. Fundamentals

In this chapter fundamentals of the inductively coupled hydrogen plasmas (i.e., the production and destruction processes of H^- ions, the configuration of H^- ion sources, and the electron kinetics in ICPs) and diagnostics related to this work will be briefly introduced and discussed in the following sections.

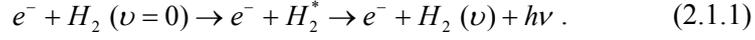
2.1 Production and destruction of H^- ion

2.1.1 Volume production of H^- ion

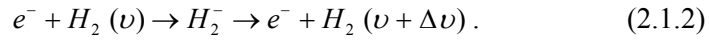
The volume production mechanism of H^- ions is a two-step process: (1) generation of highly vibrationally excited molecules and (2) production of the H^- ion by dissociative electron attachment. [7, 22] Typical volume H^- ion sources employ this process.

There are four identified reactions related with the production of highly vibrationally excited molecules, i.e., the vibrational excitation of hydrogen molecules (H_2) via the H_2^* state and H_2^- state, the recombination on the walls of molecular hydrogen ions, and the recombinative desorption of atomic hydrogens (H). The vibrational excitation of H_2 molecules via the H_2^* state (or E-V excitation) is an effective reaction pathway to create highly vibrationally excited molecules. In this reaction, highly vibrationally excited molecules are excited by collisions of ground state H_2 molecules with energetic electrons with energies of a few tens of eV, accompanied by radiative

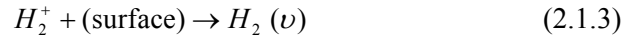
decay:



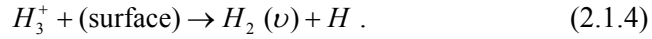
In contrast with the E–V excitation, the vibrational excitation of H_2 molecules via the H_2^- state (or e–V excitation) requires low-energy (< 5 eV) electrons and it is very effective in changing the vibrational states only at $\Delta\nu = \pm 1-2$. Thus, this reaction does not directly contribute to highly vibrationally excited molecules excited from the ground state or lowly vibrationally excited states of H_2 molecules. The reaction equation is as follows:



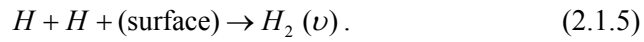
Two other reactions are surface-assisted processes. One is the recombination on the walls of H_2^+ and H_3^+ ions: [23, 24]



and



Its reaction rate is proportional to the densities and velocities of H_2^+ and H_3^+ ions and so the reaction may be more pronounced than the volume excitations, such as the E–V and e–V excitations, in low-pressure (sub-mTorr) and high-density plasmas. The other is the recombinative desorption of H atoms:



In general, this surface-assisted reaction depends upon the characteristics of the surfaces (i.e., structure, material, and temperature) and temperature of H atoms.

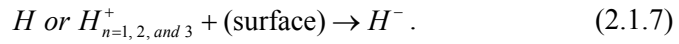
The last step of the volume production reaction of H^- ions is dissociative electron attachment (DA) to highly vibrationally excited molecules:



For this reaction, low-energy electrons are effective in generating H^- ions due to intrinsic characteristics of its cross section.

2.1.2 Surface production of H^- ion

Some of H atoms or positive ions impinging on a surface can be emitted as H^- ions: [22, 25, 26]



There are two types of surface H^- ion productions, i.e., thermodynamic equilibrium surface ionization and secondary negative ion formation (or non-thermodynamic equilibrium surface ionization). The essential of the surface production process of H^- ions is based on the electron tunneling from the surface to an atom (or ion) moving away from it. A low work function surface (e.g., a cesiated surface) is favorable for surface production of H^- ions, as shown in Figure 2.1.

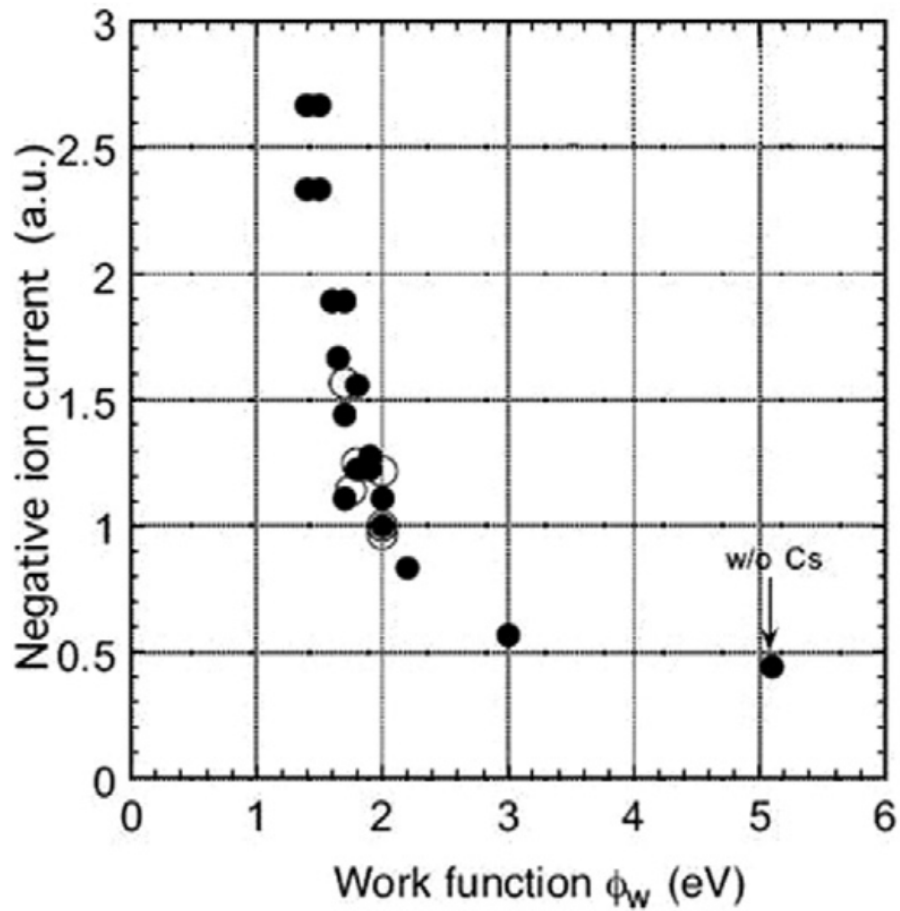


Figure 2.1 Negative ion current as a function of the work function of the plasma grid, from [25].

A minimum work function of about 1.5 eV can be obtained by the cesiation under plasma conditions. Additionally, for the H^- ion sources, the cesiation provides added advantages of decreasing the electron current and the optimum pressure.

2.1.3 Destruction of H⁻ ion

Three major volume destruction reactions are the mutual neutralization (MN), the electron detachment (ED), and the associative detachment (AD). [22] The MN in collision with positive ions is one of the dominant H⁻ ion destruction processes and its reaction equations are as follows:



and



The ED in collision with electrons,



has a low rate constant at a low electron temperature. Regardless of whether it is a volume H⁻ ion source or a surface H⁻ ion source, in order to prevent loss of H⁻ ions via ED, the electron temperature of a region near the extraction grid should be maintained at low temperature. This lowering the electron temperature (or reducing energetic electrons) can be achieved through the use of the magnetic filter after-mentioned. Lastly, the AD in collision with atoms is as follows:



2.2 H⁻ ion source configuration

The above-mentioned characteristics of H⁻ ion production and destruction mechanisms lead to the idea of a *tandem* source as a typical ion source. [5, 7] The tandem source usually consists of three regions, i.e., the driver region, the extraction plasma region, and the magnetic filter region, as shown in Figure 2.2.

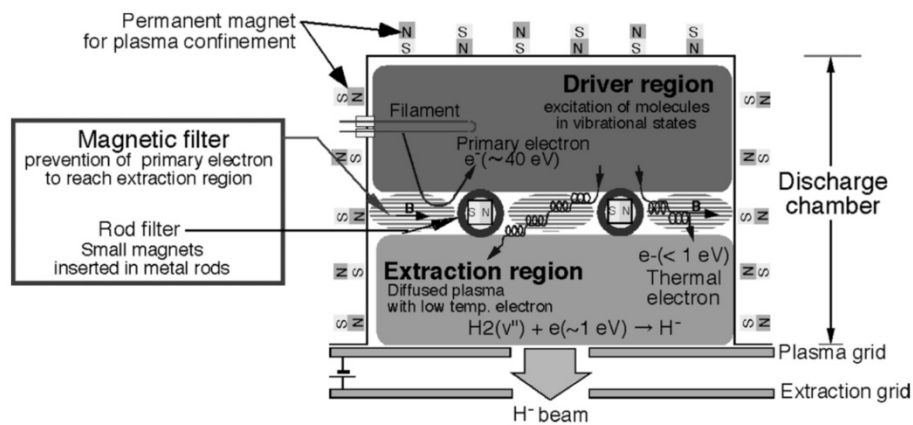


Figure 2.2 Schematic representation of the filament driven tandem multicusp H⁻ ion source as an example of the tandem source, from [7].

As briefly mentioned in chapter 1, the filament driven or RF driven ion source driver provides H⁻ ions and their precursors (i.e., highly vibrationally excited hydrogen molecules in the volume H⁻ ion sources and hydrogen atoms/ions in the surface H⁻ ion sources) to the extraction region. Reactions relevant to generation of the precursors, such as the E–V excitation, dissociation, and ionization, require a high electron temperature for high reaction rates. For this

reason, the electron temperature in the driver is higher than those in other regions.

The extraction region in front of the plasma grid is a plasma region containing negative ions that will be extracted by the grid system. The electron temperature in the extraction region should be low to reduce the H^- ion loss through ED.

As illustrated in Figure 2.2, the driver region and the extraction plasma region are generally separated by a magnetic filter. The magnetic filter formed of two or more parallel magnets produces a magnetic field perpendicular to the main plasma flow direction (or the discharge axis). This magnetic field allows only low-energy electrons and neutrals, except for high-energy electrons, to transfer from the driver region to the extraction region. For low-energy electrons, the electron transport through the magnetic filter is due to an $E \times B$ drift current on one side of the chamber induced by the presence of the chamber walls (or presheath) perpendicular to the diamagnetic ($\nabla P_e \times B$) current caused by electron pressure. [27–29] Figure 2.3 shows the electron temperature profile in the negative ion source with a magnetic filter. It is found that the electron temperature of the extraction region can be reduced, to a low level that ED occurs rarely, by the magnetic filter.

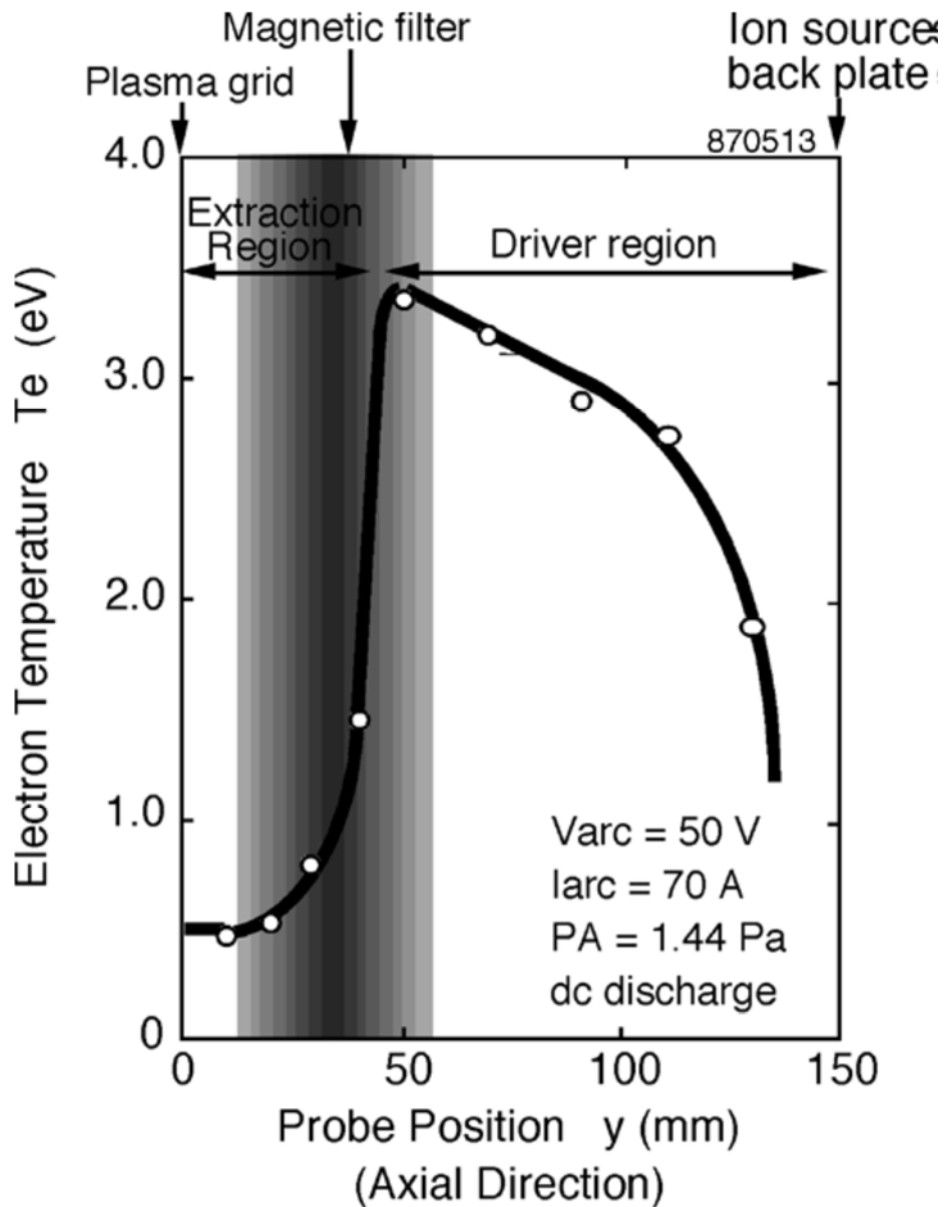


Figure 2.3 Electron temperature profile in the negative ion source with a magnetic filter, from [7].

The magnetic filter can be classified roughly into two types according to the

position of magnets: the plasma-immersed internal rod filter and the external filter, as shown in Figure 2.4.

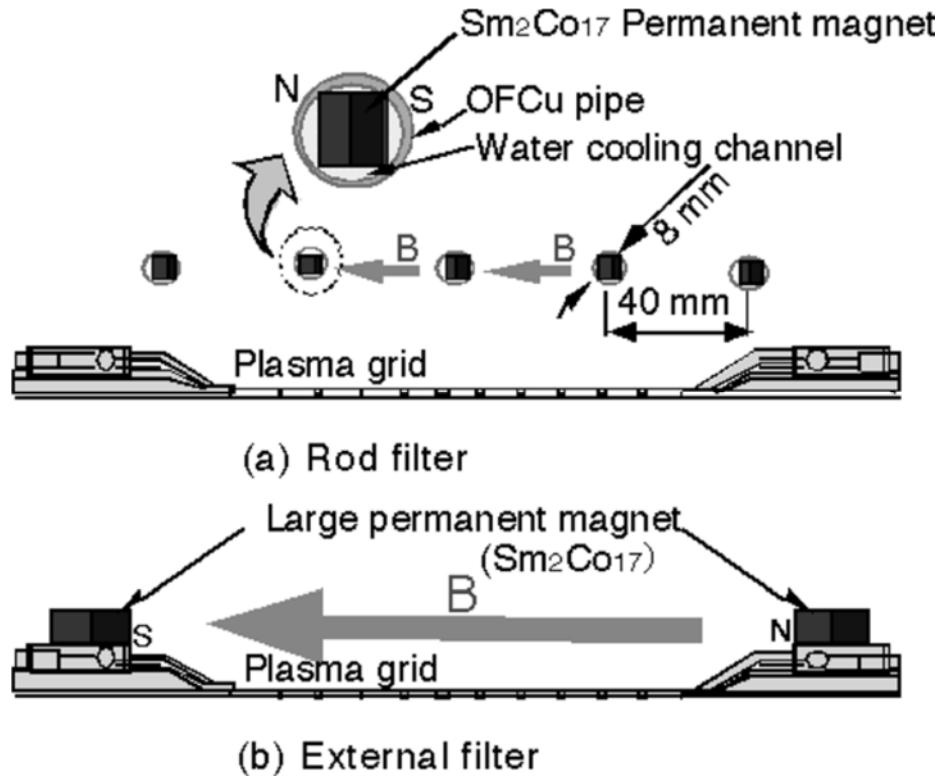


Figure 2.4 (a) rod filter and (b) external filter, from [7].

2.3 Electron energy distribution function

The EEDF in gas discharges is defined as population of electrons for a given energy, and its shape is mainly influenced by electron heating, transport, and collisions. EEDFs can be determined by solving the well-known Boltzmann equation: [30 – 32]

$$\frac{\partial f}{\partial t} + \mathbf{v} \cdot \nabla_r f + \frac{e}{m_e} (\mathbf{E} + \mathbf{v} \times \mathbf{B}) \cdot \nabla_v f = \left(\frac{\delta f}{\delta t} \right)_{coll} \quad (2.3.1)$$

where f is the electron distribution in 6-dimensional phase space, \mathbf{v} is the electron velocity, ∇ is the gradient operator, e is the elementary charge, m_e is the electron mass, \mathbf{E} is the electric field, \mathbf{B} is the magnetic field, t is time, and the term on the right side of the equation represents the rate of change in f due to collisions.

If a plasma is stationary, uniform and unmagnetized with a uniform steady \mathbf{E} and with elastic collisions between electrons and neutral gas atoms,

$$f = A \exp\left[-\frac{3m_e^3}{e^2 E^2 M} \int_0^v v' v_m^2(v') dv'\right], \quad (2.3.2)$$

where A is a normalization constant determined by $\int f d^3v = n_e$ (n_e : the electron density), M is the neutral mass, and v_m is the electron – neutral collision frequency. [33] For a constant v_m , f is a Maxwellian distribution:

$$f(\varepsilon) = c_A \varepsilon^{1/2} \exp\left(-\frac{1}{T_e} \varepsilon\right) \quad (2.3.3)$$

in the form of EEDF. Here, ε is the electron energy, c is constant, and T_e is the electron temperature in eV. When the cross section of the elastic collision

σ_m is constant and $v_m = n_g \sigma_m v$ (n_g : the neutral density), f is a Druyvesteyn distribution:

$$f(\varepsilon) = c_b \varepsilon^{1/2} \exp(-c_c \varepsilon^2). \quad (2.3.4)$$

For experiments, the EEDF reflects a state of electrons. The Maxwellian EEDF indicates that the electrons of the plasma are in thermodynamic equilibrium among each other. On the other hand, the non-Maxwellian (i.e., bi-Maxwellian and Druyvesteyn) EEDFs implies that electrons are not in equilibrium within their own ensemble. [34] The electron energy probability function (EEDF) is another expression of the EEDF for illustration purposes. EEDF in a semi-logarithmic scale shows the quick visualization of a dissimilarity of the measured EEDF from a Maxwellian distribution that is a straight line in the illustration. [35] The absolute value of the slope of the Maxwellian EEDF curve in a semi-logarithmic scale is the reciprocal of the electron temperature. When the velocity space is isotropic, the arbitrary normalized EEDF, $f_{\text{EEDF}} \equiv \varepsilon^{-1/2} f(\varepsilon)$, can be fitted as the generalized form: [36]

$$f(\varepsilon) = c_1 \exp(-c_2 \varepsilon^x). \quad (2.3.5)$$

Here, x is a parameter relevant to the electron energy distribution shape, $c_1 \equiv x[2\Gamma(\xi_2)/3T_{e, \text{eff}}]^{3/2}/[\Gamma(\xi_1)]^{5/2}$ and $c_2 \equiv [2\Gamma(\xi_2)/3T_{e, \text{eff}}\Gamma(\xi_1)]^x$ are functions of x and $T_{e, \text{eff}}$, where $\xi_1 \equiv 3/2x$, $\xi_2 \equiv 5/2x$, Γ is the gamma function, and $T_{e, \text{eff}}$ is the effective electron temperature in eV. This fitting formula is generally appropriate for Maxwellian and Druyvesteyn-like EEDFs ($x = 1-2$). In the case of bi-Maxwellian plasmas, the following fitting formula is much more suitable, compared to Equation (2.3.5):

$$f(\varepsilon) = c_{\text{low}} \exp(-\varepsilon / T_{e, \text{low}}) + c_{\text{high}} \exp(-\varepsilon / T_{e, \text{high}}), \quad (2.3.6)$$

where $T_{e, low}$ is the electron temperature (in eV) of the low-energy electron group, and $T_{e, high}$ is the electron temperature of the high-energy electron group. It is important to note that $T_{e, low}$ and $T_{e, high}$ in Equation (2.3.6) are different from electron temperatures obtained from the reciprocals of two slopes of the bi-Maxwellian EEPF curve, as illustrated in Figure 2.5.

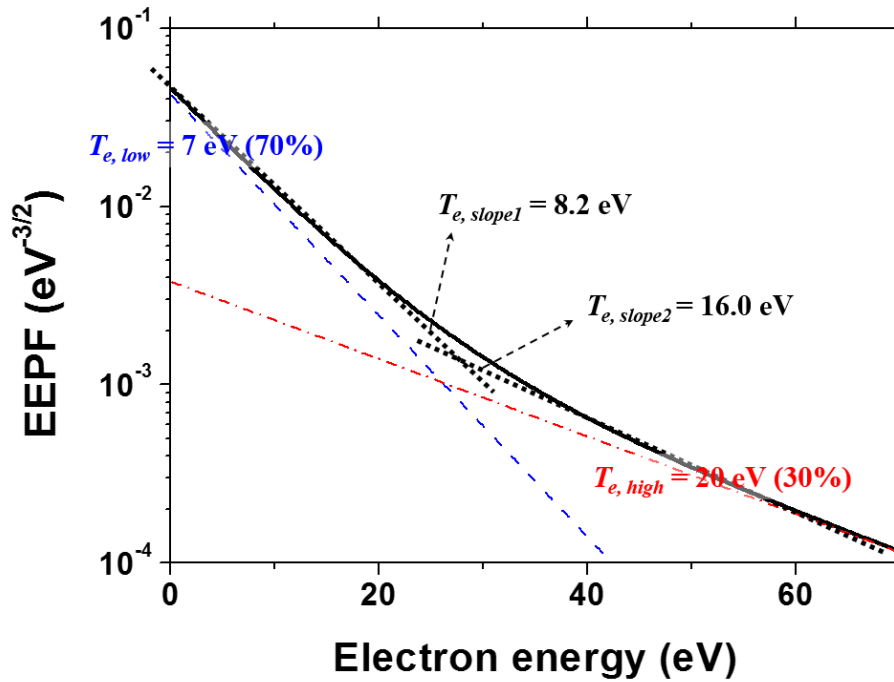


Figure 2.5 An example of the bi-Maxwellian EEPF (black solid line) of $T_{e, low} = 7$ eV (70%) and $T_{e, high} = 20$ eV (30%) in Equation (2.3.6). The blue dashed line and the red dash-dotted line represent the EEPF parts of low-energy and high-energy electron groups, respectively. The black dotted lines are to display two slopes of the bi-Maxwellian EEPF curve.

2.4 Inductively coupled plasma

Since J. Hittorf's discovery in 1884, ICPs have been widely used in the various industrial applications due to their simplicity and high efficiency. The RF driven H^- ion source driver is one of the important applications, and the ICP is ultimately compatible with its use in the driver. Compared to the ICP, other plasma sources (i.e., the filament driven arc discharge, the microwave discharge, the electron cyclotron resonance (ECR) discharge, and the capacitive coupled plasma (CCP)) for the application of the H^- ion sources have weaknesses as follows. The filament driven arc discharge sources cause the contamination by the evaporation of filaments, which is vulnerable to long pulse operation of the ion sources. The microwave and ECR discharges are less common for large-area ion sources than RF driven ion sources because they are more difficult to produce uniform large-area plasmas. In addition, the magnetic field in the ECR may be incompatible with a magnetic filter in the ion source. For high-density plasma sources, CCPs are typically less efficient than ICPs. CCPs also can suffer from the sputtering problem of their electrodes and the arcing problem between a high voltage electrode and an accelerator grid in the extraction region.

In the following subsections, the configuration, the power absorption, the heating mechanisms and the pulsed operation of ICPs, associated with the RF driven H^- ion source driver, will be discussed in detail.

2.4.1 ICP configurations

ICP reactors can be divided into two main geometric designs: the solenoidal antenna ICP and the planar antenna ICP, as shown in Figure 2.6. [37]

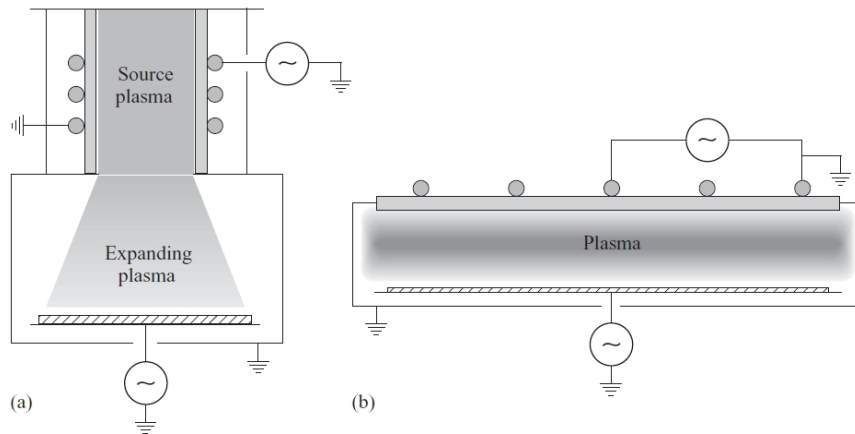


Figure 2.6 Configuration of ICPs: (a) solenoidal antenna ICP (cylindrical source) and (b) planar antenna ICP, from [37].

The solenoidal antenna ICP is generated by a coil that surrounds the cylindrical dielectric wall of the plasma source region. This type of plasma typically includes an expansion chamber where the substrate or the grid is placed. Most of RF driven H^- ion sources are based on it. Another configuration that is much used in the field of plasma is the planar antenna ICP. This configuration uses a flat spiral coil separated from the plasma by a flat dielectric RF window. The distance between the window and the substrate is generally smaller than the radius of the chamber.

In order to maximize the power transfer from an electrical power source (or the external RF power supply) to load (or the antenna coupled with a plasma), the impedance matching circuit, which is connected between the source and the load, is necessary. The two most common circuits are the standard circuit and the alternate circuit, as shown in Figure 2.7. [38]

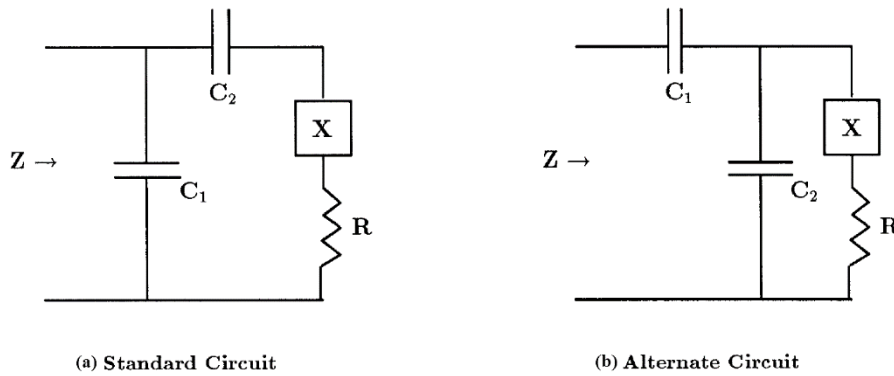


Figure 2.7 RF impedance matching circuits: (a) the standard circuit and (b) the alternate circuit, from [38].

In the figure, R is the load resistance, X is the load reactance, C_1 is the load capacitor, and C_2 is the tuning capacitor. The circuit is to have a net impedance Z_0 (usually $R_0 = 50 \text{ Ohm}$) to match the power supply and transmission line.

For a matching condition of the standard circuit, capacitances of the load and tuning capacitors are

$$C_1 = \frac{1}{2\omega R} \left[1 - \left(1 - \frac{2R}{R_0} \right)^2 \right]^{1/2} \quad (2.4.1)$$

and

$$C_2 = [\omega X - \frac{1 - R / R_0}{C_1}]^{-1}, \quad (2.4.2)$$

respectively. Here, ω is the angular wave frequency. The corresponding derivation is tedious but straightforward, and is skipped here for brevity. Note that C_1 depends only upon R , and is independent of X . If the load can be expressed as a purely inductive circuit (i.e., $X = \omega L$), there is a critical inductance,

$$C_2^{-1} = \omega^2 L - (1 - R / R_0) / C_1, \quad (2.4.3)$$

below which there is no matching condition. For large L value, C_2 depends only weakly upon L .

In the case of the matching condition of an alternate circuit, the solutions for the load and tuning capacitor's capacitances are

$$\omega C_1 = (R / R_0) / F \quad (2.4.4)$$

and

$$\omega C_2 = (X - F) / (X^2 + R^2), \quad (2.4.5)$$

respectively. ($F \equiv (R/R_0)^{1/2} [X^2 + R(R-R_0)]^{1/2}$) Compared to the standard circuit, the alternate circuit has a trade-off between the benefit of the reduced required C_1 and the risk of high voltage ratings on the capacitors.

2.4.2 Power absorption and heating mechanisms of ICPs

The principle of ICPs is to induce a plasma current by driving an RF current in an adjacent antenna coil. [37] RF power absorption of ICPs can be interpreted and understood as the interaction between an electromagnetic field and the plasma. Thus the nature of ICPs is nothing but the evanescent wave coupling

or the reactive near-field interaction between an antenna and a gaseous conductor medium. In the wave-coupled plasma region, the field around the antenna is sensitive to, and reacts to, the electromagnetic absorption. For the ICPs, the reactive region is known as the skin layer.

Heating mechanisms and electron kinetics of ICPs

In an oscillating electric field in the skin layer, a single electron in the plasma has a coherent velocity of motion that lags the phase of the electric field force by 90° . [39] Therefore, the time-averaged RF power transferred from the field to the electron is zero. Interparticle collisions (i.e., electron – other particles collisions) can destroy the phase coherence, resulting in a net transfer of power. This is the collisional or Ohmic heating mechanism, one of RF heating mechanisms. It dominates at high pressures because the interparticle collision rate is increased with pressure. When collisional heating mechanism is dominant, the electron thermal motion is generally negligible (i.e., cold electron plasma), and thus the RF current density \mathbf{J} is locally coupled with RF electric field \mathbf{E} : $\mathbf{J} = \sigma\mathbf{E}$, where σ is the local conductivity tensor of a cold plasma. Under these conditions, the electron kinetics are said to be local.

On the other hand, when mean free paths of electrons are comparable to the size of the discharge system due to thermal electrons, the electrons are not in either spatial or temporal equilibrium with the fields in the plasma. [39, 40] The thermal electrons may travel a distance comparable to the characteristic size of the discharge during one RF period, without experiencing a collision. Such

electrons interact with the fields at every point along their different trajectories, and the RF current is not a local function of the field (i.e., $\mathbf{J} \neq \sigma \mathbf{E}$) anymore. Therefore, \mathbf{J} at a given time in any volume element of the plasma depends upon the fields at every position \mathbf{x}' in the plasma and at all earlier times:

$$\tilde{\mathbf{J}}(\mathbf{x}) = \int_{-\infty}^{\infty} \Sigma(\mathbf{x} - \mathbf{x}') \tilde{\mathbf{E}}(\mathbf{x}') d\mathbf{x}', \quad (2.4.6)$$

where Σ is the non-local conductivity operator. This is a description of the non-local electron kinetics that is primarily observed in the low-pressure discharges. The required fundamental equations for obtaining a full picture of the non-local regime (e.g., the power absorption, electric field, and EEDFs) are the Maxwellian equations for fields and the Boltzmann equation for electron kinetics. Since all physical quantities of interest, such as the RF current density, are expressed in terms of integrals over the discharge volume and over past time, it is never easy to solve the equation sets.

The electrons in the non-local regime can lose phase coherence with the field due to their thermal motions, even in the absence of interparticle collisions. [39, 40] This is another RF heating mechanism called the collisionless or stochastic heating mechanism that dominates at low pressures. The principle of this mechanism is analogous to that of Landau damping of an electrostatic wave in a warm plasma. The collisionless heating often involves the anomalous skin effect. This effect is a result of the non-local interaction of electrons with fields. Unlike the classical skin effect that spatial decay of the electromagnetic field is exponential, the spatial decay under conditions that the anomalous skin effect exists is non-monotonic. It may have local maxima and minima in the plasma,

as shown in Figure 2.8.

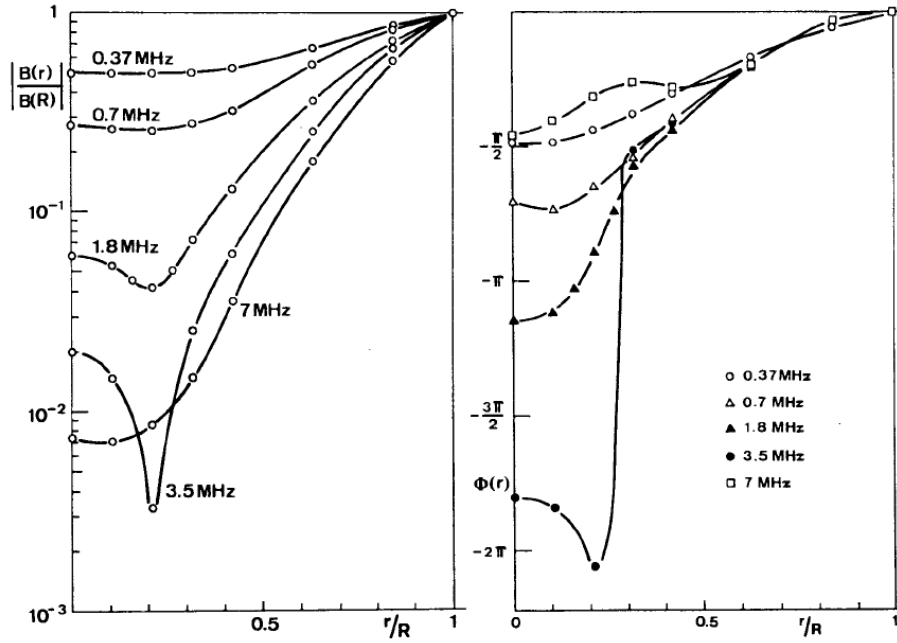


Figure 2.8 Radial distributions of the amplitude and phase of the RF magnetic field in a cylindrical argon plasma, from [39].

Power absorption of ICPs and frequency dependence

The characteristic parameters of ICPs, such as the power consumed in the plasma and the total impedance of an ICP system, can be determined using an electromagnetic model or a transformer model. [37] The electromagnetic model provides an analysis based on the calculated electromagnetic fields and RF currents in an ICP by solving Maxwell's equations. Though the electromagnetic model requires complex numerical analysis, its analysis is intuitive because the

nature of ICPs is the electromagnetic evanescent wave coupling, as mentioned earlier. The transformer model is a simplified decomposition of the electromagnetic model. In the model, an RF current loop in the plasma is regarded as the one-turn secondary coil of an air-cored transformer, and the primary coil is the antenna itself. This transformer analogy enables an easy calculation, but limits the applicable density range of the model. The analogy and the model are only satisfying in the high electron density regime. In the regime, the RF current is localized in a narrow skin layer and then the plasma indeed behave like a one-turn internal secondary coil. The electromagnetic model, on the other hand, can be applicable over the whole range of electron density since the electromagnetic fields are calculated regardless of the RF current is localized in the skin layer or not.

The Figure 2.9 shows the schematic diagram of the transformer model.

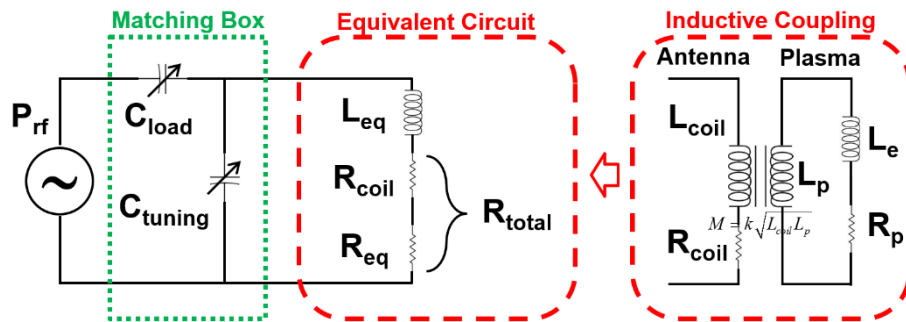


Figure 2.9 Schematic diagram of the transformer model of an inductive discharge. The secondary circuit has been transformed into its series equivalent in terms of the primary circuit current, from [37].

In Figure 2.9, the primary antenna coil has an inductance L_{coil} and a resistance R_{coil} , and the secondary plasma coil has two inductances due to the electron inertia L_e and the magnetic flux generated by the RF current loop in the plasma L_p and a plasma resistance R_p . The primary and secondary coils are coupled through the mutual inductance M . The coupled circuit can be transformed into an equivalent circuit composed of an inductance L_{eq} and a resistance R_{total} . Applying Kirchoff's laws gives

$$R_{total} = R_{coil} + R_{eq} \quad (2.4.7)$$

and

$$L_{eq} = L_{coil} - L_p (R_{eq} / R_p) - R_{eq} / \nu_m . \quad (2.4.8)$$

Recall that ν_m is the electron – neutral collision frequency. More details can be found in the textbook of Chabert and Braithwaite. [37]

In characterization of an ICP by power, the RF power delivered (incident minus reflected) by the RF generator P_{total} is the sum of the power dissipated by the antenna coil including connectors and cables P_{coil} and the power absorbed by the plasma electrons P_{abs} :

$$P_{total} = P_{coil} + P_{abs} = \frac{1}{2} R_{coil} I_{coil}^2 + \frac{1}{2} R_{eq} I_{coil}^2 , \quad (2.4.9)$$

where I_{coil} is the magnitude of the current in the coil. [41] P_{abs} is always smaller than P_{total} , and the power transfer efficiency, defined as P_{abs}/P_{total} , typically ranges between 10% and 90%. P_{abs}/P_{total} is usually low at low electron densities and low pressures, and in molecular and electronegative gases. It is important to note that P_{abs}/P_{total} is changed with the electron density and so P_{total} is not always linear to P_{abs} .

Unfortunately, as Godyak *et al.* pointed out, poor defined terms such as *ICP power*, *applied power*, *transmitted power*, *system power*, *nominal power*, etc. can be seen frequently in the literature. [41] This vague definition may yield misleading results in the interpretation of the ICP phenomena. Only P_{abs} , power absorbed by the plasma itself, is relevant to plasma parameters associated with phenomena occurring in the plasmas. Hence, to distinguish between P_{total} and P_{abs} is also crucial in the studies on the RF driven H^- ion source. In the reports of the frequency dependence of the H^- ion current by An *et al.* and Peters (see Figure 2.10), [42, 43] for example, the measurements should have been done while keeping P_{abs} or even electron density almost identical.

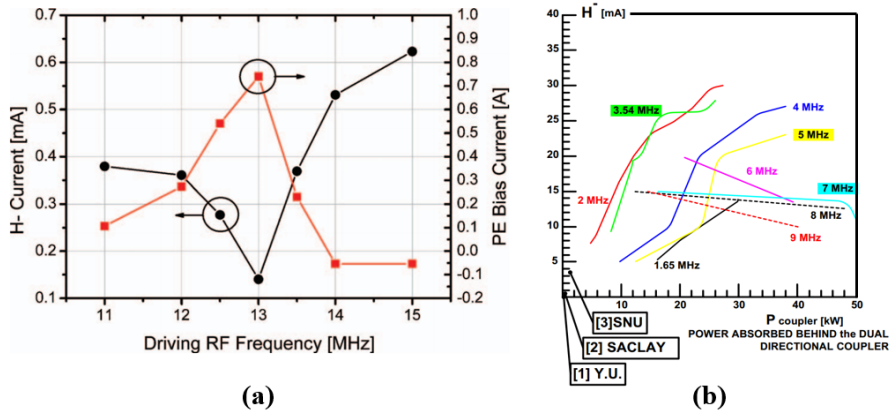


Figure 2.10 Frequency dependence of the H^- ion current, from (a) [42] and (b) [43].

The effect of different absorbed powers as well as the frequency effect might be reflected in the results in Figure 2.10. Unless theoretical analysis of P_{abs} or the frequency effect is involved in the interpretation of the experimental data, it is not easy to figure out the pure frequency dependence of the H^- ion current

underlying the tendencies. The frequency effect on the electron density in the ICPs will be reviewed in the following paragraph.

According to work of Godyak et al., [41] there is no practical frequency effect of the electron density with respect to the collisional power absorption. This can be explained as follows. As the frequency increases, the RF electric field in a skin layer where the electron heating process takes place is slightly increased, but the skin layer depth is also reduced. Consequently, the increase in the RF electric field is compensated by the shrinking the skin depth, which results in the unchanged power absorption in the skin layer and also the unchanged plasma parameters (e.g., electron density) determined by the ICP power balance. This argument was supported by results calculated using the transformer model combined with the power balance. [37] In the model, the collisionless power absorption was not taken into account. The equation for the electron density n_e as a function of I_{coil} in the low-pressure pure inductive discharges is given by

$$n_e = \left[\frac{\pi r_0 N^2 v_m (m_e / \epsilon_0)^{1/2}}{4u_B (h_l \pi r_0^2 + h_r \pi r_0 l) e \epsilon_T (T_e) c} \right]^{2/3} I_{coil}^{4/3}, \quad (2.4.10)$$

where r_0 is the radius of the cylindrical discharge volume, N is the number of turns in the solenoidal antenna coil, ϵ_0 is the permittivity of free space, u_B is the Bohm velocity, h_l is the planar dimensionless ion flux factor, h_r is the radial dimensionless ion flux factor, l is the length of the cylindrical discharge volume, ϵ_T is the total energy lost per electron – ion pair lost from the system, T_e is the electron temperature, and c is the speed of light. As can be seen from the Equation (2.4.9), I_{coil} is proportional to P_{abs} . Thus, Equation (2.4.10) also implies the correlation between n_e and P_{abs} . At fixed current, it is found that

there is no explicit dependence of n_e on the driving frequency. Figure 2.11 shows the $n_e - I_{coil}$ curves at three different frequencies, calculated using the model that takes into account the capacitive coupling in the ICP besides the inductive coupling.

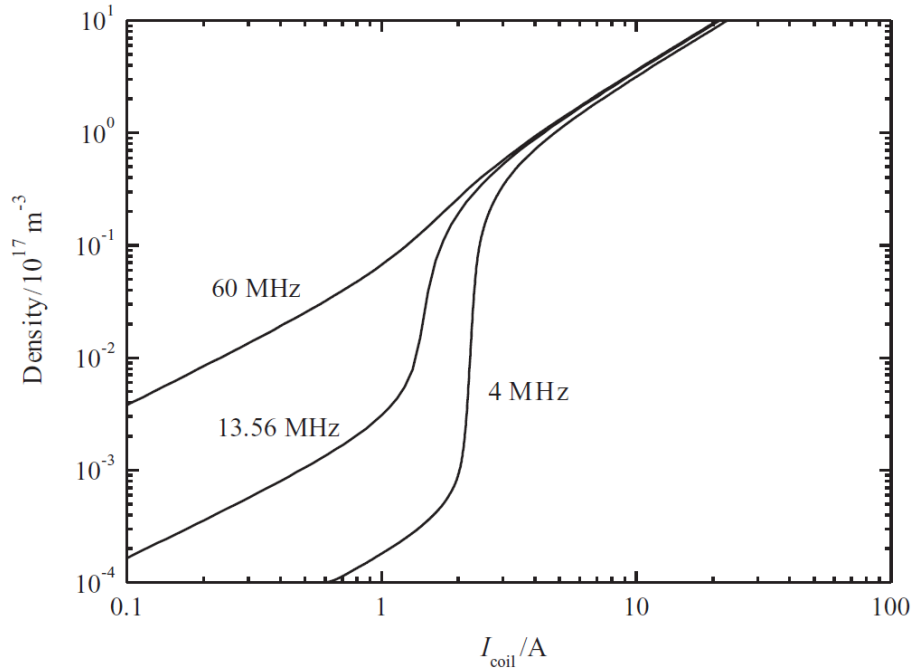


Figure 2.11 Electron density at the equilibrium as a function of the coil current for three different driving frequencies, from [37].

The frequency has almost no effect at high n_e (or high P_{abs}), where the inductive coupling dominates. This corresponds to the results calculated from Equation (2.4.10). By contrast, the frequency effect is remarkable when the capacitive coupling dominates at low n_e (or low P_{abs}).

Frequency dependence of collisionless power absorption in the low-pressure ICP has been reported by Godyak *et al.* [44, 45] Figure 2.12 shows the ratio of the absorbed total to collisional power absorption as a function of frequency.

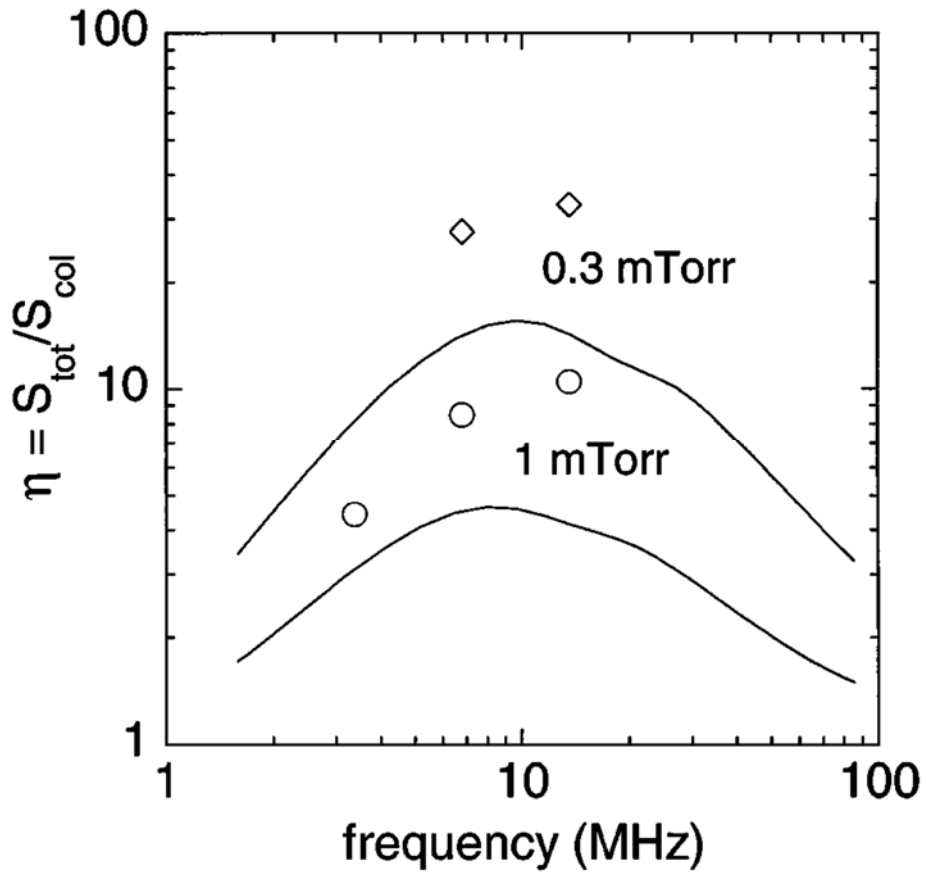


Figure 2.12 Ratio of the absorbed total to collisional power absorption as a function of frequency. The experimental data are denoted by symbols and the theory is represented by curves, from [44, 45].

Here, the absorbed total power represents the absorbed collisional power

absorption plus the absorbed collisionless power absorption. The ratio of the absorbed total to collisional power absorption is varied with frequency and it has a maximum value at a fixed pressure. Together with the fact that there is no practical frequency effect with respect to the collisional power absorption, this indicates that collisionless power absorption depends upon frequency. Actually, the appearance of the maximum ratio is ascribed to the resonant interaction of electrons with the RF field in the non-local regime. The resonance occurs when the half period of the field is approximately equal to the electron transit time through the skin layer: $\omega \approx v_{th}/\delta$, where v_{th} is the electron thermal velocity and δ is the skin layer depth.

EEDF in low-pressure ICPs

Frequency can affect the EEDF in low-pressure ICPs due to the collisionless resonant interaction, as mentioned above. [34, 41] The collisionless heating takes place when an electron crosses the skin layer in a fraction of the RF period. Only high-energy electrons ($E > E_c \approx m_e(\delta\omega)^2/2$, where E_c is the critical electron energy) can effectively gain energy, but low-energy electrons cannot. In addition, the ambipolar potential plays a role in confining the low-energy electrons as a barrier. The electrons with energies lower than the ambipolar potential energy cannot reach the skin layer where collisionless heating occurs. On the other hand, the high-energy electrons can pass through the barrier. Therefore, the collisionless selective electron heating of high-energy electrons plus the presence of the ambipolar potential barrier bring out the EEDF with a

non-equilibrium two-temperature structure in the elastic energy range, the so-called bi-Maxwellian EEDF. The bi-Maxwellian EEDF is a rather universal feature of low-pressure RF discharges as shown in Figure 2.13 (a).

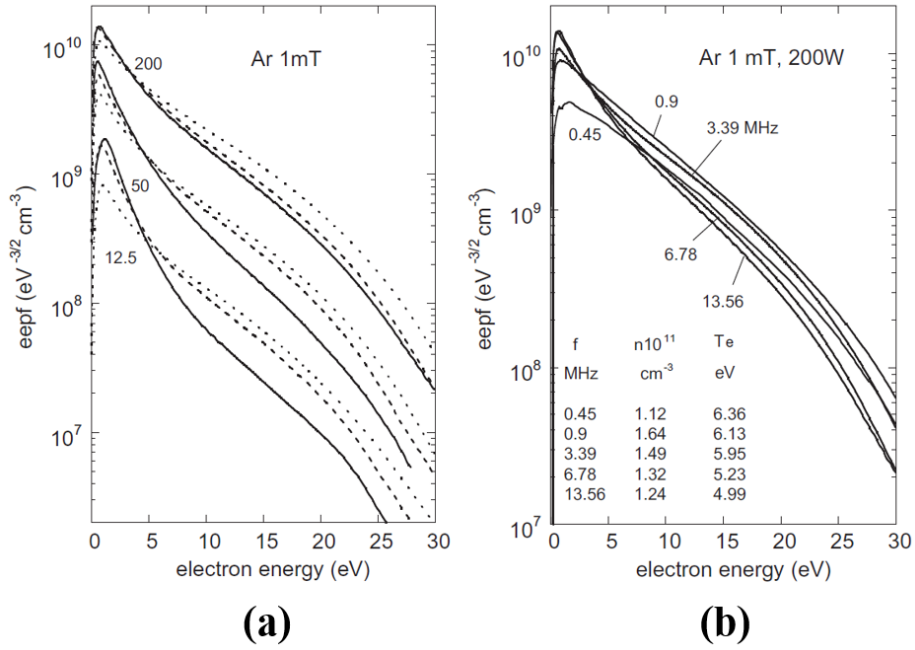


Figure 2.13 (a) EEPF versus electron energy for discharge power of 12.5, 50, and 200 W at a gas pressure of 1 mTorr. The solid, dashed, and dotted lines represent EEPFs at 13.56, 6.78, and 3.39 MHz, respectively. (b) EEPF versus electron energy for five frequencies at a discharge power of 200 W and a gas pressure of 1 mTorr. The E_c energies of EEPFs at 3.39, 6.78 and 13.56 MHz are 0.65, 2.5, and 9 eV, respectively, from [41].

Generally, the critical energy E_c corresponds to an onset in the anomalous collisionless electron heating and to a change in the EEDF or EEPF, as

illustrated in Figure 2.13 (b). The corresponding E_c energies of EEPFs at 3.39, 6.78 and 13.56 MHz are 0.65, 2.5, and 9 eV, respectively.

Godyak *et al.* argued that the knee of a bi-Maxwellian EEDF is smoothed (in other words, the EEDF is changed from the non-equilibrium bi-Maxwellian EEDF to the equilibrium Maxwellian EEDF) due to an increase in the electron – electron collision rate when the discharge power or pressure grows, as presented in Figure 2.13 (a). [41] However, in contrast to the results of work by Godyak *et al.*, McNeely *et al.* reported that a bi-Maxwellian EEPF appears even at a high power, as seen in Figure 2.14. [21]

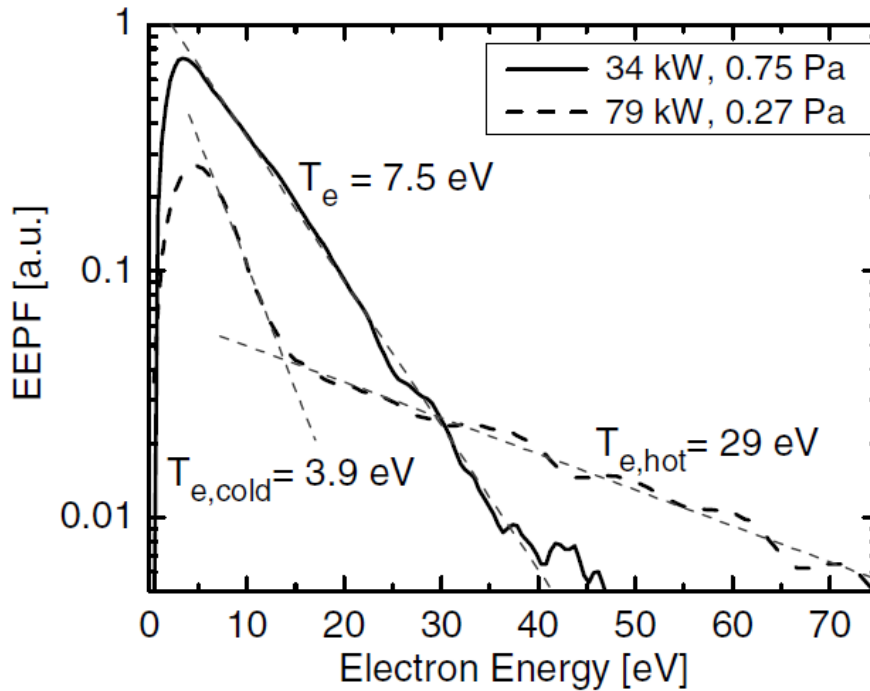


Figure 2.14 Comparison of the EEPF measured in the driver region for two different source-operating parameters, from [21].

They concluded that there is a competition between Maxwellizing caused by electron – electron collisions and de-Maxwellizing caused by the collisionless heating.

2.4.3 Pulsed operation

ICPs can operate at a constant average RF power or at a time-modulated RF power. The former operation is called the continuous wave (CW) RF mode and the latter, the pulsed RF mode. [46] The pulsed RF mode can increase the operation flexibility by enlarging the range of conditions for conventional CW RF mode. According to the review of Banna *et al.*, [46] there are two characterization parameters for the pulsed RF mode, i.e., pulse frequency and pulse duty cycle. The pulse frequency is the frequency at which the RF power is turned on and off per second, and the pulse duty cycle is the ratio between the pulse on-time and the total pulse duration. Together with conventional tunable knobs (e.g., RF power and gas flow) these two pulse parameters and optional phase lag between source and bias pulses, as new additional tunable knobs, allow the plasma properties such as ion/electron densities, electron temperature, dissociation and plasma potential to be controlled effectively. Moreover, compared to CW RF modes, the pulsed RF modes enable more independent controls of plasma properties that are strongly related to each other in the CW RF mode. The pulsed RF mode can be roughly classified into three types: source pulsing that only the source RF power is pulsed, bias pulsing that

only the bias power is pulsed, and synchronous pulsing that both source and bias powers are simultaneously pulsed with or without time delay between them. In this section, only source pulsing relevant to this work will be focused.

In contrast with the CW operation, wherein the plasma attains a quasi-steady-state, the pulsed plasma is truly transient. Figure 2.15 shows the schematic diagram on time modulation of the RF power envelope and its consequences, i.e. plasma properties during the source pulsing.

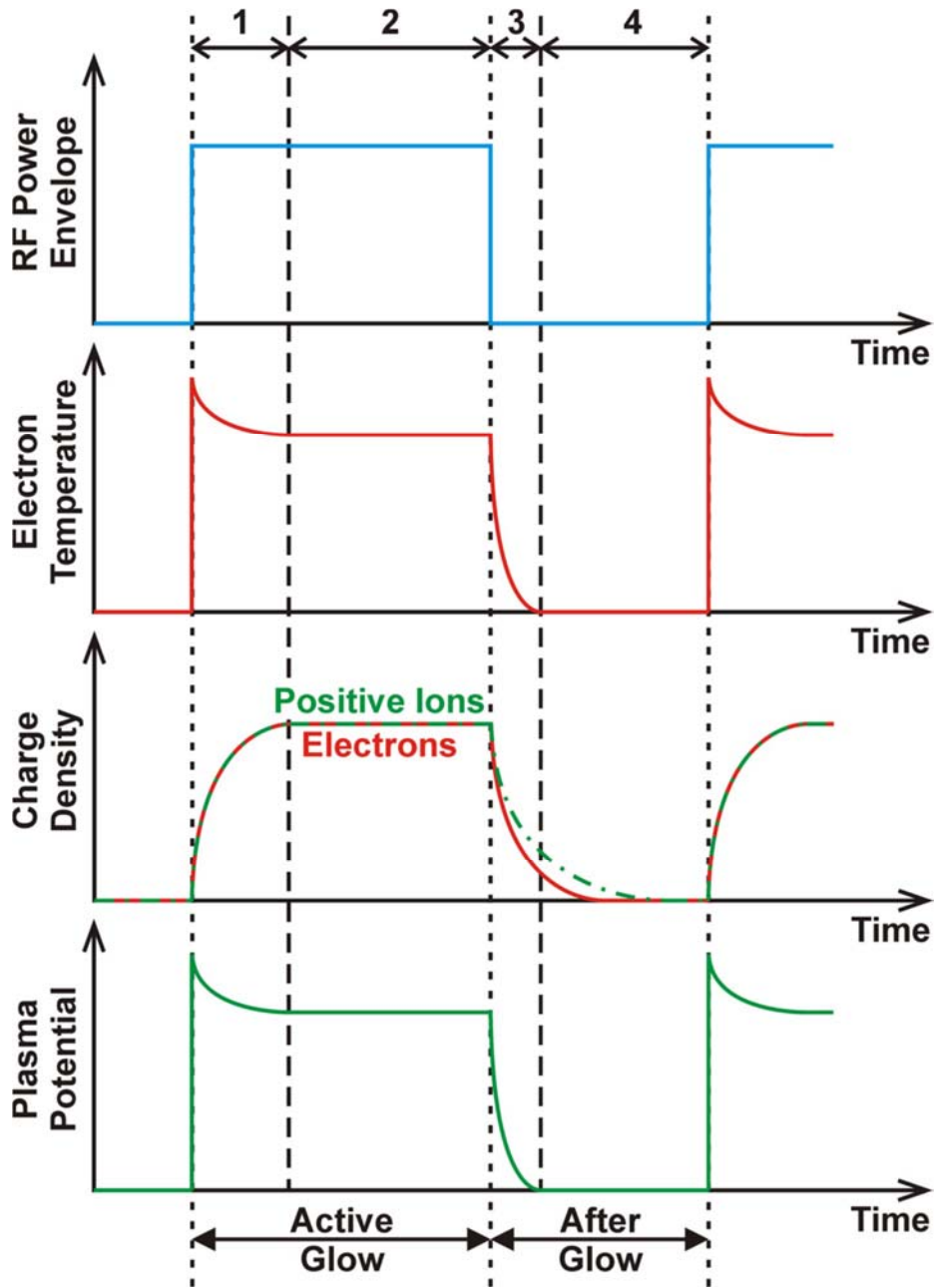


Figure 2.15 Schematic diagram on time modulation of the RF power envelope and plasma properties during the source pulsing, from [46].

Plasma properties in Figure 2.15 include electron temperature, density of positive ions and electrons, and the plasma potential[†]. Region 1 denotes to the initial active-glow period, 2 denotes to the steady-state active-glow period, 3 denotes to the initial after-glow period, and 4 denotes to the late after-glow period. The active-glow refers to the period when RF power is deposited, and the after-glow refers to the period when no power is deposited.

Initial active-glow

As RF power is instantaneously turned on, the plasma ignites and the electron/ion density begins to increase, but does not reach to a steady-state. Because the RF power deposition peaks and the electron density is low, the average energy of electrons or the electron temperature initially surges. Hence, the potential difference between a plasma and a floating wall, and the sheath voltage, which are proportional to the electron temperature, also rise.

Steady-state active-glow

The steady-state active-glow is, in principle, identical to the steady-state CW plasma. Therefore, the electron temperature, electron/ion density, and potential difference between a plasma and a floating wall in the steady-state active-glow has values that correspond to those measured in the CW RF mode. Note that

[†] In the strict sense, the plasma potential in Figure 2.15 is a misnomer. The potential difference between a plasma and a floating wall is more exact than that.

this period may not exist if RF power is turned off before plasma in the initial active-glow reaches to a steady-state. This is common for the cases at high pulse frequencies and low pulse duty cycles.

Initial after-glow

As RF power is instantaneously turned off, electrons are no longer heated. They dissipate their energy in collisions with other particles and by escaping to the walls. Consequently, the electron temperature decreases dramatically during this phase. The potential difference between a plasma and a floating wall also drops rapidly, and the sheath starts to collapse. At the same time, electrons and positive ions are transported to the surfaces or recombined. The decay rates of their densities are slower than that of the electron temperature. Interestingly, in the electronegative gas discharges, negative ion density increases rather than decreases during the period. As the H^- ions in the hydrogen discharge (mentioned above), negative ions in other electronegative gas discharges are also volume-produced by the dissociative electron attachment mechanism. Since the electron temperature is low during this period and the dissociative electron attachment is enhanced at low electron temperature, the formation of negative ions can be promoted. In addition to low electron temperature, the presence of the sheath voltage contributes to an increase in the negative ion density by confining the negative ions. This continues until the sheath has completely collapsed at the end of the initial after-glow.

Late after-glow

In this regime, electrons with energies close to thermal energies remain at their lowest level. The level depends upon the pulse frequency and the pulse duty cycle. In electronegative plasmas, ion – ion plasma (i.e., positive ion – negative ion plasma) is formed during this period because the dominant negatively charged species are the negative ions, not electrons. This is due to the fact that the electron loss, enhanced by the dissociative electron attachment and a higher mobility related to wall loss, is larger than the negative ion loss. Under such conditions, the sheath that arises from the mobility difference between the positively and negatively charged species (e.g., electrons and Ar^+ ions) is very thin.

2.5 Plasma Diagnostics

In this study, Langmuir probe diagnostics and the probe-assisted laser photodetachment technique are used for measurement of EEDF and its scalar integrals (i.e., electron temperature and electron density), and negative ion density in the plasma, respectively. In this section, the principles of these diagnostic techniques will be briefly reviewed.

2.5.1 RF compensated Langmuir probes

Ever since it was invented in 1924 by I. Langmuir, the Langmuir probe method has been extensively used for plasma diagnostics. [47] Langmuir probe is no more than a bare wire inserted into a plasma. [47, 48] By applying a variable bias voltage between the probe tip and the plasma, the current which depends on the bias voltage with respect to the plasma potential can be collected by the probe tip. From the current – voltage ($I - V$) characteristics, various plasma parameters can be obtained. The detailed interpretations of the $I - V$ characteristics to measure the electron temperature, electron and ion densities, floating potential, and time-averaged plasma potential can be found in the textbook of Hershkovitz. [48] The EEDF, one of the plasma parameters, can be attained[†] from the $I - V$ characteristic using the Druyvesteyn method:

[†] Another method developed by the author is presented in Appendix A.

$$f_{EEDF}(V) = \frac{2m_e}{e^2 A} \left(\frac{2eV}{m_e} \right)^{1/2} \frac{d^2 i_e}{dV^2}, \quad (2.5.1)$$

where m_e is the electron mass, e is the elementary charge, A is the area of the probe tip, i_e is probe electron current, and V is the probe voltage. [35] The double differentiation of the I – V characteristic in the method is delicate. Even small errors, after-mentioned RF fluctuations, and noises can result in huge distortion of the EEDF as a result of the noise-amplification effect of the differentiation process. [49] The electron density and the effective electron temperature can also be calculated by integrating the EEDF together with their definitions:

$$n_e = \int_0^{\infty} f_{EEDF}(\varepsilon) d\varepsilon \quad (2.5.2)$$

and

$$T_{e,eff} = \frac{2}{3n_e} \int_0^{\infty} \varepsilon f_{EEDF}(\varepsilon) d\varepsilon, \quad (2.5.3)$$

respectively. Here, $\varepsilon = \Phi_p - V$, where Φ_p denotes the plasma potential. [35]

When the Langmuir probe method is employed in the RF plasmas, difficulties relevant to the plasma oscillation arise. [47] The probe is swept by the oscillating plasma potential, $\tilde{\Phi}_p$, in an RF plasma. Since the oscillating frequency is usually in the mega-hertz range, the probe suffers many RF cycles at each direct (DC) bias point of the I – V characteristic, as illustrated in Figure 2.16.

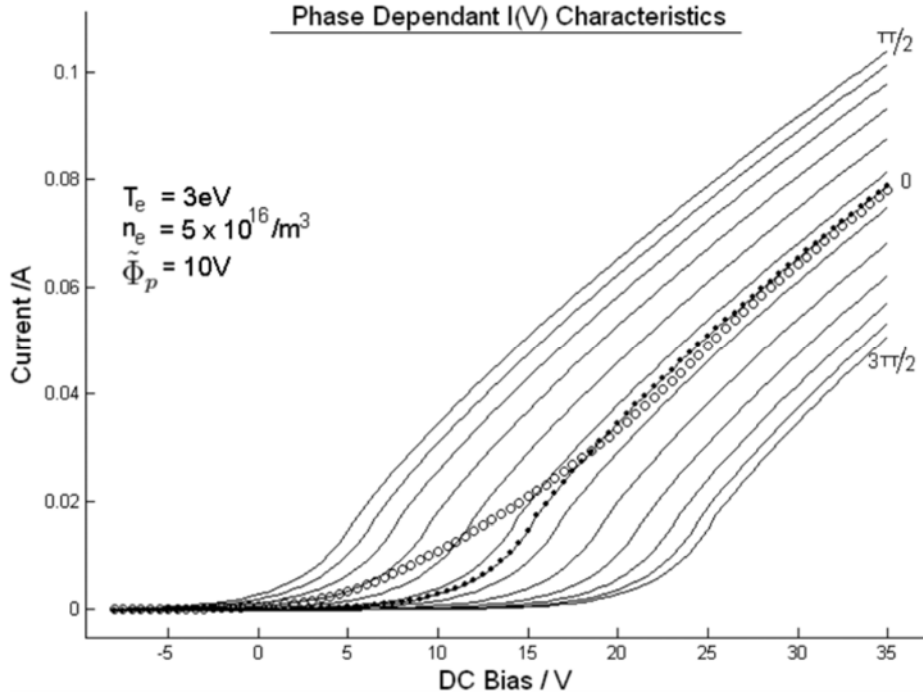


Figure 2.16 Simulated phase-dependent I – V characteristics with a plasma potential oscillation of 10 V. The solid lines represent the I – V characteristic at different points in phase of the oscillation. The time-averaged trace \bar{I}_{avg} is shown by open circles while the effective DC I – V characteristic I_{dc} is shown by solid circles.

Without an RF compensation technique, only the time-averaged trace \bar{I}_{avg} is measured by the probe. As seen in Figure 2.16, \bar{I}_{avg} is not equal to the effective DC ($t = 0$) characteristic I_{dc} due to the non-linear behavior of the I – V characteristic. An extra current component, $\Delta I(V) = \bar{I}_{avg}(V) - I_{dc}(V)$ causes a distortion. Moreover, this distortion gives rise to a more serious distortion in the EEDF through the double differentiation.

In an effort to compensate the distortion due to the RF fluctuation, several

methods that eliminate or reduce the amplitude of the oscillation across the probe sheath have been proposed. [35, 47, 50] One of the common methods is to use high impedance notch filter circuits. This idea is based on the RF oscillating voltage divider composed of components (i.e., the filter circuit and the probe sheath) connected in series. By letting the RF oscillating voltage primarily drop across the circuit, the probe sheath oscillates to a smaller extent. This leads to a smaller amplitude of RF oscillation in probe current and hence a smaller distortion. To achieve a negligible distortion, the impedance of the notch filter circuit $Z_{circuit}$ should be much larger than the probe sheath impedance Z_{sh} . The condition for the sufficient RF compensation is

$$|Z_{sh} / Z_{circuit}| < (0.3 \sim 0.5) T_e / \tilde{\Phi}_p. \quad (2.5.4)$$

However, in practice, the impedance of the notch filter circuit is largely reduced by the inherent parasitic (or stray) capacitance. To fulfil the above requirement, taking into account the stray capacitances, a compensation electrode (or an auxiliary floating electrode or a shunting electrode) can be employed. The compensation electrode, which is shunt connected to the probe tip via a DC blocking capacitor, has a surface area larger than the probe tip area. While it does not affect the measured DC probe current because of the DC blocking capacitor, it effectively decreases Z_{sh} due to its large area and parallel connection to the probe tip, resulting in a reduction of the required $Z_{circuit}$. Figure 2.17 shows the equivalent circuit of the probe, sheath, and associated circuitry. [50]

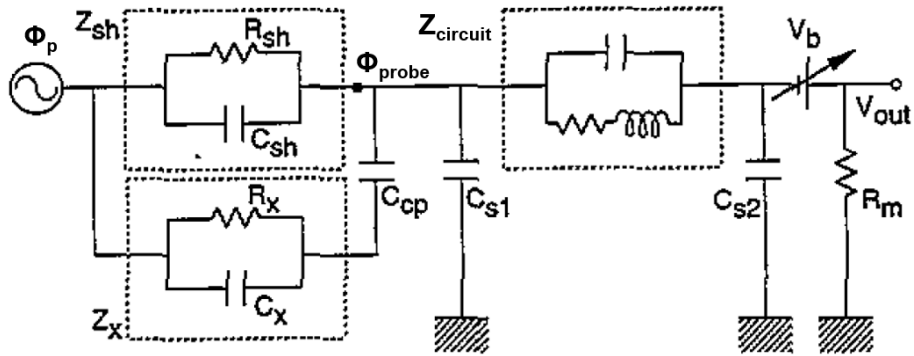


Figure 2.17 Equivalent circuit for the probe, sheath, and measurement system, from [50].

Here, Φ_p is the plasma potential, Φ_{probe} is the potential of the probe tip, V_b is the probe bias voltage, and V_{out} is the output voltage across the current measuring resistor R_m . The probe sheath impedance Z_{sh} consists of an equivalent resistance R_{sh} in parallel with an equivalent capacitance C_{sh} . The notch filter circuit is represented by an impedance $Z_{circuit}$. The small stray capacitance C_{s1} is that of the short lead between the notch filter circuit and the probe tip and large stray capacitance C_{s2} is that of the power supply and all the connecting cables. The compensation electrode has an impedance Z_x consisting of R_x in parallel with C_x , and is coupled to the probe tip by the DC blocking capacitor C_{cp} .

It is recommended that the notch filter circuit has high impedances at several harmonic frequencies of the RF oscillation as well as the fundamental frequency. As seen in Figure 2.18, the collected probe current by applying a sinusoidal RF voltage oscillation is non-sinusoidal due to non-linear behavior of the plasma sheath. [47]

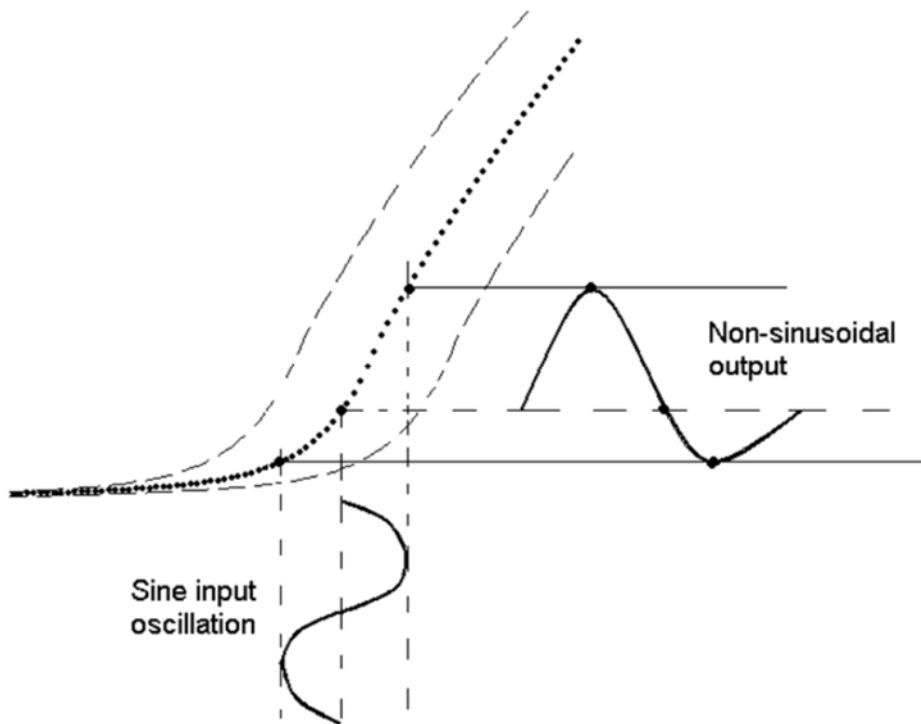


Figure 2.18 Illustration of harmonic generation caused by non-linear sheath impedance, from [47].

It implies that currents of higher harmonic frequencies can be produced from a Fourier analysis point of view. Accordingly, in order to alleviate the RF fluctuation harmonics, the common notch filter circuit consists of filters connected in series with high impedances at the first several harmonics. Each of the filters satisfies the requirement of Equation (2.5.4) for the corresponding frequency.

In addition to the RF fluctuation, there is another obstacle related to the probe circuit resistance. [35] If the probe circuit resistance including R_m and a real resistance component of $Z_{circuit}$, $R_{circuit}$, is comparable to or larger than R_{sh} in

Figure 2.17, a DC bias voltage with respect to the plasma potential, V of the I – V characteristic, is no longer a voltage drop across the probe sheath due to a voltage drop across the probe circuit resistance. It results in an enormous depletion of low-energy electrons in the EEDF or EEPF. This large EEPF distortion in its low-energy range is called the Druyvesteynization effect. Consequently, besides the requirement of Equation (2.5.4), the notch filter circuit should satisfy the requirement that the sum of $R_{circuit}$ and R_m be much smaller (about one hundred times smaller) than the minimum value of R_{sh} , in order to suppress the Druyvesteynization effect and to obtain acceptable EEPFs.

2.5.2 Time-resolved Langmuir probes

The time-resolved Langmuir probe diagnostics is to measure the averaged collected current as a function of two independent variables; time t and probe bias voltage V_b , i.e., $I(V_b, t)$. [51] Generally, the boxcar sampling technique has been used to measure I – V characteristics at a specific time t^* : $I(V_b, t = t^*)$. The process is as follows: First, at a fixed probe bias voltage V_{bl} ($V_b = V_{bl}$), the probe current is measured at many different times and then averaged to obtain $I(V_{bl}, t)$. Since V_b is fixed while collecting $I(V_{bl}, t)$ the plasma always has sufficient time to equilibrate with the probe, leading to improved signal-to-noise ratio and good time resolution. Next, first step is repeated for all probe bias voltages over the range of interest. (e.g., $I(V_{b2}, t)$, $I(V_{b3}, t)$, $I(V_{b4}, t)$, ... are obtained.) Last, the only data of $I(V_b, t)$ at the specific time t^* is extracted from all accumulated data of $I(V_b, t)$, (see Figure 2.19) and then sorted in ascending order of V_b to obtain

$$I(V_b, t = t^*).$$

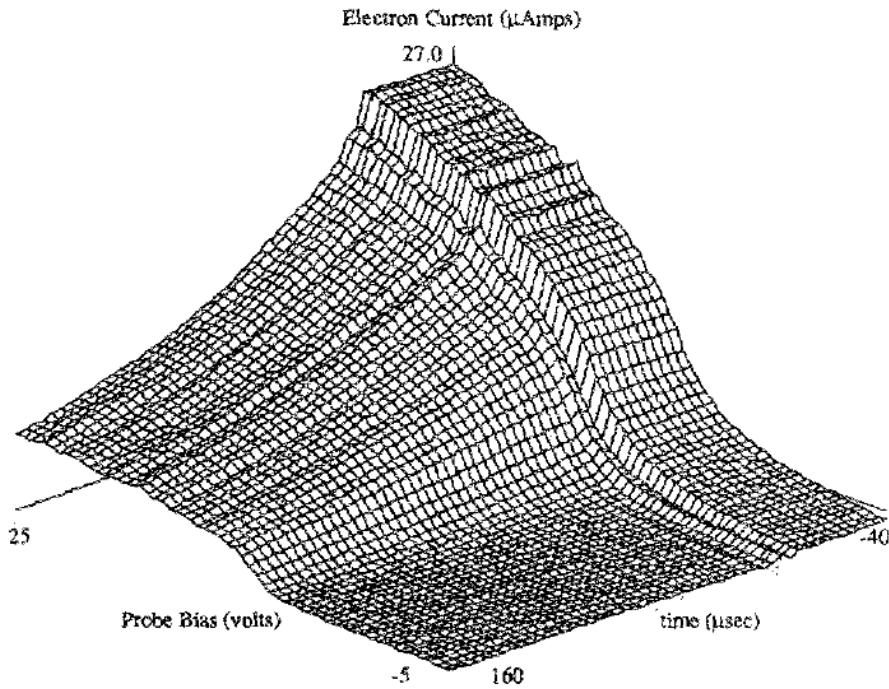


Figure 2.19 Average collected current plotted versus time and probe bias. Each line of constant probe bias corresponds to an ensemble average over 200 shots taken, from [51].

The schematic diagram of this process is shown in Figure 2.20.

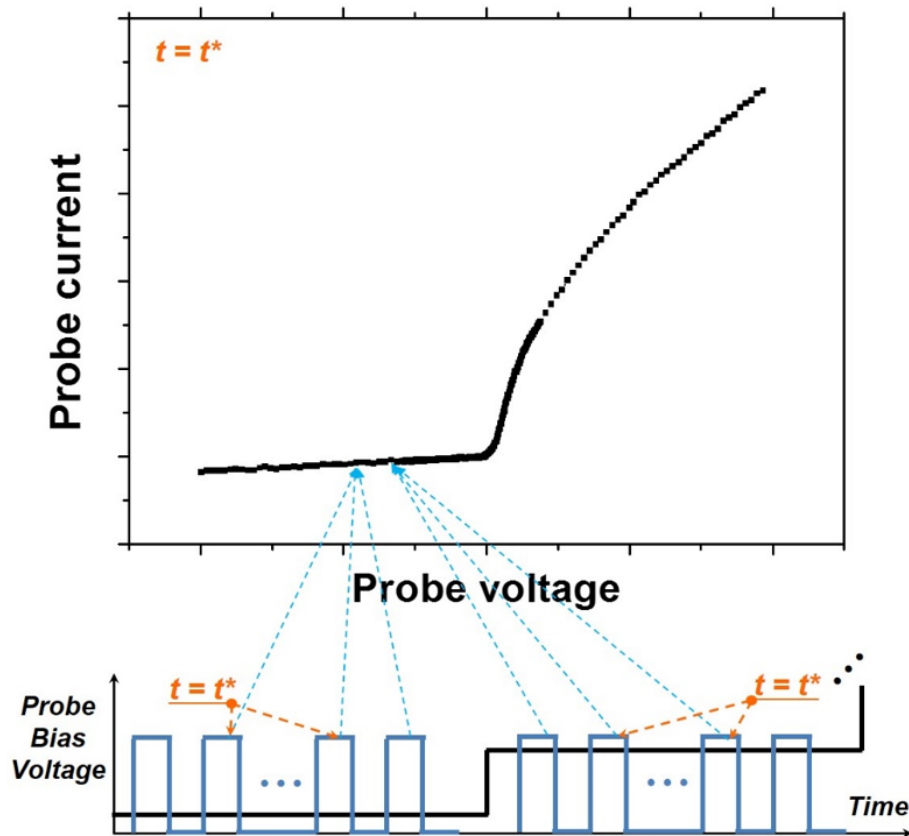


Figure 2.20 Schematic diagram of the boxcar sampling technique.

2.5.3 Probe-assisted laser photodetachment technique

The H^- ion source technologies require diagnostics in order to understand H^- ion behavior and underlying physics of ion sources. According to the work of Bacal, [52] two characteristic features of H^- ion lead to the need for specialized diagnostics. Firstly, it is difficult for H^- ions to be measured using electrostatic probe diagnostics because they are easily confined by the ambipolar potential. Secondly, the H^- ion does not have a single-electron

excited state below the detachment limit so that no light is emitted in collisions of H^- ions with electrons or heavy particles. Thus, the spectroscopies, such as laser-induced fluorescence spectroscopy and optical emission spectroscopy (OES), using the light emission of the excited state are not available.

The laser photodetachment technique is a representative of the specialized diagnostics for measurement of H^- ion density. [52, 53] Because the electron affinity of H atoms is low, the cross section for the photodetachment of H^- ions is fairly large, as shown in Figure 2.21.

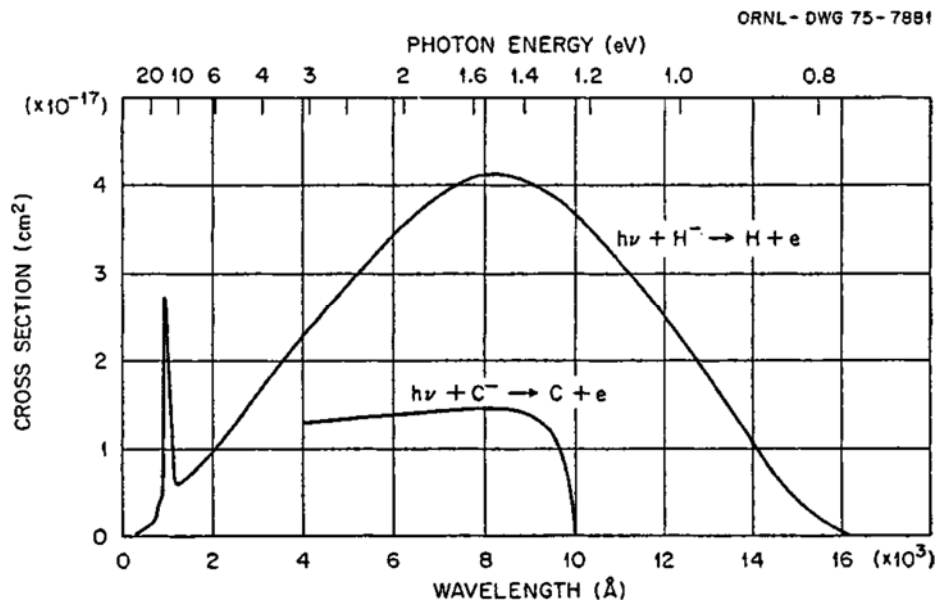


Figure 2.21 Photodetachment cross sections of H^- and C^- as a function of laser wavelength, from [53].

This large cross section guarantees that a laser beam can sufficiently photodetach H^- ions to yield large enough photodetachment signals, with

little chance of photoionization of H atoms to make another signals. This selectivity allows the laser photodetachment techniques to be applied to the diagnostics for measuring H^- ion density. As seen in Figure 2.21, the photodetachment cross section of H^- ions has its peak at about 1.5 eV near the photon energy of Neodymium Yttrium Aluminum Garnet (Nd:YAG) laser (1.2 eV). Thus, Nd:YAG laser is typically used for the photodetachment of H^- ions. On account of the high cross section of the photodetachment at the laser energy, the Nd:YAG laser can completely (see Figure 2.22) and instantly photodetach all H^- ions in the volume where laser beam is injected across with only a very modest laser pulse energy.

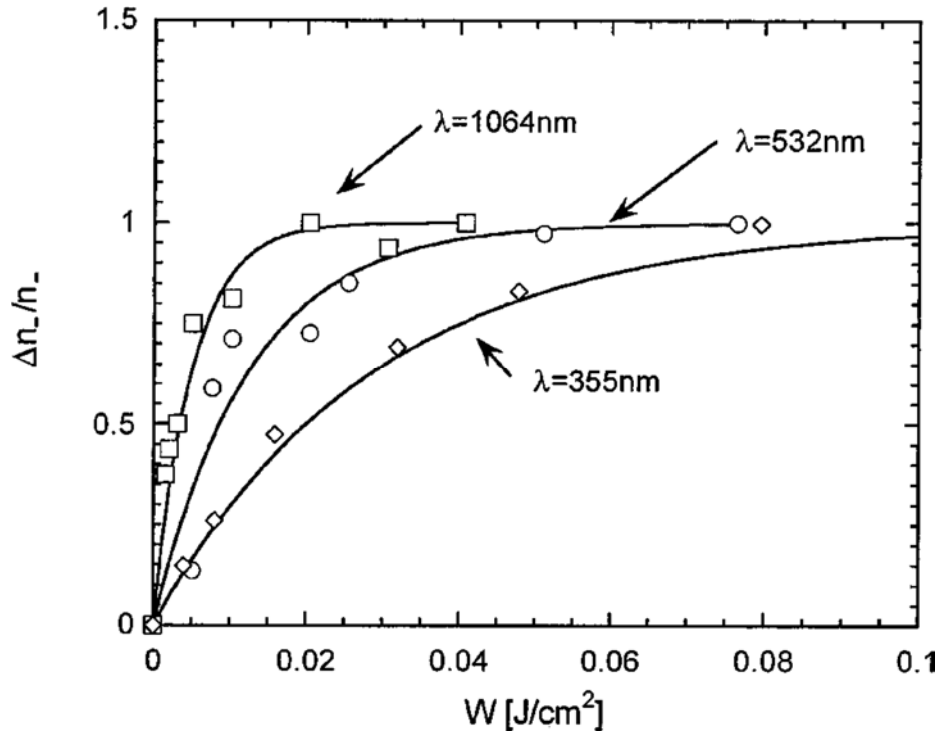


Figure 2.22 Variation of $\Delta n_{H^-}/n_{H^-}$, where Δn_{H^-} is the density of H^- ions destroyed by the photodetachment and n_{H^-} is the H^- ion density, with laser pulse energy, for three wavelengths of laser light, from [53]. The saturation of $\Delta n_{H^-}/n_{H^-}$ at energies above a modest level ($>20 \text{ mJ/cm}^2$) is attributed to full photodetachment.

Therefore, the Nd:YAG laser photodetachment techniques have two advantages from a diagnostic point of view: (1) The large diagnostic signals can be obtained. (2) The instantaneous photoelectron density is a direct measure of the H^- ion density.

To measure of the H^- ion density using the Nd:YAG laser photodetachment techniques, a measurement method to detect the photodetached electrons is

highly necessary. [53] One of the simple methods is the use of Langmuir (conductive) probes operated at a bias voltage equal to or higher than plasma potential, collecting the DC electron saturation current $i_{e(dc), sat}$ proportional to the background plasma electron density n_e . The schematic diagram of the probe-assisted laser photodetachment technique is shown in Figure 2.23.

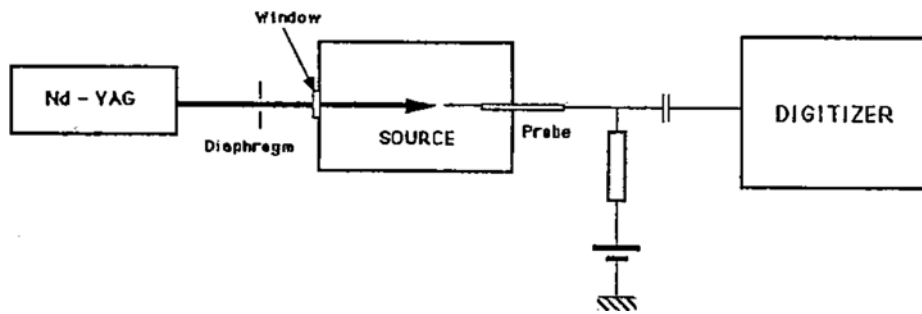


Figure 2.23 Cylindrical metal probe tip aligned parallel to the laser beam axis, electrically biased and drawing a conduction current from the plasma, from [53].

Figure 2.23 shows a cylindrical probe tip aligned parallel to the Nd:YAG laser beam axis. The probe tip, more precisely, the probe sheath (the region for collecting electrons) should lie inside the laser beam. Before the laser beam is injected into plasma, $i_{e(dc), sat}$ can be measured by the probe. When the laser pulsing occurs, the laser photodetachment causes an instantaneous increase in the electron density Δn_e . At this moment, $i_{e(dc), sat}$ added the current Δi_e corresponding to Δn_e is collected by the probe. Because Δi_e induced by the laser pulse is also instantaneous, a DC blocking capacitor is sometimes used to collect only Δi_e .

If the laser pulse energy is sufficient to photodetach all the H^- ions, and the probe is inserted in the beam, $\Delta i_e / i_{e(dc), sat} = \Delta n_e / n_e$ and $\Delta n_e = n_{H^-}$. These two relation yields $\Delta i_e / i_{e(dc), sat} = n_{H^-} / n_e$. Consequently, n_{H^-} can be measured using $\Delta i_e / i_{e(dc), sat}$ together with n_e obtained from the I – V characteristic.[†]

[†] Another method for measuring the H^- ion density developed by the author, the laser-assisted H_α spectroscopy, is presented in Appendix B.

Chapter 3. Modeling of an inductive coupled hydrogen plasma

This chapter presents theoretical models and approaches, which help to understand the underlying plasma physics of RF driven H^- ion source drivers. The global model of a hydrogen plasma, the electromagnetic model of an ICP, and the analytic model of collisionless heating will be discussed. These models allow one to analyze theoretically the chemical reaction kinetics in hydrogen plasmas, the power absorbed by plasma (or the power transfer efficiency) of ICPs, and the characteristic collision frequencies of the heating mechanisms and collisions.

3.1 Global model of a hydrogen plasma

The global (volume-averaged) model is a simple model for analyzing gas-phase and surface reaction kinetics in chemically complex low-temperature plasmas. [54] Global models of hydrogen plasma discharges, which are associated predominantly with negative ion sources, have been developed by several research groups. [54–59] Zorat *et al.* developed a hydrogen plasma global model that takes into account the magnetic filter effect and compared the electron density and temperature of the model to experimental measurements collected from an ICP at 10–100 mTorr. [55, 56] They emphasized that the ratio between the hydrogen H^- ion density to the electron density was far lower

than 0.1 in the model under the most optimistic assumptions for H^- ion production. Kimura and Kasugai studied the effects of diluting hydrogen discharges with argon on the plasma parameters, assuming a Maxwellian electron energy distribution (EED). [57] More recently, Hjartarson *et al.* extended Kimura and Kasugai's study by considering reactions involved in the negative ions and the vibrationally excited states of H_2 molecules [58] Pagano *et al.* investigated the effects of cesium on hydrogen kinetics in a model for the multicusp negative ion sources. [59] Other modeling approaches, such as two-dimensional fluid models and particle-in-cell simulations using Monte Carlo collision models, have been used to analyze the reaction kinetics in hydrogen plasmas.[60–66]

In all of the aforementioned hydrogen plasma global models, the EED was assumed to be Maxwellian. Some researchers have identified that a change in the EEDF, i.e., from a Maxwellian EEDF to a non-Maxwellian EEDF, can affect the model results. [57, 58] Although there were some attempts to employ the global model to explore the effects of the EED on the plasma characteristics in low-pressure argon, nitrogen, and chlorine plasmas, [67–69] few such studies have addressed the reaction kinetics in pure hydrogen plasmas with bi-Maxwellian EEDs that have been reported in low-pressure ICPs. A global model of a low-pressure hydrogen ICP with an arbitrary EEDF to analyze the densities of all species including the H^- ion and the electron temperature in the bi-Maxwellian plasma has been developed as follows.

The global model only addresses the spatially averaged plasma parameters in a steady-state discharge system. [55] For a given set of external condition

parameters, the model yields outputs, i.e., the electron temperature and spatially averaged species densities, which provides the cause-and-effect relationship between the external condition parameters and the outputs. Despite neglecting the spatial variations, it is enough for the model to understand the mechanisms that underlie the cause-and-effect relationship and to provide qualitative or even quantitative agreements with the experimental parameters. [54, 55] The global model of a hydrogen plasma with a cylindrical geometry was designed to calculate the electron impact collision reaction rate constants and the sheath properties, given a non-Maxwellian EED. Therefore, the model permits investigation of the chemical kinetics in a low-pressure bi-Maxwellian plasma. This model with the assumption that a plasma has floating sheaths offers an appropriate description of the electrodeless RF discharge (e.g., ICP) of which walls are not biased. The species of interest in the model are the ground state and excited states of the hydrogen atoms ($H(n=1)$ and $H(n=2-4)$), the ground state and vibrationally excited states of the hydrogen molecules ($H_2(v=0)$ and $H_2(v=1-14)$), the positive ions (H^+ , H_2^+ , and H_3^+), negative ions, and electrons (e^-). The model consists essentially of a set of nonlinear algebraic equations that describe the particle balance for each species (except for the electron), the quasi-neutrality, and the power (or energy) balance. Moreover, the model involves numeric calculations of the charge flux balance equation at the wall and the dispersion relation in front of the sheath edge. The potential difference between the sheath edge and the wall, and the potential drop between the bulk plasma and the sheath edge can be obtained from the charge flux balance equation and the dispersion relation, respectively. [55, 58] The 25 outputs in the

model can be obtained by solving the 25 nonlinear equation sets self-consistently using the built-in functions, *fsolve* (for the global model calculation of steady-state plasmas) and *ode45* (for the global model calculation of pulsed plasmas), in MATLAB R2013a (Mathworks Inc., Natick, MA, USA).

3.1.1 Particle balance equation

The sum of all generation and destruction reaction rates, together with the rates at which the particles flow into and out of the system for a particle species i , must be equal to the temporal variations of the species density. The temporal variations are equal to zero in the steady-state that the variables remain unchanged over time;

$$\frac{dn_i}{dt} = \sum_j (\pm N_j k_j \prod_l n_{R,l}) + \Phi_{in,i} - \Phi_{out,i} = 0, \quad (3.1.1)$$

where n_i is the density of the species i (except for the electron), N_j is the stoichiometric coefficient of the species produced by the generation reaction j associated with the species i ($N_j = 1$ for the species destroyed during the volume-destruction reaction j because all volume reactions considered in the model were two-body reactions. Three-body reactions were neglected due to the low-pressure conditions), k_j is the rate constant of the reaction j , $n_{R,l}$ is the density of the reactant l , Φ_{in} is the rate at which particles flow into the system ($\Phi_{in} \neq 0$ only for H_2 of the feedstock gas), and $\Phi_{out,i}$ is the rate at which particles are pumped out of the system. In the first term of the equation, the plus (minus) sign refers to the generation (destruction) reactions. The reactions can be classified into the volume reactions and the surface reactions that take place

inside the volume and on the surfaces of the plasma reactor, respectively. The volume and surface reactions selected in the model are listed in Table 3.1.

TABLE 3.1 Volume and surface reactions for the model and their references.

No.	Reaction formula	Description	Reference
1	$e^- + H (n=1\sim 4) \rightarrow e^- + H (n=1\sim 4)$	H elastic scattering ^a	70, 71
2	$e^- + H (n=1\sim 3) \rightarrow e^- + H (m=2\sim 4); (n < m)$	H excitation	70, 72
3	$H (n=2\sim 4) \rightarrow H (m=1\sim 3) + h\nu; (n > m)$	Spontaneous decay	73
4	$e^- + H (n=1\sim 4) \rightarrow e^- + H^+ + e^-$	H ionization	70, 72
5	$H (n=1) + H (n=3, 4) \rightarrow H_2^+ + e^-$	Associative ionization	74
6	$e^- + H^+ \rightarrow e^- + H (n=1) + e^-$	Electron detachment	70, 73
7	$H^+ + H^- \rightarrow H (n=3) + H (n=1)$	H ⁺ - H ⁻ mutual neutralization	70, 73
8	$H^+ + H (n=1\sim 4) \rightarrow H_2 (v=1\sim 5) + e^-$	Associative detachment ^{b, d}	70, 73–75
9	$e^- + H_2 (v) \rightarrow e^- + H_2 (v)$	H ₂ elastic scattering ^{a, c}	76
10	$e^- + H_2 (v) \rightarrow e^- + H_2 (v')$	Vibrational excitation or de-excitation via H ₂ ⁻ ^{b, d}	22, 76–82
11	$e^- + H_2 (v) \rightarrow e^- + H_2 (v') + h\nu$	Vibrational excitation or de-excitation via H ₂ [*]	83, 84
12	$e^- + H_2 (v=0) \rightarrow e^- + H (n=1\sim 3) + H (n=1)$ $e^- + H_2 (v=0) \rightarrow e^- + H (n=2) + H (n=2)$	Dissociation ^d	70, 73, 85
13	$e^- + H_2 (v) \rightarrow e^- + H_2^+ + e^-$	Non-dissociative ionization	70, 73, 85, 86
14	$e^- + H_2 (v=0) \rightarrow e^- + H^+ + H (n=1) + e^-$	Dissociative ionization ^d	70, 73, 83
15	$e^- + H_2 (v=3\sim 14) \rightarrow H^- + H (n=1)$	Dissociative electron attachment ^d	74
16	$H^+ + H_2 (v=4\sim 14) \rightarrow H (n=1) + H_2^+$	H ⁺ - H ₂ charge exchange ^d	74

17	$e^- + H_2^+ \rightarrow e^- + H^+ + H (n=1)$	Dissociative excitation ^d	70, 73, 74
18	$e^- + H_2^+ \rightarrow H (n=1) + H (n=3, 4)$	H_2^+ dissociative recombination ^d	70, 73
19	$H (n=1) + H_2^+ \rightarrow H^+ + H_2 (v=0)$	H - H_2^+ charge exchange	74, 87
20	$H_2^+ + H_2 (v=0) \rightarrow H_3^+ + H (n=1)$	H_3^+ ion formation	14, 70, 74
	$e^- + H_3^+ \rightarrow 3H (n=1)$		
21	$e^- + H_3^+ \rightarrow H_2 (v=6-14) + H (n=2)$	H_3^+ dissociative recombination ^d	70, 73, 74
22	$e^- + H_3^+ \rightarrow 2H (n=1) + H^+ + e^-$	Dissociative excitation	70, 73, 74, 88
23	$H_2^+ + H^- \rightarrow H_2 (v=0) + H (n=4)$	H_2^+ - H^- mutual neutralization ^d	74, 89-91
24	$H_3^+ + H^- \rightarrow H_2 (v=0) + H (n=1) + H (n=4)$	H_3^+ - H^- mutual neutralization ^d	74, 89, 90, 92, 93
25	$H (n=1) + H_2 (v) \rightarrow H (n=1) + H_2 (v-1)$	H - H_2 vibration-translation energy transfer (de-excitation) ^e	94, 95
26	$H_2 (w) + H_2 (v) \rightarrow H_2 (w) + H_2 (v-1)$	H_2 - H_2 vibration-translation energy transfer (de-excitation)	96
27	$H \xrightarrow{surface} \frac{1}{2} H_2$	Wall neutral recombination	97-100
28	$H_2 (v) \xrightarrow{surface} H_2 (v'); (v' < v)$	Wall vibrational de-excitation	101, 102
29	$H (n=2-4) \xrightarrow{surface} H (m=1); (n > m)$	Wall H de-excitation	
30	$H^+ \xrightarrow{surface} H (n=1)$	Wall H^+ neutralization	
31	$H_2^+ \xrightarrow{surface} H_2 (v=0)$	Wall H_2^+ neutralization	
32	$H_3^+ \xrightarrow{surface} H (n=1) + H_2 (v=0)$	Wall H_3^+ neutralization	

^aElastic scattering was not included in the particle balance equation because the species taking part in the reaction remain unchanged after the reaction.

^bThe cross section of the reaction was estimated by extrapolation since it was not supported by direct experimental measurements or theoretical data.

^cThe ground state and all excited states were assumed to have the same cross section.

^dSome processes related to the specific state n or v were neglected to improve the calculation efficiency in the model because these processes have relatively small reaction rates.

°Reactions related to H (n>1) were excluded in the model for simplicity, under the assumption that neutral H (n=1) is the most dominant species.

Volume reaction

The rate constant of the two-body volume reaction collision can be expressed as

$$k_j = \langle \sigma(v_{12})v_{12} \rangle, \quad (3.1.2)$$

where σ is the cross section, v_{12} is the magnitude of the relative velocity, and the triangular brackets denote averaging over the distribution of v_{12} . [63] If the two particles are identical, [33]

$$k_j = \frac{1}{2} \langle \sigma(v_{11})v_{11} \rangle. \quad (3.1.3)$$

In the electron impact collision reaction, v_{12} is approximately equal to the electron velocity, and the rate constant can be obtained by averaging over the EEDF. The model can calculate the electron impact collision reaction rate constant of an arbitrary EEDF, including a bi-Maxwellian EEDF over the considered electron temperature range up to 50 eV:

$$f(\varepsilon)d\varepsilon = 2\pi[(1-\beta)\sqrt{\frac{\varepsilon}{(\pi T_{e,low})^3}} \exp(-\frac{\varepsilon}{T_{e,low}}) + \beta\sqrt{\frac{\varepsilon}{(\pi T_{e,high})^3}} \exp(-\frac{\varepsilon}{T_{e,high}})]d\varepsilon, \quad (3.1.4)$$

where ε is the electron kinetic energy (in electron volts), β is the ratio of the high-energy electron density to the total electron density, $T_{e,low}$ is the electron temperature (in eV) of the low-energy electron group, and $T_{e,high}$ is the electron temperature of the high-energy electron group. The rate constants of all other heavy particle collisions (i.e., ion – ion, ion – neutral, and neutral – neutral

collisions) were calculated assuming that each reactant has a Maxwellian velocity distribution at different temperatures: [103]

$$k_j = 2 \left(\frac{2m_1 k_B T_2 + 2m_2 k_B T_1}{\pi m_1 m_2} \right)^{1/2} \int_0^{\infty} \exp(-\xi) \sigma(u_{12}) \xi d\xi, \quad (3.1.5)$$

where k_B is the Boltzmann constant, m is the species mass, T is the temperature of the species (in Kelvin units), and

$$\xi \equiv \frac{m_1 m_2}{2m_1 k T_2 + 2m_2 k T_1} u_{12}^2. \quad (3.1.6)$$

Although most of the rate constants in the volume reactions can be calculated based on the cross section data, as listed in Table 3.1, some rate constants (of reaction Nos. 1, 8, 10, 21, and 23–26) were difficult to calculate due to a lack of the cross section data. The following unavoidable manipulations and assumptions were applied to those cross section data using the reference data.

The elastic scattering cross section of the H (n) atom was obtained by averaging the cross sections of the various angular momentum states identified by Bray and Stelbovics, [70, 71] based on the assumption that elastic scattering are equally probable across the angular momentum states.

The most important collisions between H^- ions and H (n) atoms are the resonant charge exchange, associative detachment, and non-associative detachment. [74] Except for the resonant charge exchange, in which the reactants and products remain unchanged, the associative detachment is dominant over non-associative detachment at energies below 4 eV. In low-temperature plasmas, the energies and ions and neutrals are normally in the sub-

eV range, and only associative detachment was included in the $H^- - H$ (n) collisions of the model. The cross sections of $H^- + H (n = 1) \rightarrow H_2 (v > 0) + e^-$ were estimated by multiplying the factors by the cross section of $H^- + H (n = 1) \rightarrow H_2 (v = 0) + e^-$. [73] These factors are the relative ratios of the cross sections for populating the vibrationally excited state v of H_2 molecules, obtained by summing over the cross sections of rotational levels J to the specific v at 0.646 eV. [75] Because the collision processes of $H^- + H (n > 1) \rightarrow H_2 (v) + e^-$ have not been studied so far, [74] their cross sections were assumed to be equal to the cross sections of $H^- + H (n = 1) \rightarrow H_2 (v = 0) + e^-$ multiplied by the weighting factors which are the relative ratios of the ionization cross sections of $H (n > 1)$ and $H (n = 1)$ atoms.

There are two electron impact collision reactions for the vibrational excitation (or de-excitation) of H_2 molecules ($X^1\Sigma_g^+$). One is the vibrational excitation via $H_2^-(X^2\Sigma_u^+, B^2\Sigma_g^+)$ by collisions of H_2 molecules with low-energy electrons, another one is the vibrational excitation via $e + H_2^*(N^1\Lambda_u)$, accompanied by radiative decay, by collisions of H_2 molecules with high-energy electrons. [74, 22] Unlike the cross section data on the vibrational excitations or de-excitations via H_2^* provided by Celiberto *et al.*, [83, 84] the estimations of cross sections on some highly vibrational excitations or de-excitations via H_2^- were required due to a lack of data. The cross-sections of the $v = 0 \rightarrow v' > 1$ transition were calculated using the formula proposed by Shakhmatov and Lebedev [77, 78] together with the cross-section of the $v = 0 \rightarrow v' = 1$ transition. [76] The threshold energies ε_{th} of the $v = 0 \rightarrow v' > 1$ transition cross-sections were determined from the differences between the vibrational energy levels. [79] For

the estimation of the cross-sections of the $v > 0 \rightarrow v' > 1$ transition, the curve-fitting formulae on the correction factors (i.e., the dependence of the maximum cross section amplitude $\sigma_{max}^{v \rightarrow v'}/\sigma_{max}^{v=0 \rightarrow v'}$, ε_{th} shift, and breadth $\varepsilon(\sigma_{max}^{v \rightarrow v'}) - \varepsilon_{th}$ as a function of the state v and $\Delta v = |v' - v|$) that represent the departures of the cross-sections of the $v > 0 \rightarrow v' > 1$ transition from the cross-sections of the $v = 0 \rightarrow v' > 1$ transition was devised. The coefficients of the formulae were determined using the data reported by Gao and Capitelli *et al.* [80, 81]. This model took no account of the oscillating structures of the vibrational excitation cross sections that grow more and more severe at higher vibrational states. The estimations of cross sections on vibrational de-excitation via H_2^- were processed in the same way using the curve-fitting formulae and data given by Horáček *et al.* and Capitelli *et al.* [81, 82].

In the dissociative recombination by collisions of H_3^+ with electrons, the branching ratios of the reaction channels producing three-body (3 H) and two-body ($H_2 + H$) fragments as a function of the relative collision energy are almost constant at energies below 0.3 eV, with average values of 0.75 and 0.25, respectively. [74] The average branching ratios were adopted in the model.

The cross sections for the mutual neutralizations of H_2^+ and H_3^+ ions with H^- ions have not been studied sufficiently, unlike the $H^+ - H^-$ mutual neutralization. [74, 90, 91] Furthermore, the $H_3^+ - H^-$ mutual neutralization has the complexity that correlates with the predissociation channels of H_3 (produced by the electron capture in the collision of H_3^+ and H^-) to 3 H and $H_2 + H$. Not only the total cross section of the $H_3^+ - H^-$ mutual neutralization, but also the predissociation branching ratio which is dependent on the H_3

excited states must be considered in principle. [92, 93] For simplicity, the data from Eerden *et al.* [89] was chosen as the cross sections of the $H_2^+ - H^-$ and $H_3^+ - H^-$ mutual neutralizations in the model, with consideration for the values reported by other references. [90–93]

No cross section data were available for the vibration – translation energy transfer relaxation (or de-excitation) processes of the $H - H_2$ and $H_2 - H_2$ collisions, thus the temperature-dependent formulae of their rate constants (for the most dominant $\Delta v = 1$ case) given by Mandy and Martin, [95] and Matveyev and Silakov [96] were employed, respectively. The $H - H_2$ vibration – translation energy transfer rate constants were calculated using the effective gas temperature of H and H_2 as the temperature in the formula, as suggested by Biel *et al.* [94]

Surface reaction of the neutral species

The wall neutral recombination of H atoms, wall vibrational de-excitation (or relaxation) of H_2 molecules, and wall de-excitation of H atoms are major surface reactions that neutral species are lost at the walls. These rate constants are, respectively, given by

$$k_j = \left[\frac{\Lambda_0^2}{D_{eff, H}} + \frac{2V(2 - \gamma_{rec})}{Av_H \gamma_{rec}} \right]^{-1}, \quad (3.1.7)$$

$$k_j = \left[\frac{\Lambda_0^2}{D_{eff, H_2}} + \frac{2V(2 - \gamma_{q, H_2}(v))}{Av_{H_2} \gamma_{q, H_2}(v)} \right]^{-1}, \quad (3.1.8)$$

and

$$k_j = \left[\frac{\Lambda_0^2}{D_{eff,H}} + \frac{2V(2-\gamma_{q,H})}{A\bar{v}_H\gamma_{q,H}} \right]^{-1}, \quad (3.1.9)$$

where Λ_0 is the effective diffusion length, D_{eff} is the effective diffusion coefficient, V is the plasma chamber volume, A is the plasma chamber surface area, \bar{v} is the average velocity of the neutral particles ($\bar{v} = (8k_B T/\pi m)^{1/2}$), γ_{rec} is the wall neutral recombination coefficient, and γ_q is the wall quenching coefficient (or repopulation probability). The effective diffusion length Λ_0 is expressed as

$$\Lambda_0 = \left[\left(\frac{\chi_{01}}{R} \right)^2 + \left(\frac{\pi}{L} \right)^2 \right]^{-1/2}, \quad (3.1.10)$$

where χ_{01} is the first zero of the zero order Bessel function, R is the radius of the cylindrical chamber, and L is the chamber length. For the surface reaction, γ_{rec} and γ_q are used to characterize the probability that a specific wall reaction will occur, analogous to the cross section of the volume reaction. The wall neutral recombination coefficient γ_{rec} represents the probability that two H atoms could recombine and form a H_2 molecule at the wall, and it depends on the wall temperature T_{wall} (in Kelvin). To obtain $\gamma_{rec}(T_{wall})$, the experimental data of γ_{rec} for silica, alumina, and stainless steel surfaces provided by Green *et al.*, [97] Wood and Wise, [98] and Abe *et al.* [99, 100] were fitted to curves of the piecewise formula $\gamma_{rec} = \gamma_0 \exp(-E/R_c T_{wall})$, where γ_0 , E and R_c are constants. The wall quenching coefficient γ_q is the probability that represents the de-excitations in collisions of the vibrational excited molecules or the excited atoms with the wall. γ_q of H_2 , γ_{q,H_2} , is varied with v , and the relevant data from Hiskes and Karo, [101] and Taccogna *et al.* [102] were used in the

model. The excited atoms undergoing collisions with the wall were assumed to be de-excited to the ground states, so that $\gamma_{q,H} = 1$. The effective diffusion coefficients of the H atom and the H₂ molecule in equations (3.1.7) – (3.1.9) consist of a Knudsen free diffusion part and a collisional diffusion part involving other H atoms and H₂ molecules:

$$\frac{1}{D_{eff,H}} = \frac{1}{D_{Kn,H}} + \frac{1}{D_{H-H}} + \frac{1}{D_{H-H_2}}, \quad (3.1.11)$$

and

$$\frac{1}{D_{eff,H_2}} = \frac{1}{D_{Kn,H_2}} + \frac{1}{D_{H_2-H}} + \frac{1}{D_{H_2-H_2}}, \quad (3.1.12)$$

where D_{Kn} is the Knudsen free diffusion coefficient ($D_{Kn} = \frac{\bar{v}\Lambda_0}{3}$) and D_{A-B} is the collisional diffusion coefficient for species A diffusing into species B . A and B denote the neutral species (i.e., H and H₂). It was assumed that the collisional diffusion coefficient could be described using the two-temperature binary ordinary diffusion coefficient developed in the Chapman-Enskog method: [104]

$$D_{A-B} = \left(\frac{2\pi k_B}{\mu_{AB} T_{AB}^*} \right)^{1/2} \frac{3T_A g_{AB}}{16n_N \bar{Q}_{AB}^{(1,1)}}, \quad (3.1.13)$$

where μ_{AB} is the reduced mass of the species A and B , T_{AB}^* is the collision effective temperature (in Kelvin), T_A is the kinetic temperature (in eV) of the species A , n_N is the total number density of neutrals, $\bar{Q}_{AB}^{(1,1)}$ is the diffusion collision integral which takes into account the interactions between the colliding species A and B , and

$$g_{AB} \equiv \frac{(m_B + m_A \theta_{BA})^2 (m_A + m_B \theta_{BA})^3}{\theta_{BA}^{5/2} (m_B + m_A)^5}. \quad (3.1.14)$$

Here, the non-equilibrium parameter θ_{AB} is defined as T_A/T_B . The temperature-dependent values of $\bar{Q}_{H-H}^{(1,1)}$, $\bar{Q}_{H-H_2}^{(1,1)}$, $\bar{Q}_{H_2-H}^{(1,1)}$, and $\bar{Q}_{H_2-H_2}^{(1,1)}$ were provided by Stallcop *et al.* [105, 106] The collision effective temperature is given by

$$T_{AB}^* = \left[\frac{1}{m_A + m_B} \left(\frac{m_A}{T_B} + \frac{m_B}{T_A} \right) \right]^{-1}. \quad (3.1.15)$$

Surface reaction of the ion species

Unlike electrons and negative ions, the potential drop across the presheath and sheath accelerates positive ions so that they escape to the walls. The rate constant of the positive ion loss to the walls is given by

$$k_j = u_{B, H_n^+} \frac{A_{eff}}{V}, \quad (3.1.16)$$

where u_{B, H_n^+} is the Bohm velocity ($n = 1, 2,$ and 3 for H^+ , H_2^+ , and H_3^+ ions) and A_{eff} is the effective area over which ions are lost. According to recent studies, [107–110] the ion Bohm velocities at the sheath edge are dependent on the relative ion density ratios in plasmas containing multiple ion species. Each ion Bohm velocity in two (inert gas) ion species plasmas, in particular, reaches its own Bohm velocity $u_{B,o} = (T_e/m_o)^{1/2}$, when the relative density ratio differences are large. On the other hand, both of the ion Bohm velocities are

closer to a common system sound velocity $u_B^{sys} = \sum_o [u_{B,o}^2 \{n_o / \sum_o n_o\}]^{1/2}$ if the relative ion density ratios are comparable. Unfortunately, the ion Bohm velocities of the three ion species in the hydrogen (the non-inert gas) discharges have not been studied so far either theoretically or experimentally. In this model, for reasons of convenience, the individual Bohm velocity u_{B,H_n^+} and the common system sound velocity u_B^{sys} were presumed to equal the Bohm velocities used to calculate the rate constant of the positive ion wall loss and the ion flux at the sheath edge (discussed in greater detail below), respectively. Given the presence of the negative ions, the Bohm velocity can be expressed by [111, 112]

$$u_{B,H_n^+} = \left[\left(\frac{1-\alpha_s}{eT_{e,eff}^B} + \frac{\alpha_s}{k_B T_{H^-}} \right) m_{H_n^+} \right]^{-1/2}, \quad (3.1.17)$$

where $\alpha_s \equiv n_{H^-,s} / n_{pi,s}$ is the electronegativity (i.e., the ratio of the negative ion density to the total positive ion density $n_{pi,s} \equiv \sum_n n_{H_n^+,s}$) at the sheath edge, e is the elementary charge, $T_{e,eff}^B = \left[\frac{1-\beta}{T_{e,low}} + \frac{\beta}{T_{e,high}} \right]^{-1}$ is the effective electron temperature (in electron volts) in the form of the density-weighting harmonic average used to calculate the Bohm velocity, [109] T_{H^-} is the negative ion temperature (in Kelvin), and $m_{H_n^+}$ is the mass of the positive ion species.

The expression describing the effective area of a cylindrical ICP with a multicusp magnetic configuration surrounding the chamber is [55, 56]

$$A_{eff} = 2\pi R (a_{cf} L h_R + R h_L), \quad (3.1.18)$$

where a_{cf} is the magnetic confinement parameter ranging between 0 and 1, and $h_{R,L}$ is the radial and planar dimensionless ion flux factor. a_{cf} , which is

introduced to consider the effect of the multicusp magnetic field on the effective area, is inversely proportional to the enhancement of plasma confinement. If a multicusp magnetic configuration is absent, a_{cf} is 1. The value of a_{cf} reported in previous studies was assumed to be constant, although this parameter depends on the electron and ion temperatures. The concept of the leak width $w \approx 4(\overline{r_{ce}} \overline{r_{cl}})^{1/2}$ ($\overline{r_{ce}}$ is the mean electron gyroradius and $\overline{r_{cl}}$ is ion the mean electron gyroradius) [113] was introduced to express the magnetic confinement parameter in this model as $a_{cf} = \xi w$, where ξ is a constant. The dimensionless ion flux factors can be approximated as the ratio of the positive ion density at the sheath edge to that at the discharge center, assuming that the volume-averaged ion density equals the central ion density. [54] Kim *et al.* attempted to describe the transitions of the dimensionless ion flux factors from the low to high pressures as well as from electropositive to highly electronegative schemes. [114, 115] For this model, limited solutions to the dimensionless ion flux factors proposed by Kim *et al.* have been utilized (except at high pressures) and have been patched heuristically using the root mean square ansatz: [55, 58, 114–116]

$$h_{L,R} = \sqrt{h_{La,Ra}^2 + h_{Lc,Rc}^2}, \quad (3.1.19)$$

$$h_{La} \approx 0.86(1 - \alpha_0) \left[3 + \frac{\eta L}{2\lambda_i} + \left(\frac{0.86 L u_B^{sys}}{\pi D_a} \right)^2 \right]^{-1/2}, \quad (3.1.20)$$

$$h_{Ra} \approx 0.80(1 - \alpha_0) \left[4 + \frac{\eta R}{\lambda_i} + \left(\frac{0.80 R u_B^{sys}}{\chi_{01} J_1(\chi_{01}) D_a} \right)^2 \right]^{-1/2}, \quad (3.1.21)$$

and

$$h_{Lc, Rc}^2 \approx \frac{1}{\gamma_-^{1/2} + \gamma^{1/2} [n_*^{1/2} n_{pi} / n_{H^-}^{3/2}]}. \quad (3.1.22)$$

Here, $\alpha_0 \equiv n_{H^-}/n_{pi}$ is the central electronegativity (i.e., the ratio of the central negative ion density to the central total positive ion density $n_{pi} \equiv \sum_n n_{H_n^+}$), $\eta \equiv 2T_{pi}/(T_{pi} + T_{H^-})$ (T_{pi} is the positive ion temperature (in eV)), $\lambda_i = 1/\sum_r n_r \sigma_{sc,r}$ is the positive ion – neutral mean free path, $D_a = D_i(1 + \gamma + \frac{2\gamma\alpha_s}{1-\alpha_s})/(1 + \frac{\gamma\alpha_s}{1-\alpha_s})$ is the ambipolar diffusion coefficient (D_i is the positive ion diffusion coefficient and $\gamma = T_{e,eff}^B/T_{pi}$), J_1 is the first-order Bessel function, $\gamma_- = T_{e,eff}^B/T_{H^-}$, and $n_* = \frac{15}{56} \frac{\eta^2}{k_{rec}\lambda_i} v_i$ (k_{rec} is the rate constant for mutual neutralization and v_i is the mean thermal velocity of the positive ions).

Particle flow rate at the inlet and outlet

Molecules in the feedstock H_2 gas is supplied to the chamber through a mass flow controller (MFC) at a rate given by [58]

$$\Phi_{in, H_2} \simeq 4.48 \times 10^{17} \frac{f_{H_2}}{V}, \quad (3.1.23)$$

where f_{H_2} is the gas flow rate controlled by the MFC in standard cubic centimeters per minute (SCCM), and the scalar constant is a conversion factor from the SCCM units into particles/s. In a similar way, the rate at which particles of species i are pumped out of the chamber can be formulated as follows: [55, 58]

$$\Phi_{out,i} = k_{out,i} n_i \approx 2.83 \times 10^{-20} \frac{\Phi_{in}}{p_{o,i}} n_i, \quad (3.1.24)$$

where $k_{out,i}$ is the rate constant of species i particles pumped out the system, the scalar constant is the ratio of $k_B T_{H_2}^{STP}$ to a conversion factor from mTorr units into Pa units ($T_{H_2}^{STP}$ is the temperature at standard temperature and pressure (STP) conditions), $p_{o,i}$ is the outlet pressure of the species i in mTorr, and n_i is the density of the species i . Zorat *et al.* [55] pointed out that $k_{out,i}$ is proportional to the average velocity of the species i particles in the molecular flow regime ($k_{out,i} \propto \bar{v} = [8k_B T / \pi m]^{1/2}$). Consequently, the ratio of the pumping rate constants for the two species with different temperatures or masses $k_{out,1}/k_{out,2}$ is linearly related to the square root of the temperature ratio $\sqrt{T_1/T_2}$ or the mass ratio $\sqrt{m_2/m_1}$. In this model, $k_{out,i}$ or $p_{o,i}$ was adjusted considering the relation above until the calculated pressure reaches a set pressure.

3.1.2 Quasi-neutrality equation and power balance equation

Instead of the particle balance equation for electrons, an equation that describes the quasi-neutrality of the plasma was used in the above-mentioned 25 nonlinear algebraic equation sets:

$$n_{pi} - n_e - n_H = 0, \quad (3.1.25)$$

where n_e is the electron density.

The power balance equation in the steady-state represents that the RF power

absorbed by the discharge is dissipated in the elastic and inelastic collisions within the volume of the reactor and consumed as the kinetic energy loss of charged particles escaping to the reactor walls. The equation is given by [58]

$$\frac{d}{dt} \left(\frac{3}{2} n_e T_{e, \text{eff}} \right) = \frac{P_{\text{abs}}}{V} - e \sum_j (k_j \prod_l n_{R,l}) \varepsilon_{c,j} - e u_B^{\text{sys}} n_{pi} \frac{A_{\text{eff}}}{V} (\varepsilon_e + \varepsilon_i) = 0, \quad (3.1.26)$$

where $T_{e, \text{eff}} = (1 - \beta)T_{e, \text{low}} + \beta T_{e, \text{high}}$ is the effective electron temperature (in eV) defined in the EEDF ($T_{e, \text{eff}}$ differs from $T_{e, \text{eff}}^B$ defined above), P_{abs} is the absorbed power by the plasma, $\varepsilon_{c,j}$ is the collisional energy loss of the reaction j , $\varepsilon_e = 2[(1 - \beta)T_{e, \text{low}}^{3/2} + \beta T_{e, \text{high}}^{3/2}] / [(1 - \beta)T_{e, \text{low}}^{1/2} + \beta T_{e, \text{high}}^{1/2}]$ is the average kinetic energy loss per electron entering the wall surface, and ε_i is the mean kinetic energy loss per ion striking the wall surface. Note that the right-hand side of Equation (3.1.26) is not zero and thus cannot be neglected for the calculation for pulsed plasmas because the plasma is not in the steady-state. The collisional energy loss $\varepsilon_{c,j}$ in an electron elastic collision process involving the neutral species j is $3m_e T_e / m_j$, and $\varepsilon_{c,j}$ in the inelastic collision processes are given in the cited references of Table 3.1. The value of $\varepsilon_{c,j}$ for the inelastic collision process may not be equal to the reaction threshold energy. For example, the threshold energy of a dissociation process that produces H ($n = 3$) and H ($n = 1$) (No. 12) in Table 3.1 is about 19.0 eV, but the mean collisional energy loss is 21.5 eV. The mean kinetic ion energy lost at the wall ε_i was transferred from the potential energy of the ion in the presheath and sheath:

$$\varepsilon_i = V_{ps} + V_s, \quad (3.1.27)$$

where V_{ps} is the voltage drop within the presheath region in which the ions are

accelerated from zero to the Bohm velocity, and V_s is the voltage drop between the sheath edge potential and the wall potential. Amemiya proposed an expression for V_{ps} , modified by the electronegativity in the electronegative plasma, using the dispersion relation in front of the sheath edge, [111]

$$V_{ps} = \frac{1}{2e} \left[\frac{1 - \alpha_s}{eT_{e,eff}^B} + \frac{\alpha_s}{k_B T_{H^-}} \right]^{-1}. \quad (3.1.28)$$

The electronegativity at the sheath edge α_s should satisfy the relation $\alpha_s = \alpha_0 \delta_n / [\delta_e (1 - \alpha_0) + \alpha_0 \delta_n]$, where $\delta_n \equiv \exp(-eV_{ps}/k_B T_{H^-})$ and $\delta_e \equiv \exp(-V_{ps}/T_{e,eff})$. This relation yields the multi-valued V_{ps} with respect to a specific α_0 , for $\gamma_- > 5 + \sqrt{24}$. [117] The selection of an appropriate value among the multi-valued V_{ps} of the Bohm criterion in electronegative plasmas has been embroiled in controversy over the past decade. [112, 117–119] Although the lowest value of the multi-valued solutions was selected as V_{ps} in this model, as suggested by Allen, [119] most of the calculations in this model were unaffected by the problem on the multi-valued solutions because the electronegativity of the hydrogen plasma was usually small and then the relation had one solution. For an ICP, V_s within a floating sheath can be obtained by numerically solving the equation that describes that the balance between the positive ion current density J_+ , negative ion current density J_{H^-} , and electron current density J_{e^-} at the sheath edge: [58, 119]

$$J_+ + J_{H^-} + J_{e^-} = 0, \quad (3.1.29)$$

where $J_+ = en_{pi} u_B^{sys} [(1 - \alpha_0) \delta_e + \alpha_0 \delta_n]$, $J_{H^-} =$

$$-\frac{1}{4}en_{H^-}\delta n\sqrt{\frac{8k_B T_{H^-}}{\pi m_{H^-}}}\exp\left(-\frac{eV_s}{k_B T_{H^-}}\right), \text{ and } J_{e^-} = -\frac{1}{4}en_e\delta_e\bar{v}_e\exp\left(-\frac{V_s}{T_{e,\text{eff}}}\right).$$

Here, m_{H^-} is the negative ion mass, m_e is the electron mass, and $\bar{v}_e = (1 - \beta)(8eT_{e,\text{low}}/\pi m_e)^{1/2} + \beta(8eT_{e,\text{high}}/\pi m_e)^{1/2}$ is the electron mean thermal velocity.

3.2 Electromagnetic model of an ICP

In order to calculate the power absorbed by the plasma (or the power transfer efficiency), a simple electromagnetic model of an ICP introduced by the textbook of Chabert and Braithwaite is employed. [37] If there is a long thin cylindrical ICP, with a uniform density, contained in a dielectric tube of radius r_0 , outer radius r_c and length l , (see Figure 3.1)

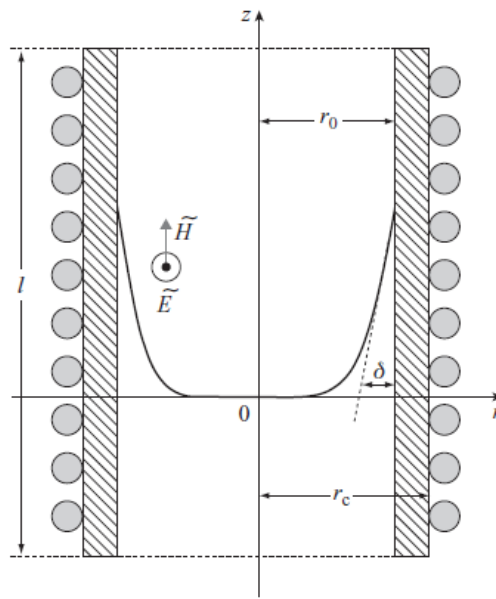


Figure 3.1 Schematic of the ICP. The plasma is contained in a dielectric tube of inner radius r_0 , outer radius r_c and length $l \gg r_0$. The tube is surrounded by a coil with N turns uniformly distributed, in which flows an RF sinusoidal current $I_{\text{RF}}(t) = \text{Re}[\tilde{I}_{\text{RF}}e^{i\omega t}]$, where \tilde{I}_{RF} is the complex amplitude and t is time. The induced electric field \tilde{E}_θ is azimuthal, while the induced magnetic field \tilde{H}_z is axial. At high plasma density, both fields decay within the skin depth δ , from [37].

the fields can be obtained from Maxwell's equations:

$$-\frac{\partial \widetilde{H}_z}{\partial r} = i\omega \varepsilon_0 \varepsilon \widetilde{E}_\theta \quad (3.2.1)$$

and

$$\frac{1}{r} \frac{\partial(r \widetilde{E}_\theta)}{\partial r} = -i\omega \mu_0 \widetilde{H}_z, \quad (3.2.2)$$

where ω is the angular wave frequency, ε_0 is the permittivity of free space, ε is the complex relative permittivity ($\varepsilon = \varepsilon_p$ in the plasma and $\varepsilon = \varepsilon_t$ in the tube), and μ_0 is the permeability of free space. Substituting the Equation (3.2.1) to the Equation (3.2.2), one can obtain an electromagnetic wave equation for \widetilde{H}_z :

$$\frac{\partial^2 \widetilde{H}_z}{\partial r^2} + \frac{1}{r} \frac{\partial \widetilde{H}_z}{\partial r} + k_0^2 \varepsilon \widetilde{H}_z = 0, \quad (3.2.3)$$

where $k_0 \equiv \omega/c$ is the wavenumber in free space. The solutions of Equation (3.2.3) are given by

$$\widetilde{H}_z = H_{z0} \frac{J_0(kr)}{J_0(kr_0)}, \quad (3.2.4)$$

and

$$\widetilde{E}_\theta = -\frac{ikH_{z0}}{\omega \varepsilon_0 \varepsilon_p} \frac{J_1(kr)}{J_0(kr_0)}, \quad (3.2.5)$$

where $H_{z0} \equiv \widetilde{H}_z(r=r_0)$, $k \equiv k_0 \sqrt{\varepsilon_p}$ is the complex wave number in the plasma, and J_0 and J_1 are the Bessel functions of the first kind.

If $k_1 r_0 \ll 1$ and the magnetic field is nearly constant in the tube ($\widetilde{H}_z \approx H_{z0}$ at $r_0 < r < r_c$), the following equation can be obtained from the integral form of Faraday's law:

$$\tilde{E}_\theta(r_c) = \tilde{E}_\theta(r_0) \frac{r_0}{r} - i\omega\mu_0 H_{z0} \left(\frac{r_c^2 - r_0^2}{2r_c} \right). \quad (3.2.6)$$

In addition, the plasma current, \tilde{I}_p , the current flowing in the dielectric tube, \tilde{I}_t , and the current flowing in the coil, \tilde{I}_{RF} , can be calculated from Ampère's theorem together with the contours in Figure 3.2:

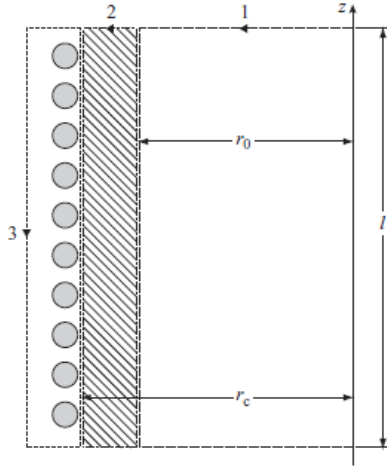


Figure 3.2 Ampère contours for the current in the plasma (1), in the dielectric tube (2), and in the coil (3), from [37].

$$\tilde{I}_p = l\tilde{H}_z(0) - lH_{z0} = lH_{z0} \left[\frac{1}{J_0(kr_0)} - 1 \right], \quad (3.2.7)$$

$$\tilde{I}_t = lH_{z0} - l\tilde{H}_z(r_c), \quad (3.2.8)$$

and

$$N\tilde{I}_{RF} = l\tilde{H}_z(r_c). \quad (3.2.9)$$

The sum of three equations then yields

$$\tilde{I}_p + \tilde{I}_t + N\tilde{I}_{RF} = \frac{lH_{z0}}{J_0(kr_0)}. \quad (3.2.10)$$

Since, as assumed above, the magnetic field is nearly constant in the tube, $\tilde{I}_t = 0$, and thus the magnetic field at the plasma edge, H_{z0} , with respect to \tilde{I}_{RF} is deduced from Equations (3.2.8) – (3.2.10) as follows:

$$H_{z0} = \frac{N\tilde{I}_{RF}}{l} = \frac{NI_{coil}}{l}, \quad (3.2.11)$$

where I_{coil} is the magnitude of the current in the coil.

From Poynting's theorem, the complex power input (i.e., the sum of the power dissipated and the power stored by the electromagnetic fields) is given by:

$$\tilde{P} = -\frac{1}{2}\tilde{E}_\theta(r_c)\tilde{H}_z(r_c)2\pi r_c l = \frac{1}{2}Z_{ind}I_{coil}^2, \quad (3.2.12)$$

where Z_{ind} is the total complex impedance of the system. Therefore, one can express dissipative and reactive components of the complex power input:

$$R_{ind} = \frac{2\text{Re}[\tilde{P}]}{I_{coil}^2}, \quad (3.2.13)$$

and

$$X_{ind} = \frac{2\text{Im}[\tilde{P}]}{I_{coil}^2}. \quad (3.2.14)$$

The Equation (3.2.12) together with Equation (3.2.6), (3.2.11), and $\tilde{H}_z(r = r_c) = H_{z0}$ can be rewritten as

$$\tilde{P} = i\frac{\pi N^2 I_{coil}^2}{l} \left[\frac{kr_0 J_1(kr_0)}{\omega \varepsilon_0 \varepsilon_p J_0(kr_0)} + \frac{1}{2} \omega \mu_0 (r_c^2 - r_0^2) \right]. \quad (3.2.15)$$

Finally, the time-averaged power absorbed by plasma (or dissipated in the

system) is given by

$$P_{abs} = \text{Re}[\tilde{P}] = \frac{\pi N^2}{l\omega\varepsilon_0} \text{Re}\left[\frac{ikr_0 J_1(kr_0)}{\varepsilon_p J_0(kr_0)} I_{coil}^2\right]. \quad (3.2.16)$$

3.3 Analytic model of collisionless heating

The collisional and collisionless heating are often accounted for by introducing an electron – neutral collision frequency and a stochastic (or collisionless) frequency, respectively. [45] These frequencies represent collisions / electron–field interactions that cause a change in phase coherence, and thus a net transfer of power. Unlike the electron – neutral collision frequency obtained directly from $\nu_{en} = n_g \langle \sigma_m v_e \rangle$ (n_g : the neutral density, σ_m : the cross section of the elastic momentum transfer collision, and the triangular brackets: averaging over the distribution of electron velocity v_e), [33, 37] the stochastic frequency obtained from the complicated numerical calculation of the spatially non-uniform RF fields determined self-consistently with the electron motions is not easy. [39] This always involves solving the full equations including the Maxwellian equations and the Boltzmann equation. (See Chapter 2, Section 2.4)

Vahedi *et al.* proposed the analytic model of the collisionless heating that is simplified by introducing appropriate assumptions, while maintaining a reliability. [120] In this model, the EEDF is assumed to be Maxwellian. By using the model, one can determine the stochastic frequency that is a measure of the collisionless heating in the non-local regime. The complete details of the model would go far beyond the scope of this study, so only final reduced equations for obtaining the stochastic frequency ν_{sto} are given in this section:

$$\Xi(\alpha) = \frac{1}{\pi} \int_0^{\infty} \frac{x e^{-x}}{(x + \alpha)^2} dx, \quad (3.3.1)$$

$$\frac{4\delta}{v_e} \Xi(\alpha) = \frac{v_{st}}{v_{st}^2 + \omega^2}, \quad (3.3.2)$$

and

$$\delta = \frac{c}{\omega_{pe}} \left(\frac{2(1 + v_{st}^2 / \omega^2)}{1 + (1 + v_{st}^2 / \omega^2)^{1/2}} \right)^{1/2}, \quad (3.3.3)$$

where $\alpha \equiv 4\delta^2 \omega^2 / \pi \bar{v}_e^2$, δ is the effective skin depth, ω is the angular wave frequency, \bar{v}_e is the electron mean thermal velocity, c is the speed of light, and ω_{pe} is the electron plasma frequency. A set of three simultaneous equations (i.e., Equations (3.3.1), (3.3.2), and (3.3.3)) can now be solved numerically for v_{sto} and δ . Here, δ does not always have the same geometrical significance associated with the exponential decay of fields as the classical skin depth (in cases when only collisional heating is considered) due to presence of the non-monotonic spatial decay in the anomalous skin layer. It is interesting to note that multiple solutions are possible. If multiple solutions are encountered, the only one solution that meets the relation illustrated in Figure 3.3 should be selected. [120]

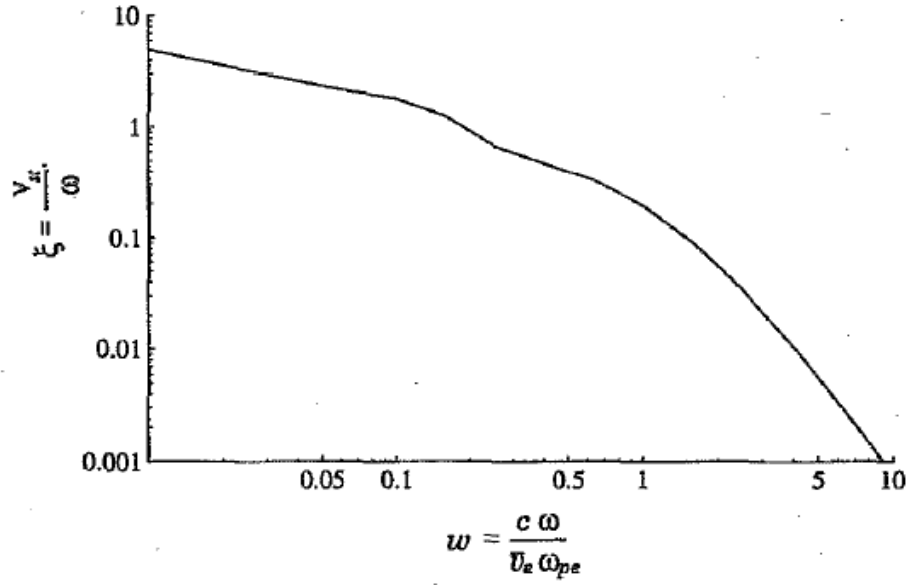


Figure 3.3 Variation of the normalized stochastic frequency as a function of the normalized frequency $w = (\omega c)/(\bar{v}_e \omega_{pe})$, from [120].

Additionally, the electron – electron collision frequency, ν_{ee} in sec^{-1} , can be obtained by the following equation: [121, 122]

$$\nu_{ee} \approx 3 \times 10^{-6} \frac{n_e \ln \Lambda}{T_e^{3/2}}, \quad (3.3.4)$$

where n_e is the electron density in cm^{-3} , T_e is the electron temperature in eV, and $\ln \Lambda = 23.5 - \ln(n_e^{1/2} T_e^{-5/4}) - [10^{-5} + (\ln T_e - 2)^2/16]^{1/2}$ is the Coulomb logarithm.

Chapter 4. The relation between H^- ion generation and EEDF

In this chapter, the relationship between the EEDF and the reaction kinetics of hydrogen plasmas involved in the generation and destruction of H^- ions and their precursors will be explored using both the developed global model and experimental measurements in a low-pressure inductively coupled hydrogen plasma. In experiments, the measured EEDFs were Maxwellian and bi-Maxwellian EEDFs, which coincides with the previous reports. (See Subsection 2.4.2) By comparing the densities of negative ions and other species with a bi-Maxwellian EEDF and those of a Maxwellian EEDF, the underlying relation was revealed and a more favorable EEDF shape for the H^- ion generation was found.

4.1 Experimental setup

The electron temperature and densities of all species, including the H^- ion, in a hydrogen bi-Maxwellian plasma were investigated using both experimental data and the developed model applied to an ICP, as depicted in Figure 4.1. [123, 124]

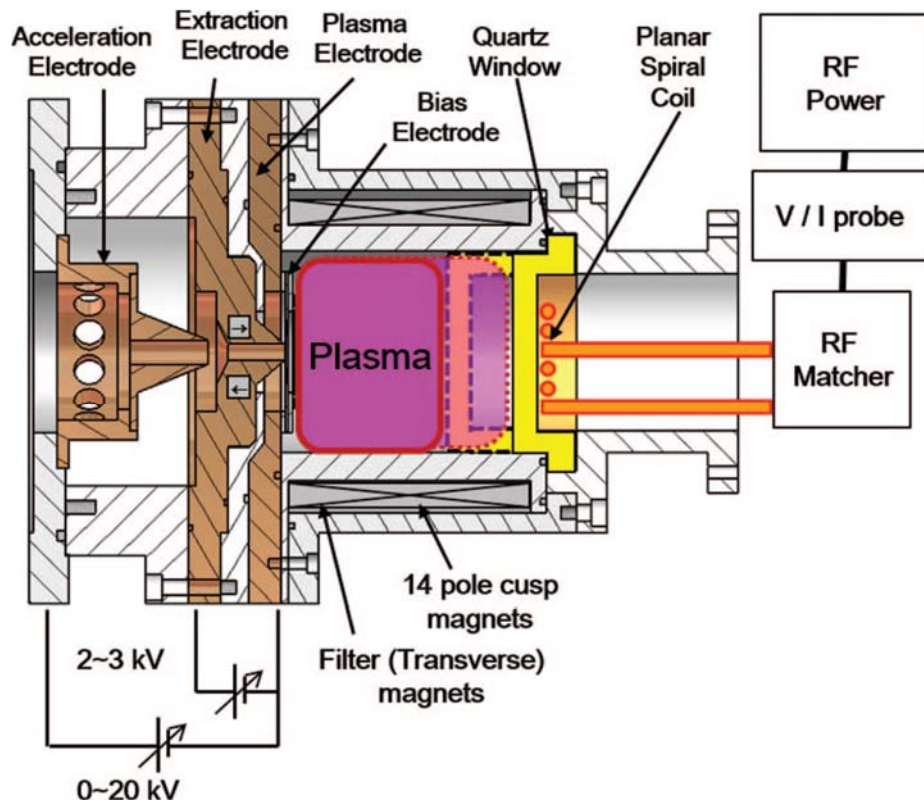


Figure 4.1 Schematic diagram of the inductively coupled hydrogen plasma, from [123].

The ICP source consists of a cylindrical plasma chamber of radius $R = 5$ cm and length $L = 7.5$ cm. The plasma was excited by a planar spiral antenna coil powered at a RF of 13.56 MHz. The antenna coil was positioned on a quartz plate that was used as an RF window at the top of the discharge chamber. The external walls of the chamber was encircled by samarium cobalt (SmCo) magnets which form a cusp field for improvement of the electron confinement in the radial direction. The confinement effect was taken into account in the model using the above-mentioned parameter a_{cf} . The experimental setup is

described in detail in Refs. 123 and 124. In the experiments and model analyses, the RF power was fixed at 900W and the hydrogen gas pressures were varied from 3 to 30 mTorr. The pressure variation can contribute significantly to change in the EED shape. [41] Simultaneous measurements of the plasma parameters (i.e., EEDF, electron density, and electron temperature) were carried out using RF compensated cylindrical Langmuir probes. In addition, the model results of the H^- ion densities were compared with measurements obtained using the laser (Nd-YAG laser, 532 nm) photodetachment technique. A magnetic filter was installed at the bottom of the chamber in order to lowering the electron temperature. The magnetic filter enables the H^- ion density to be increased, which increases the corresponding laser photodetachment signal to measurable levels. For calculation of the H^- ion densities in the vicinity of the magnetic filter, the particle balance equation (Equation (3.1.1)) of the H^- ion density was solved separately using the model results of the central neutral densities and positive ion density ratios, together with n_e and T_e measured by the probe at the bottom of the chamber. Only 40% of the neutrals in center were assumed to diffuse and reach the bottom of the chamber. In the model analysis, it was assumed that the gas temperature was assumed to be 500 K.

4.2 Global model analysis of bi-Maxwellian H₂ plasmas

4.2.1 EEDFs and its scalar integrals: effective electron temperature and electron density

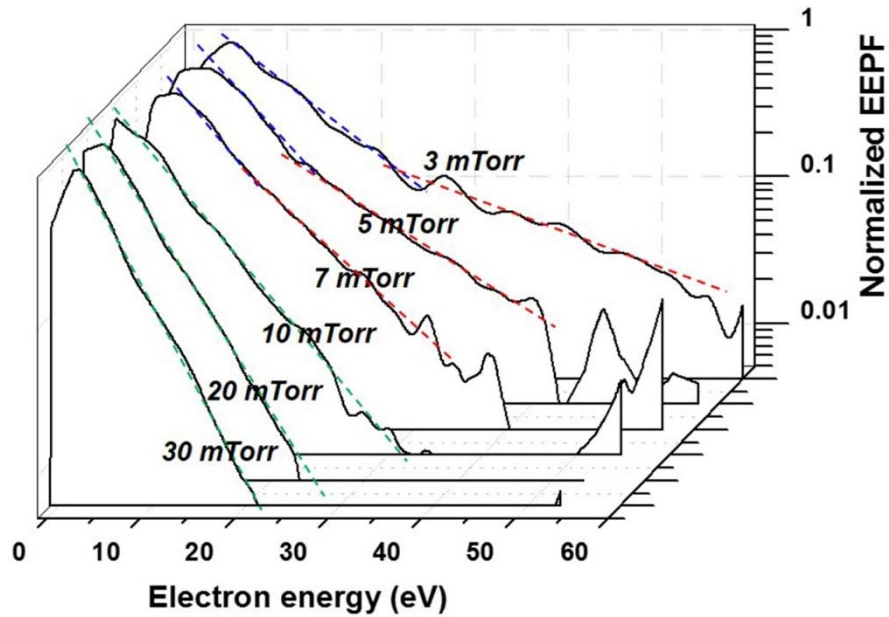


Figure 4.2 Normalized EEPFs measured at different pressures (RF power: 900W).

Normalized electron energy probability functions (EEPFs) measured in the ICP source region at different pressures and 900 W are shown in Figure 4.2. The reciprocal slope of the EEPF – energy plot in a semi-log scale represents the electron temperature if a plasma has a Maxwellian EED that is a straight line in the plot. The low- and high-pressure regimes are clearly distinct. The EEPF lines are straight in the high-pressure regime (10, 20, and 30 mTorr),

whereas the EEPFs yield two-slope structures in the low-pressure regime (3, 5, and 7 mTorr). In other words, the EED changes from Maxwellian to bi-Maxwellian as the gas pressure decreases. The bi-Maxwellization of the EED in the low pressure regime is a common phenomenon of the non-local electron kinetics. [21, 41, 125–129] This can be analyzed as follows. The orders of magnitudes of the characteristic collision frequencies (i.e., the stochastic frequency ν_{sto} , the electron – neutral collision frequency ν_{en} , and the electron – electron collision frequency ν_{ee}) can be compared to qualitatively understand the change of the EED shapes. [21, 120] (It will be discussed in more detail in the next chapter.) ν_{sto} represents the collisionless selective electron heating of high-energy electrons that can cause the bi-Maxwellization. [34] ν_{en} and ν_{ee} correspond to the collisional heating and the Maxwellization, respectively. In the low-pressure regime, ν_{sto} exceeds ν_{en} and ν_{ee} so that the plasmas are expected to show the non-local behavior and to have bi-Maxwellian EEDs (e.g., $\nu_{sto} = 31 \text{ MHz} > \nu_{en} = 1.8 \text{ MHz} > \nu_{ee} = 44 \text{ kHz}$ at 3 mTorr). On the other hand, ν_{en} is the highest characteristic frequency at high pressures and then the non-local phenomena including the bi-Maxwellization are expected to be insignificant (e.g., $\nu_{en} = 65 \text{ MHz} > \nu_{sto} = 38 \text{ MHz} > \nu_{ee} = 3.1 \text{ MHz}$ at 30 mTorr). As shown in Figure 4.2, the transition from a bi-Maxwellian to a Maxwellian EED occurs around 7 mTorr. Considering the volume ratio of the collisionless heating region (the skin layer volume) and the entire chamber within which collisions occur, ν_{en} is found to be equal to ν_{sto} at 6 mTorr that corresponds roughly to the transition pressure.

Since the global model does not cover the electron kinetics or electron heating,

the steady-state EED data obtained from electron Boltzmann equation solvers or experiments should be required. In the global model analysis of a bi-Maxwellian plasma, an EEDF can be characterized by three factors in Equation (3.1.4): $T_{e, low}$, $T_{e, high}$, and β as compared with T_e of a Maxwellian plasma. Therefore, a set of 25 nonlinear equations, as discussed in Chapter 3, are insufficient to conduct a self-consistent calculation over 27 unknowns. In this study for the analysis of the bi-Maxwellian plasmas, two unknown factors: $T_{e, high}$ and β were obtained from Figure 4.2 (the experimental data), and $T_{e, low}$ was treated as the output T_e of the model for the case of a Maxwellian EED.

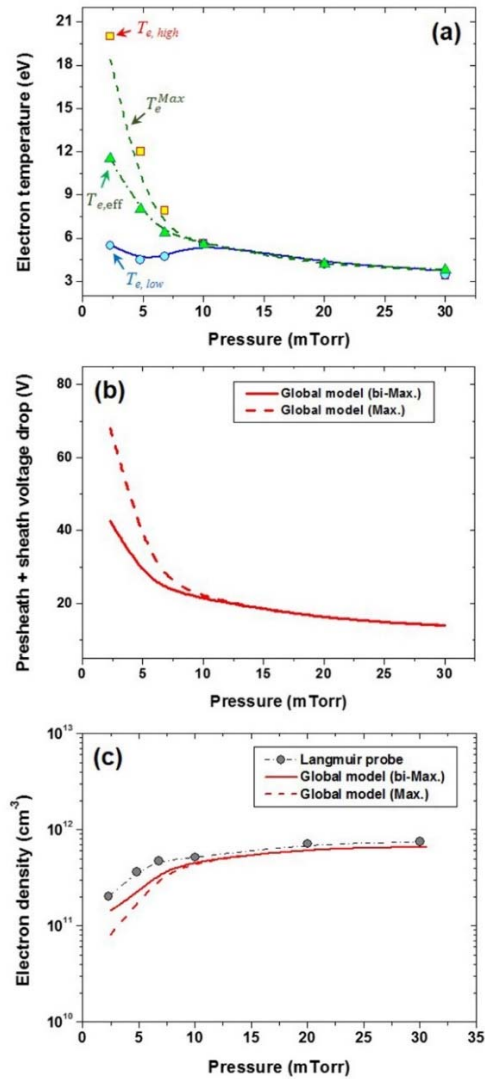


Figure 4.3 The dependence of (a) the electron density, (b) the voltage drop across the presheath and sheath regions and (c) the electron density on pressure at 900 W. Symbols denote the experimentally measured data. (For (b) and (c), the solid lines indicate the model results obtained using the measured EEDFs including the bi-Maxwellian EEDFs in the low-pressure regime; the dashed lines indicates those under the assumption that EEDFs are Maxwellian.)

Figure 4.3(a) shows the measured and calculated electron temperatures as a function of pressure. $T_{e, low}$ (circle symbols), $T_{e, high}$ (square symbols), and the effective electron temperature $T_{e, eff}$ (triangle symbols) given by the average energy integral over the EEDF [130] ($T_{e, eff} = 2/3\langle\epsilon\rangle$) are experimental data obtained from the EEDF in Figure 4.2. In addition, $T_{e, low}$ (blue solid line) and $T_{e, eff}$ (green dash dotted line) were calculated using the global model with the experimental values for $T_{e, high}$ and β . T_e^{Max} (green dashed line) is the electron temperature calculated using the global model, assuming a Maxwellian EED. A comparison of $T_{e, low}$ from the model results with experiments yields that the agreement between the model and measurement is very good. In Figure 4.3(a), the $T_{e, high}$ of a bi-Maxwellian EED decreases drastically compared to $T_{e, low}$ that slightly decreases and then increases somewhat as the pressure increases. At pressures higher than 7 mTorr, both $T_{e, high}$ and $T_{e, low}$ converge to the same electron temperature during the transition to a Maxwellian distribution. In the following, $T_{e, eff}$ defined as $T_{e, high}$ and $T_{e, low}$ of the bi-Maxwellian EED are compared with T_e^{Max} in low pressure regime. Strictly speaking, this T_e^{Max} is not realistic because only one EEDF shape (bi-Maxwellian EED in this case) are determined under a given condition (e.g., a given pressure, power, chamber and antenna geometry, etc.). T_e^{Max} serves only as a benchmark value for $T_{e, eff}$. It is interesting to note that $T_{e, eff}$ for a bi-Maxwellian EED in the low-pressure regime is lower than T_e^{Max} . As the population of high-energy electrons, which have higher rate constants of the electron impact reactions including ionization, increases with decreasing pressure, the temperature of another electron group have to be low to keep the generation reaction rates balancing the loss rates.

The existence of low $T_{e,low}$ leads to a decrease in $T_{e,eff}$. For this reason, $T_{e,eff}$ of a bi-Maxwellian EED is lower than T_e^{Max} in the low pressure regime.

A low value of $T_{e,eff}$ for a bi-Maxwellian EED accompanies a low voltage drop across the presheath and sheath regions, $V_{ps} + V_s$, and a low corresponding ion energy lost ε_i , as described in Equations (3.1.27) – (3.1.29) (see Figure 4.3(b)). Because the wall loss power density (the third term on the right hand side of Equation (3.1.26)) is roughly proportional to ε_i and the electron density, the bi-Maxwellian EED has a higher electron density to compensate the power loss related to the lower voltage drop, as shown in Figure 4.3(c). The electron densities calculated using the model were compared with the experimental measurements obtained by integrating over the EEDF. [130] Although the calculated electron densities with the bi-Maxwellian EED are slightly lower than the measured values, they show good agreements in trend with the measurements at all pressures. The serious discrepancies of the electron densities obtained using the global model with the assumption of a Maxwellian EED are due to the differences between the actual EED and the Maxwellian EED. It implies that the consideration of the EED shape in a low-pressure plasma is important for the development of an elaborate global model capable of providing accurate predictions.

4.2.2 Densities of neutral species including $H_2(v)$, the precursor of H^-

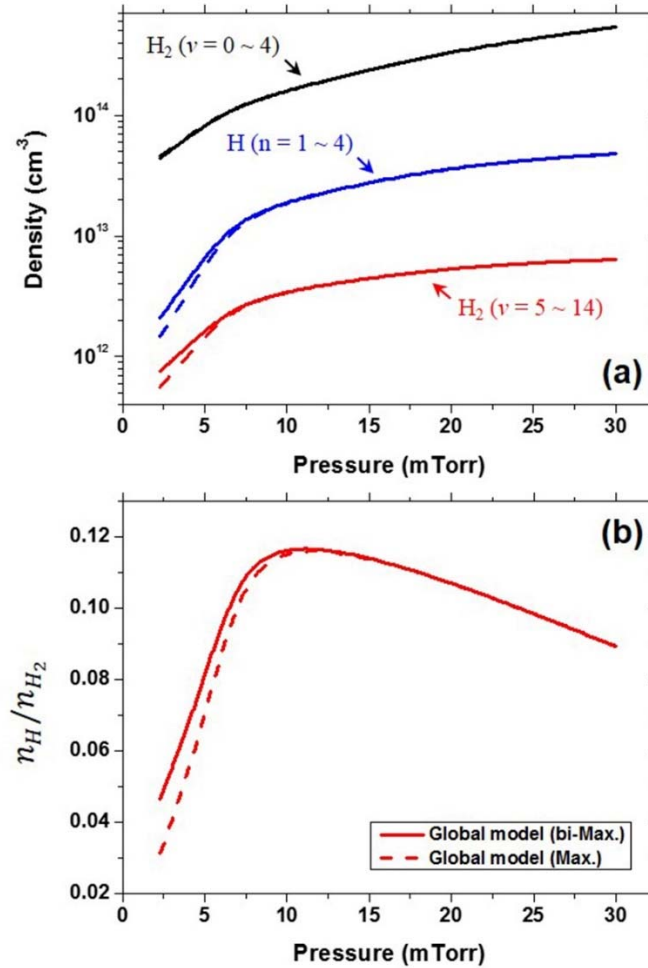


Figure 4.4 The dependence of (a) the neutral densities and (b) the atomic and molecular hydrogen density ratios on pressure at 900 W. (The solid lines indicate the model results obtained using the measured EEDFs including the bi-Maxwellian EEDFs in the low-pressure regime; the dashed lines indicates those under the assumption that EEDFs are Maxwellian.)

The densities of H ($n = 1-4$) atoms, H₂ ($v = 0-4$) molecules and H₂ ($v = 5-14$) molecules as a function of pressure are presented in Figure 4.4(a). Among these, H₂ ($v = 5-14$) molecules plays a significant role in the dissociative electron attachment producing H⁻ ions. The densities of all neutral species increase as the pressure increases. The dissociation fraction, defined as the ratio of the H ($n = 1-4$) atom density to the H₂ ($v = 0-14$) molecule density, is shown in Figure 4.4(b). The hydrogen dissociation fraction increases dramatically with increasing pressure in the low-pressure regime, and then begins decreasing with more increasing pressure. The dissociation fraction peaks around 10 mTorr, reaching a value of 12%. The model results obtained using the measured bi-Maxwellian EEDFs and those obtained using the Maxwellian EEDFs shown as the dashed lines in Figure 4.4 were compared. While there is no difference between the H₂ ($v = 0-4$) molecule densities in the case of the bi-Maxwellian and Maxwellian EEDs in the low-pressure regime, the densities of H ($n = 1-4$) atoms and H₂ ($v = 5-14$) molecules have the difference. The densities of H ($n = 1-4$) atoms and H₂ ($v = 5-14$) molecules for the bi-Maxwellian EED are higher than those obtained from the Maxwellian EED. As a consequence, the corresponding dissociation fractions are also higher. These results suggest that the bi-Maxwellian EED leads to higher dissociation and vibrational excitation rates compared to the Maxwellian EED.

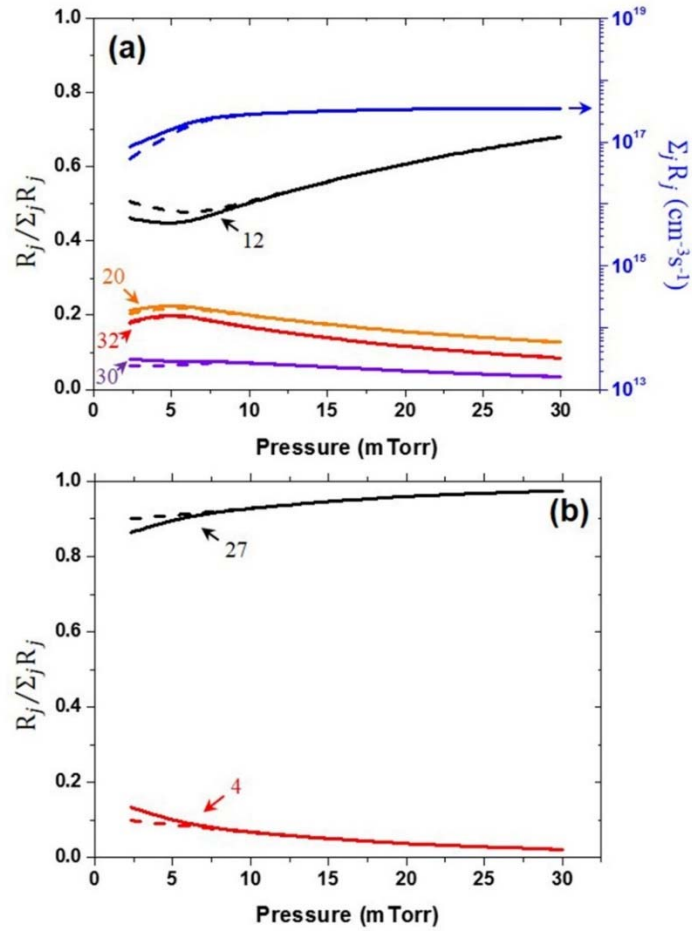


Figure 4.5 The relative reaction rates ($R_j / \sum_j R_j$) of the dominant volume and surface processes for (a) the generation and (b) the destruction of H atom as a function of pressure at 900 W. The absolute total reaction rate ($\sum_j R_j$) for the generation and destruction of H atom is given on the right side of Figure 4.5(a). Numbers on the graph denote the corresponding reactions listed in Table 3.1. (The solid lines indicate the model results obtained using the measured EEDFs including the bi-Maxwellian EEDFs in the low-pressure regime; the dashed lines indicates those under the assumption that EEDFs are Maxwellian.)

Figure 4.5 shows the absolute total reaction rate and the relative reaction rates of several major volume and surface processes for the generation and destruction of H atoms as a function of pressure. The absolute total reaction rate rises and then stays almost constant over the pressure range as shown in Figure 4.5(a). This trend is attributed to the electron impact dissociation (No. 12 in Table 3.1) that is the most dominant reaction contributing 45–65% of the H atom production processes. The electron density increases with increasing pressure, whereas the electron impact dissociation rate constant decreases due to the reduction of the effective electron temperature. In the low-pressure regime, the absolute total reaction rate grows with increasing pressure on account of the drastic increase in the electron density (see Figure 4.3(c)). A decrease in the rate constant compromises a slight increase in the electron density, resulting in the nearly constant total reaction rate above 10 mTorr. The total reaction rate for the bi-Maxwellian EEDs is higher than that for the Maxwellian EEDs in the low-pressure regime. The relative contribution of the electron impact dissociation, on the other hand, is lower for the bi-Maxwellian EED than for the Maxwellian EED. This is mainly due to the fact that the bi-Maxwellian EED, compared to the Maxwellian EED, increases the reaction rates of all H atom production reactions except for the electron impact dissociation reaction more than the electron impact dissociation reaction rate. Meanwhile, the wall neutral recombination (No. 27 in Table 3.1) of H atoms is primarily responsible for the loss of H atoms as seen in Figure 4.5(b). Its contributions exceed 80% at all pressures considered.

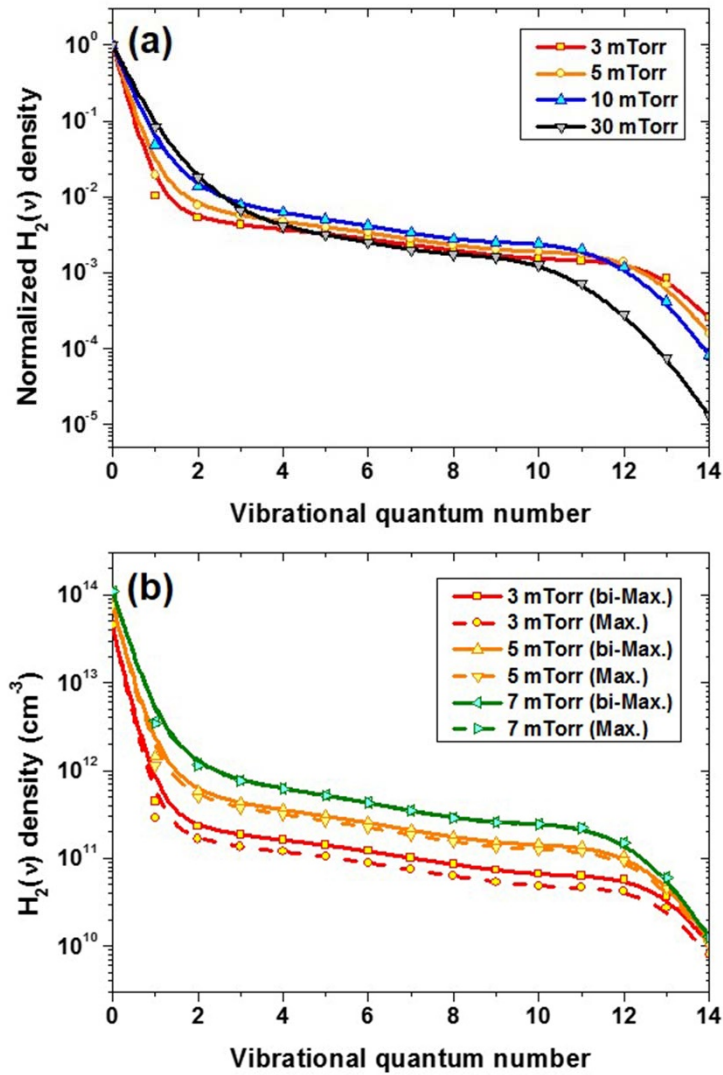


Figure 4.6 The dependence of (a) the normalized and (b) the absolute vibrationally excited H₂ molecule density on the vibrational quantum number and pressure, at 900 W. (The solid lines indicate the model results obtained using the measured EEDFs including the bi-Maxwellian EEDFs in the low-pressure regime; the dashed lines indicates those under the assumption that EEDFs are Maxwellian.)

The normalized and absolute vibrationally excited hydrogen molecule densities as a function of the vibrational quantum number and pressure are plotted in Figure 4.6. It is clear that the vibrationally excited H₂ molecule density distribution is not Boltzmann and it has a plateau at the intermediate vibrational quantum numbers between $\nu = 3$ and $\nu = 10$. Similar results were observed earlier by Mosbach. [90] Mosbach showed that the lowly and highly vibrationally excited states are populated by collisions of H₂ molecules with low- and high-energy electrons (Nos. 10 and 11 in Table 3.1), respectively. Thus, the reduction of the effective electron temperature with increasing pressure increases the populations of the lowly vibrationally excited states and decreases the populations of the highly vibrationally excited states, thereby shrinking the plateau as shown in Figure 4.6(a). In the low-pressure regime, as shown in Figure 4.6(b), the bi-Maxwellian EEDs produce higher densities of the vibrationally excited H₂ molecules compared to the Maxwellian EEDs across all values of ν . This result is ascribed to the higher reaction rates of Nos. 10 and 11 reactions in Table 3.1 due to the higher electron densities (see Figure 4.3(c)) under the bi-Maxwellian EEDs.

4.2.3 Densities of positive ions associated with H^- destruction

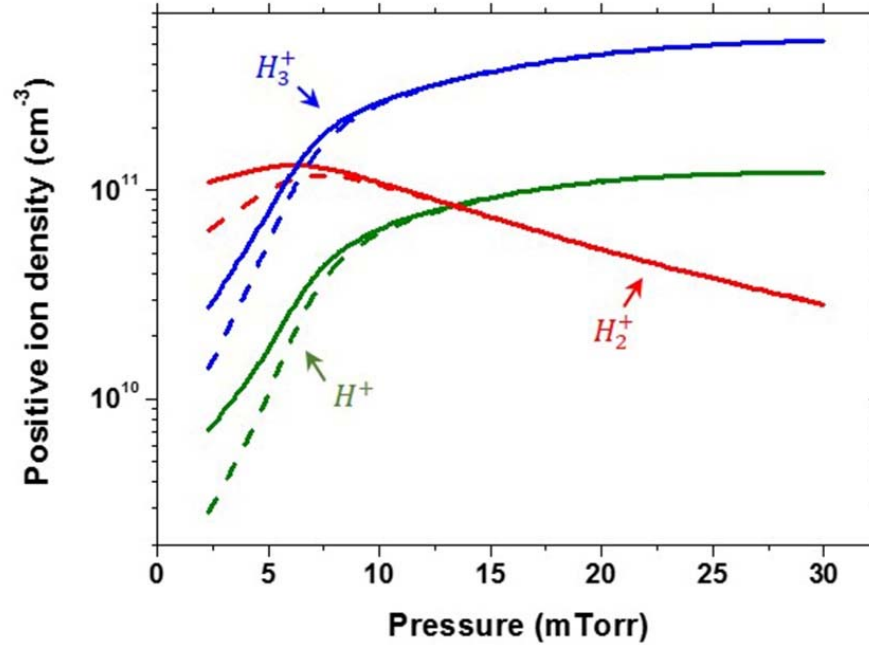


Figure 4.7 The dependence of the positive ion densities on pressure at 900 W. (The solid lines indicate the model results obtained using the measured EEDFs including the bi-Maxwellian EEDFs in the low-pressure regime; the dashed lines indicates those under the assumption that EEDFs are Maxwellian.)

Figure 4.7 shows the dependence of the positive ion densities on pressure at an RF power of 900W. All positive ions contribute to the destruction of H^- ions by the mutual neutralization. The H_2^+ and H_3^+ ions are the dominant ions in the pressure range of interest, and these ions are sensitive to the pressure. On the whole, the H_2^+ ion density decreases whereas the H_3^+ ion density

increases with increasing pressure. In the low-pressure regime below 7 mTorr, the H_2^+ ion density increases slightly with increasing pressure due directly to the drastic rise in the electron density as shown in Figure 4.3(c). The H_2^+ ion density becomes significant below pressures of around 7 mTorr, while the H_3^+ ion is the most populated ion among the positive ions at much higher pressures. The H^+ ion density, which is a relatively minor fraction of the ion densities in this regime, is more sensitive to RF power than to pressure. The H^+ ion production rate increases dramatically with the RF power, unlike the other ion species. So the H^+ ion becomes the most dominant ion at RF powers exceeding a certain value, as investigated by Zorat and Vender. [56] Though the H^+ ion density increases with pressure, its rate of increase with respect to pressure is much smaller than that of the H_3^+ ion density. This can obviously be seen in the linear-scaled Figure 4.7. A comparison between the EED conditions reveals that the positive ion densities obtained under a bi-Maxwellian EED are higher than those obtained under a Maxwellian EED in the low-pressure regime. The ratios of the positive ion density under the bi-Maxwellian EED to that under the Maxwellian EED for the H^+ , H_2^+ , and H_3^+ ions are in the following order (highest to lowest): $H^+ > H_3^+ > H_2^+$.

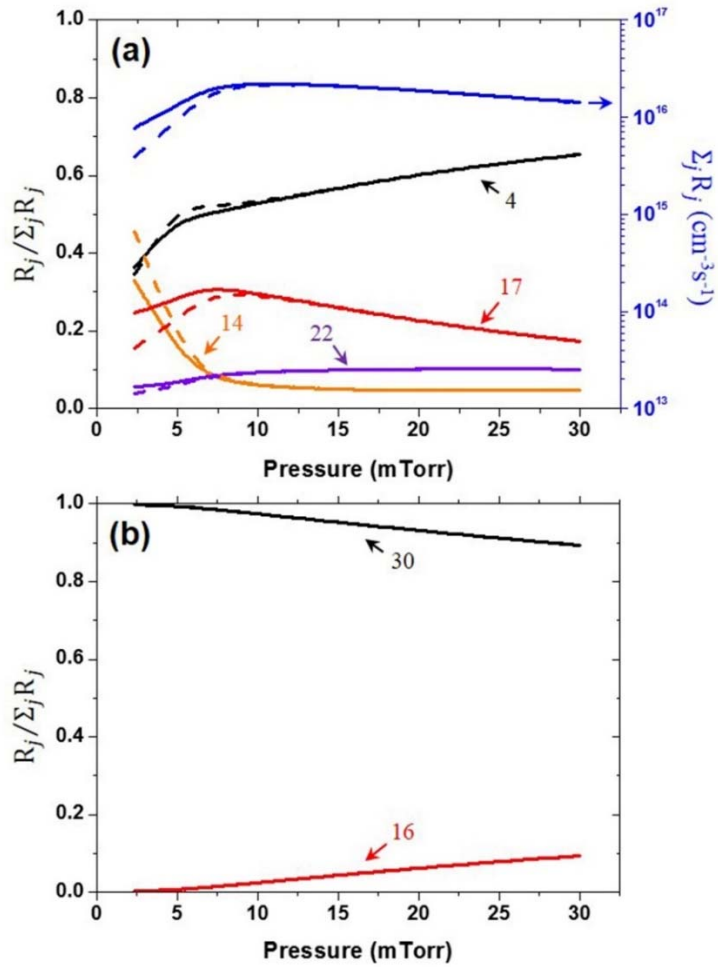


Figure 4.8 The relative reaction rates of the dominant volume and surface processes for (a) the generation and (b) the destruction of H^+ ions as a function of pressure at 900 W. The absolute total reaction rate is given on the right side of Figure 4.8(a). Numbers on the graph denote the corresponding reactions listed in Table 3.1. (The solid lines indicate the model results obtained using the measured EEDFs including the bi-Maxwellian EEDFs in the low-pressure regime; the dashed lines indicates those under the assumption that EEDFs are Maxwellian.)

Figure 4.8 shows the absolute total reaction rate and the relative reaction rates of the dominant volume and surface processes for the generation and destruction of H^+ ions as a function of pressure. The absolute total reaction rate reaches a peak value around 10 mTorr. This can be explained as follows. All major H^+ ion production processes plotted in Figure 4.8(a) are electron impact collision reactions. The absolute total reaction rate is proportional to the corresponding rate constants and electron density. Thus, increasing the electron density and decreasing the rate constants by reducing $T_{e, \text{eff}}$ with increasing pressure changes the absolute total reaction rate. The increase in the electron density is mainly responsible for an increase of the absolute total reaction rate at low pressures below 10 mTorr, whereas the decrease in the rate constants largely contributes to a decrease of the absolute total reaction rate at higher pressures. These effects together produce a peak on the graph of the absolute total reaction rate versus pressure. Compared to the Maxwellian EED case, the bi-Maxwellian EED case has a higher electron density and lower the rate constants. Since the increased electron density prevails over the rate constant reduction, the absolute total reaction rate in the bi-Maxwellian EED is higher than that in the Maxwellian EED.

The most dominant contributor of H^+ ion formation is the direct ionization of atomic hydrogen (No. 4 in Table 3.1.) and the relative contribution of this reaction increases with increasing pressure as shown in Figure 4.8(a). Nevertheless, the contribution seems to be largely unaffected by the change in EED because it is compensated by the contributions of the next two most dominant reactions. The ranking of the second and third dominant contributors

changes, depending on pressure. The second dominant contributor is the dissociative ionization of H_2 molecules (No. 14 in Table 3.1) and the third dominant contributor is the dissociative excitation of H_2^+ ions (No. 17 in Table 3.1) below pressures of 4 mTorr. The increase in pressure sharply decreases the reaction rate of reaction No. 14 for which high-energy electrons are effective. Therefore, the ranking is reversed at higher pressures. In the meantime, the relative reaction rate of the reaction No. 14 is lower whereas the rate of the reaction No. 17 is higher for the bi-Maxwellian EED compared to those for the Maxwellian EED in the low-pressure regime. These results arise from the fact that the lower $T_{e,eff}$ of the bi-Maxwellian EED and the higher $T_{e,eff}$ of the Maxwellian EED are more favorable to the reaction No. 17 and No. 14, respectively, due to the intrinsic characteristics of their cross sections. In Figure 4.8(b), the main H^+ ion loss process is the H^+ neutralization at the wall, contributing over 90% of the processes. There is no significant difference between the relative reaction rates for the two EEDs.

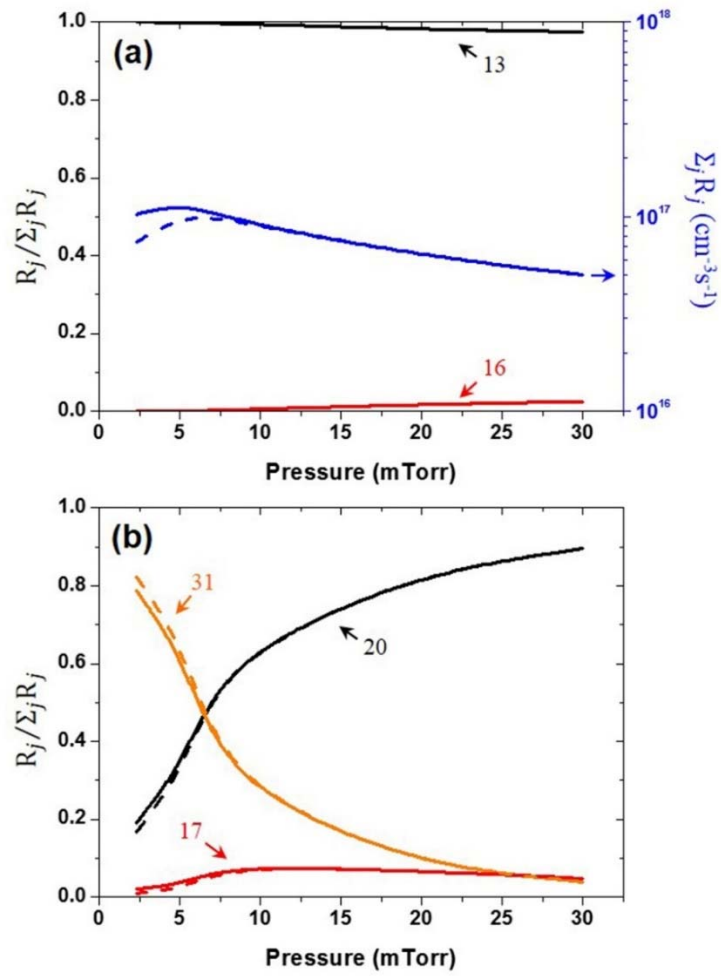


Figure 4.9 The relative reaction rates of the dominant volume and surface processes for (a) the generation and (b) the destruction of H_2^+ ions as a function of pressure at 900 W. The absolute total reaction rate is given on the right side of Figure 4.9(a). Numbers on the graph denote the corresponding reactions listed in Table 3.1. (The solid lines indicate the model results obtained using the measured EEDFs including the bi-Maxwellian EEDFs in the low-pressure regime; the dashed lines indicates those under the assumption that EEDFs are Maxwellian.)

The absolute total reaction rate and the relative reaction rates of the dominant volume and surface processes for the generation and destruction of H_2^+ ions as a function of pressure are shown in Figure 4.9. The trend in the absolute total reaction rate for the H_2^+ ion generation and destruction as a function of pressure and EED shape is similar to that for the H^+ ion generation and destruction because the most dominant H_2^+ ion production process is also an electron impact collision reaction. For H_2^+ ions, the peak of the absolute total reaction rate is at around 5 mTorr. The non-dissociative ionization of hydrogen molecules (No. 13 in Table 3.1) accounts for most of the relative contribution of the H_2^+ ion formation, and it remains almost unchanged across all pressures as shown in Figure 4.9(a). Figure 4.9(b) shows that two primary reactions, i.e., H_2^+ neutralization at the wall (No. 31 in Table 3.1) and H_3^+ ion formation (No. 20 in Table 3.1), contribute to the loss of H_2^+ ions. The wall H_2^+ neutralization is dominant at pressures below 7 mTorr, and is decreased as pressure increases. On the other hand, the H_3^+ ion formation increases with increasing pressure, then its contribution reaches almost 90% at 30 mTorr. The relative reaction rates of the reactions No. 31 and No. 20 for a bi-Maxwellian EED with a low $T_{e, \text{eff}}$ are slightly lower and higher, respectively, than those for a Maxwellian EED.

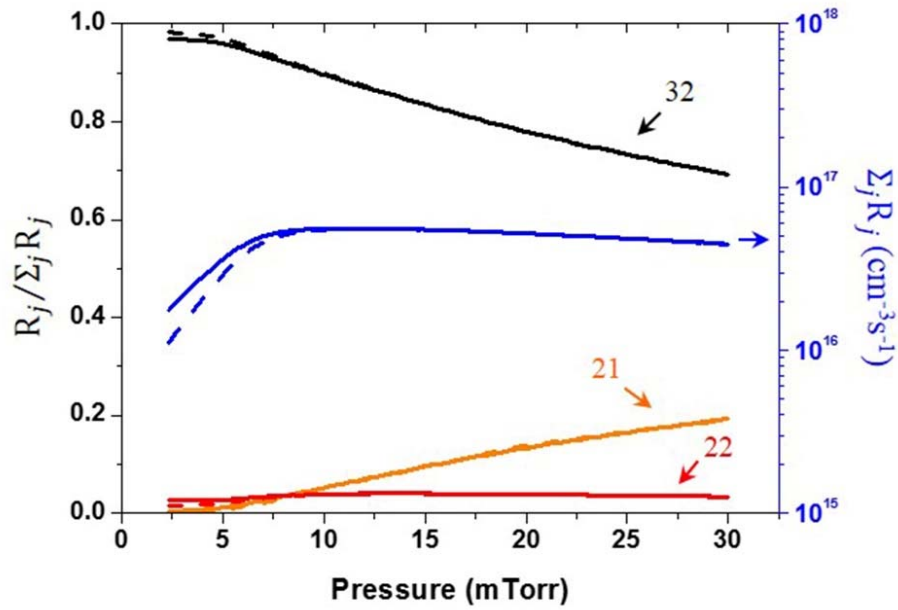


Figure 4.10 The relative reaction rates of the dominant volume and surface processes for the destruction of H_3^+ ions as a function of pressure at 900 W. The relative reaction rate of the reaction No. 20 listed in Table 3.1 ($R_j / \sum_j R_j = 1$) is not plotted for reasons of convenience because the reaction No. 20 is the only considered reaction for the H_3^+ ion production. The absolute total reaction rate is given on the right side of the graph. Numbers on the graph denote the corresponding reactions listed in Table 3.1. (The solid lines indicate the model results obtained using the measured EEDFs including the bi-Maxwellian EEDFs in the low-pressure regime; the dashed lines indicates those under the assumption that EEDFs are Maxwellian.)

Figure 4.10 shows the absolute total reaction rate and the relative reaction rates of the dominant volume and surface processes for H_3^+ ions versus pressure. H_3^+ ion formation (No. 20 in Table 3.1.) is the only considered reaction for the

creation of H_3^+ ions in the model. Its relative reaction rate, which is 1, is omitted from the plot for reasons of convenience. The absolute total reaction rate associated with the H_3^+ ion generation and destruction is exclusively determined by the H_2^+ ion density and H_2 molecule density involved in the H_3^+ ion formation reaction. Both the H_2^+ ion density (see Figure 4.7) and H_2 molecule density increase with pressure at pressures below 8 mTorr, resulting in an increase in the absolute total reaction rate. In addition, the absolute total reaction rate for a bi-Maxwellian EED is higher than that obtained for a Maxwellian EED due to higher H_2^+ ion density for a bi-Maxwellian EED. The absolute total reaction rate is nearly constant at pressures above 8 mTorr because the increase in H_2 molecule density with increasing pressure is comparable to the decrease in the H_2^+ ion density. The main reaction that contributes to the destruction of H_3^+ ions is the wall H_3^+ neutralization (No. 32 in Table 3.1). The relative reaction rate of the most dominant volume loss reaction, i.e., H_3^+ dissociative recombination (No. 21 in Table 3.1) increases gradually with pressure, contributing at most roughly 20% of the H_3^+ ion destruction at 30 mTorr. The relative reaction rates for the H_3^+ ion generation and destruction do not change noticeably with the EED shape, unlike those for the generation and destruction of other positive ions.

4.2.4 Negative ion density

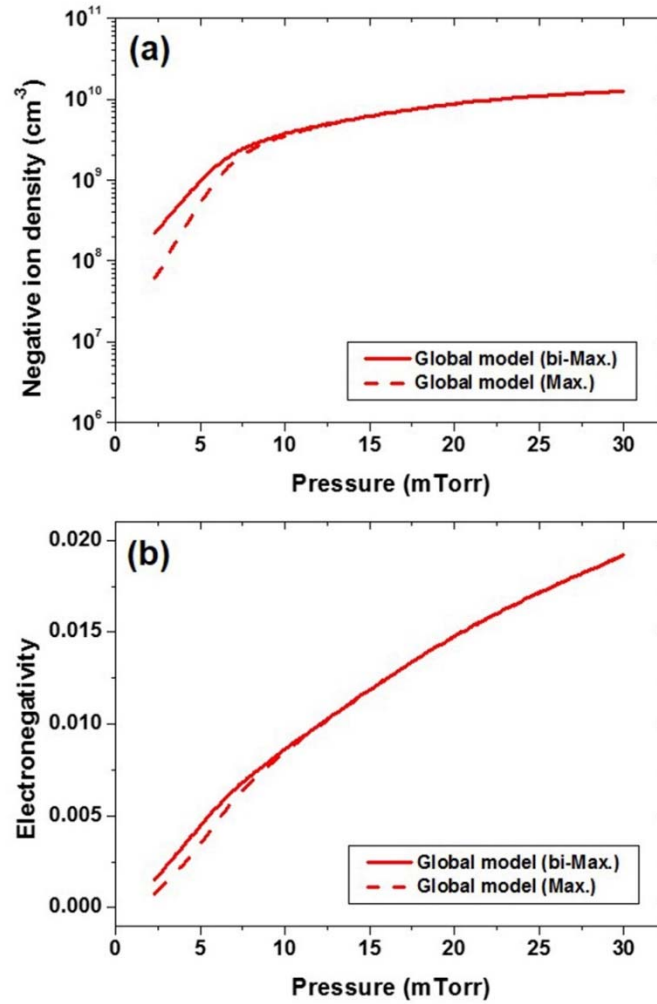


Figure 4.11 The dependence of (a) the negative ion density and (b) the central electronegativity on pressure at 900 W. (The solid lines indicate the model results obtained using the measured EEDFs including the bi-Maxwellian EEDFs in the low-pressure regime; the dashed lines indicates those under the assumption that EEDFs are Maxwellian.)

The dependence of the H^- ion density and central electronegativity on pressure at an RF power of 900 W are presented in Figure 4.11. The H^- ion density over the pressure range considered is nearly one or two orders of magnitude lower than the positive ion densities shown in Figure 4.7. As the pressure increases, the H^- ion density increases from $2.2 \times 10^8 \text{ cm}^{-3}$ at 3 mTorr to $1.3 \times 10^{10} \text{ cm}^{-3}$ at 30 mTorr for the bi-Maxwellian EED as shown in Figure 4.11(a). The H^- ion density in the Maxwellian EED is lower than that in the bi-Maxwellian EED, especially 3.6 times lower at 3 mTorr. As can be seen in Figure 4.11(b), the central electronegativity also increases with increasing pressure, reaching a value of about 2% at 30 mTorr. The small central electronegativities indicate that the low-pressure hydrogen plasma is weakly electronegative. There is not much difference between electronegativities for the bi-Maxwellian and Maxwellian EEDs. It implies that the density ratios of the electron and H^- ion for the bi-Maxwellian and Maxwellian EEDs are similar.

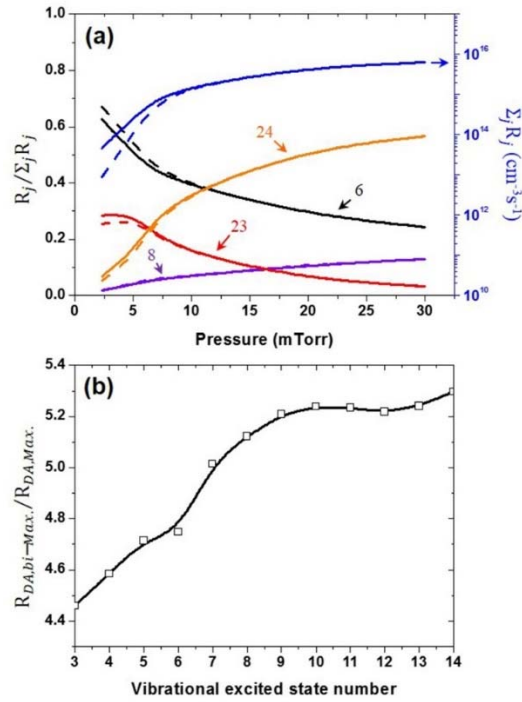


Figure 4.12 The relative reaction rates of the dominant volume and surface processes for the destruction of H^- ions as a function of pressure at 900 W. The relative reaction rate of the reaction No. 15 listed in Table 3.1 ($R_j / \sum_j R_j = 1$) is not plotted for reasons of convenience because the reaction No. 15 is the only considered reaction for the H^- ion production. The absolute total reaction rate is given on the right side of the graph. Numbers on the graph denote the corresponding reactions in Table 3.1. (The solid lines indicate the model results obtained using the measured EEDFs including the bi-Maxwellian EEDFs in the low-pressure regime; the dashed lines indicates those under the assumption that EEDFs are Maxwellian.) (b) The ratio of the absolute dissociative electron attachment reaction rate (R_{DA}) for a Maxwellian EED and that for a Maxwellian EED as a function of the vibrational quantum number ($\nu = 3-14$) at 3 mTorr and 900 W.

Figure 4.12 reveals that the H^- ions are destroyed and generated at different pressures. The absolute total reaction rate and relative reaction rates of the dominant volume and surface processes for H^- ions as a function of pressure are plotted in Figure 4.12(a). The dissociative electron attachment (No. 15 in Table 3.1) is the only considered reaction for the creation of H^- ions in the model. Its relative reaction rate, which is 1, is also omitted from the plot for reasons of convenience, as well as the relative reaction rate of the H_3^+ ion formation. Indeed, H^- ions are mainly volume-produced via the dissociative electron attachment by collisions of the highly vibrationally excited states, H_2 ($v = 5-14$), with low-energy electrons. The dissociative electron attachment also requires high-energy electrons that efficiently generate the highly vibrationally excited states. The absolute total reaction rate of the dissociative electron attachment increases drastically with pressure at low pressures below 8 mTorr, and then it increases more slowly with a further increase in pressure. The trend in the total reaction rate follows the changes in the densities of the electrons and H_2 ($v = 5-14$) molecules, which are reactants involved in the dissociative electron attachment, under varying pressure (see Figure 4.3(c) and also Figure 4.4(a)).

Meanwhile, the bi-Maxwellian EED in the low-pressure regime gives advantageous conditions with abundant low-energy electrons (characterized by a lower $T_{e,\text{eff}}$ and a higher electron density) and highly vibrationally excited states for the dissociative electron attachment. For this reason, the H^- ion density for a bi-Maxwellian EED is higher than that obtained for a Maxwellian EED. Figure 4.12(b) shows the ratio of the absolute dissociative electron

attachment reaction rates for the bi-Maxwellian EED and the Maxwellian EED as a function of the vibrational quantum number at 3 mTorr and 900 W. The ratio increases with increasing the vibrational quantum number in general, exceeding 5 for $v = 7-14$. It implies that the transition from a Maxwellian EED to a bi-Maxwellian EED efficiently promotes the dissociative electron attachments of the higher vibrationally excited states.

For the destruction of H^- ions, the electron detachment (No. 6 in Table 3.1) and the $H_3^+ - H^-$ mutual neutralization (No. 24 in Table 3.1) are the two most dominant reactions. The electron detachment, which is enhanced by the presence of energetic electrons, is most dominant at low pressures below 12 mTorr. As the H_3^+ ion density increases with pressure, the absolute reaction rate of the $H_3^+ - H^-$ mutual neutralization grows remarkably, and its relative reaction rate becomes most significant at higher pressures. By contrast, other relative reaction rates are relatively diminished. The relative reaction rates of Nos. 23 and 24 reactions for a bi-Maxwellian EED are higher than those for a Maxwellian EED, while the relative reaction rate of No. 6 is lower.

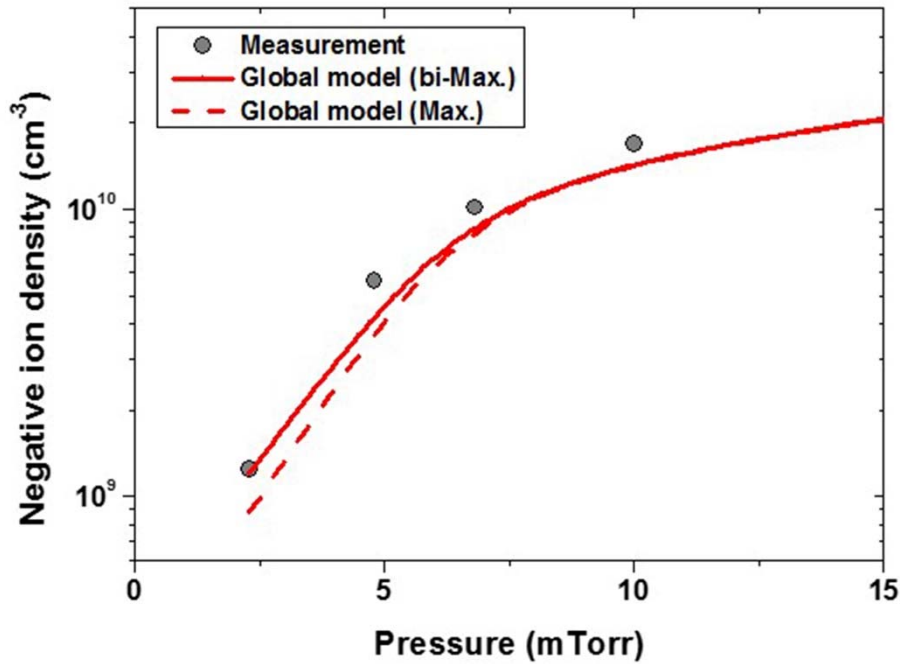


Figure 4.13 The dependence of negative ion density in the vicinity of the magnetic filter on pressure at 900 W. Symbols denote the experimental data measured using the laser photodetachment technique. (The solid lines indicate the model results obtained using the measured EEDFs including the bi-Maxwellian EEDFs in the low-pressure regime; the dashed lines indicates those under the assumption that EEDFs are Maxwellian.)

Figure 4.13 shows a comparison of the measured and calculated H^- ion densities in the vicinity of the magnetic filter under varying pressure at 900 W. The H^- ion densities over the pressure range considered are approximately one order of magnitude higher than the central negative ion densities plotted in Figure 4.11(a) due to the presence of the magnetic filter. Since the magnetic filter reduces the electron temperature in the vicinity of the filter regardless of

the EED shape associated with the population of low-energy electrons, the difference between the calculated H^- ion densities for the bi-Maxwellian and Maxwellian EEDs, as shown in Figure 4.13, arises primarily from the difference between the central highly vibrationally excited H_2 molecule densities. Therefore, the H^- ion density difference for the bi-Maxwellian and Maxwellian EEDs in the vicinity of the filter is smaller than the central H^- ion density difference (see Figure 4.11(a)). This H^- ion density difference may be increased as the bi-Maxwellization process becomes dominant. The H^- ion densities obtained from the model under the actual bi-Maxwellian EED accurately follow the experimentally measured values at various pressures, especially low pressure regime.

Chapter 5. H⁻ ion generation enhanced by ICP

heating

In the previous chapter, it is found that the densities of H⁻ ions and their precursors (i.e., highly vibrationally excited hydrogen molecules for the volume H⁻ ion production and hydrogen atoms for the surface H⁻ ion production) for the bi-Maxwellian EED are higher than those for the Maxwellian EED. The transition from a Maxwellian EEDF to a bi-Maxwellian EEDF, the bi-Maxwellization, can usually be achieved by lowering the pressure. (See Figure 4.2) However, as mentioned in Chapter 1, the pressure is not a control knob for the bi-Maxwellian because the pressure in an ion source should be low enough to minimize the stripping losses of H⁻ ions in the extraction system. In this chapter, the driving frequency regarding the collisionless heating as a control knob will be investigated, and the dual frequency antenna ICP as the RF driven H⁻ ion source driver will also be proposed. The qualitative analysis on the characteristic collision frequencies to determine a change of EED by ICP heating and the global model analysis to predict an increase in H⁻ ion density by the change of EED are carried out.

5.1 Experimental setup

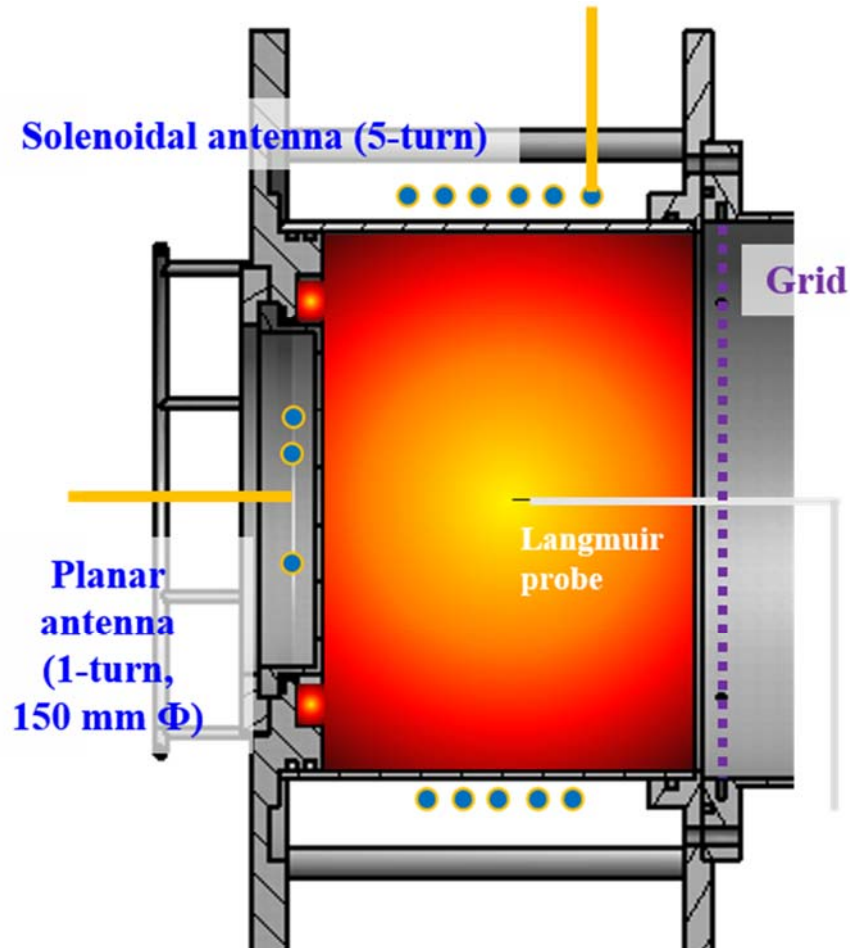


Figure 5.1 Schematic diagram of dual frequency antenna ICP.

A schematic diagram of the experimental setup is depicted in Figure 5.1. In order to investigate the driving frequency as a control knob, a cylindrical plasma chamber has been designed to install two antennas. Two different frequencies for two antennas were selected for the reason as follows. In general,

the RF ion source is biased with respect to the ground for the beam extraction and then an RF power is fed to an antenna through an insulating transformer. Because the transformer efficiency increases with decreasing the driving frequency, low frequencies of 1–2 MHz have been widely used in RF driven H^- ion sources. [21, 131, 132] Besides, the low frequencies are advantageous to lower antenna voltage. High frequencies (e.g., 13.56 MHz), on the other hand, can promote the collisionless heating to produce high-energy electrons efficiently. As reviewed in Subsection 2.4.2, the ratio of collisionless power absorption to collisional power absorption has a maximum at about 13.56 MHz. [44] Accordingly, frequencies of 2 and 13.56 MHz were chosen as low and high frequencies for different functions mentioned above.

The one-turn loop planar antenna with diameter of 15 cm is located on the quartz plate at the top of the chamber, and RF power at 13.56 MHz is applied to it. Another five-turn solenoidal antenna feeding RF power at 2 MHz is close to circumference of the chamber. RF powers at two different frequencies can be controlled independently though each individual RF power supply and matcher. Experiments have been carried out at fixed operating pressure of 5 mTorr H_2 and RF powers ranging up to 3 kW for 2 MHz and up to 5 kW for 13.56 MHz. The chamber has a diameter of 30 cm and a length of 23 cm.

Plasma properties have been measured using a RF compensated cylindrical Langmuir probe which is placed at the center of the chamber. The tungsten tip of the probe has a diameter of 0.3 mm and a length of 2 mm. The probe was designed to fulfill the requirement of Equation (2.5.4) for first three harmonics of 2 and 13.56 MHz. $Z_{circuit}$ impedances of the notch filter circuits in the probe

at the harmonic frequencies are shown in Figure 5.2.

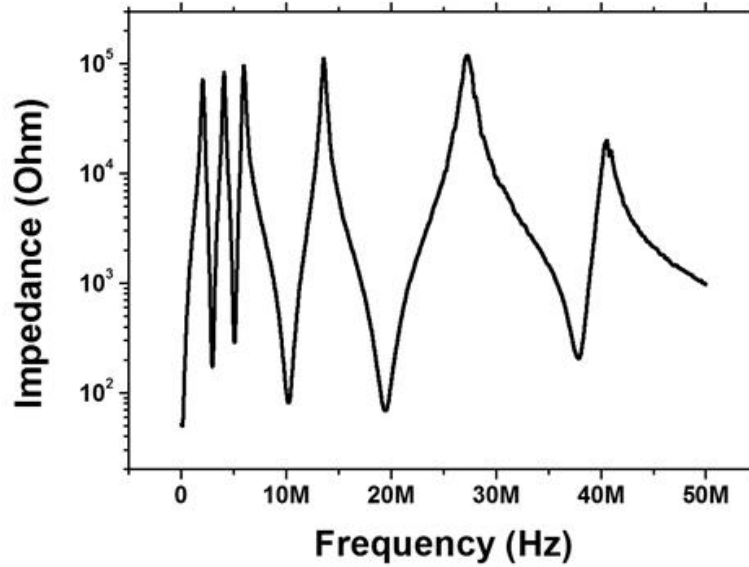


Figure 5.2 Measured impedance $Z_{circuit}$ of the notch filter circuits in the probe at the harmonic frequencies of 2 and 13.56 MHz.

To avoid the thermal damage of the notch filter circuits and then to increase the heat-resisting capability of the probe, the water-cooling jacket was introduced. EEPFs and EEDFs were obtained using the Druyvesteyn method. [130] From EEPFs and EEDFs, the electron temperature $T_{e, max}$ in the case of Maxwellian EEDF, the electron temperature of low- and high-energy electron groups $T_{e, low}$ and $T_{e, high}$, the density ratio of the high-energy electron to the total electron β in the case of bi-Maxwellian EEDF, and electron density, n_e , were calculated.

Since there is no diagnostic tool for measuring H^- ions and their precursors in the dual frequency antenna ICP, the dependence of H atom and H^- ion

densities on EED in the dual frequency antenna ICP was evaluated using the developed global model.

5.2 Bi-Maxwellization of the dual frequency antenna ICP

Compared to the conventional single frequency antenna ICP, the dual frequency antenna ICP can be characterized by two phenomena, i.e., increase of the power absorbed by the plasma and the Bi-Maxwellization enhanced by the collisionless heating.

5.2.1 Increase of the power absorbed by the plasma in the dual antenna mode

Figure 5.3 shows the electron densities as a function of total RF power P_{total} for single and dual antenna modes in the ICP.

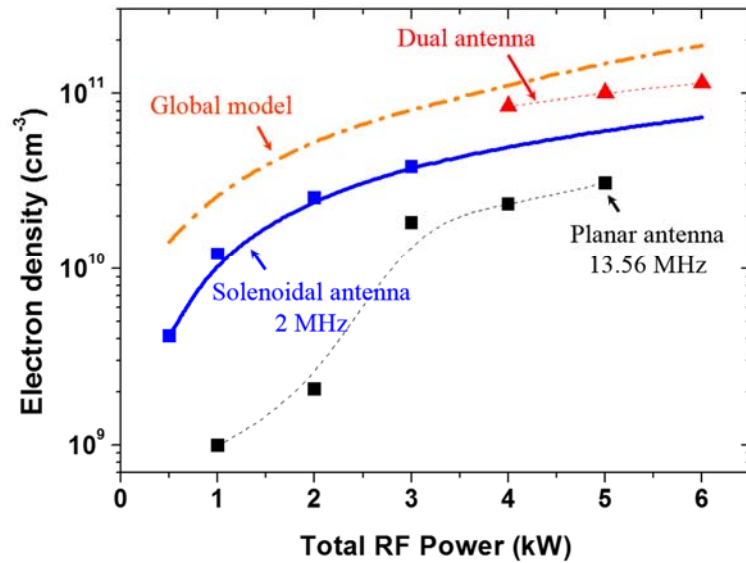


Figure 5.3 Electron densities versus total RF power in single and dual antenna modes in the ICP. In dual antenna modes, RF power of the solenoidal antenna is fixed at 2 kW and only RF power of the planar antenna is varied. Symbols denote experimental data measured, and the dash-dot ($P_{abs}/P_{total} = 1$) and solid line represents the global model result.

Density of the single frequency solenoidal antenna mode is higher than that of the single frequency planar antenna mode at the same total RF power P_{total} . This is attributed to difference in their power absorbed by plasma (or RF discharge power) P_{abs} . As discussed in the transformer model part of Subsection 2.4.2, P_{total} is consumed in P_{abs} and the power dissipated in the coil P_{coil} . [37, 133] Because plasma is regarded as the one-turn secondary coil of a transformer in the model, configuration of the antenna is crucial to determine the coupling

coefficient between an antenna coil and a plasma coil, and also P_{abs} or power transfer efficiency P_{abs}/P_{total} . Compared to the planar antenna, the solenoidal antenna with larger number of turns has so higher coupling coefficient and P_{abs}/P_{total} that its density is higher. Additionally, a drastic density evolution between 2 and 3 kW of single frequency planar antenna mode is ascribed to the E – H mode transition. [134] It is interesting to note that electron densities of dual antenna modes are higher than those of single antenna modes at the same P_{abs} . This can be explained as follows. For a fixed coil current, the inductive P_{abs} increases linearly with the electron density (see Regime A in Figure 5.4), and then decays with the square root of the electron density (See Regime B in Figure 5.4). [37]

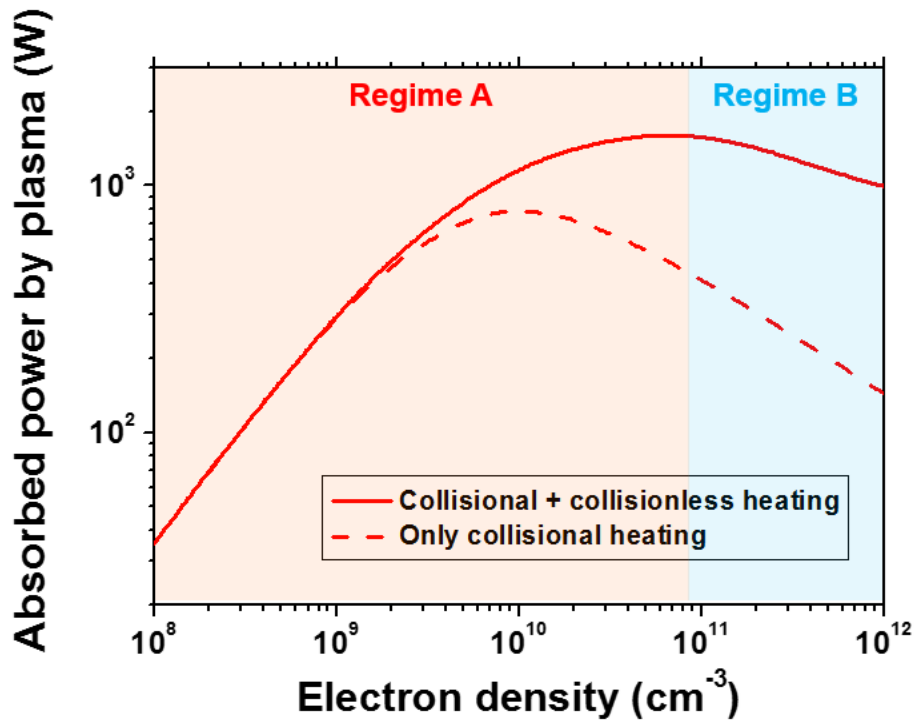


Figure 5.4 Dependence of the absorbed power by plasma on the electron density in the ICP. This is the electromagnetic model results calculated using Equation (3.2.16) (frequency: 2 MHz, RF power: 2 kW, pressure: 5 mTorr, antenna current: 13 A, and electron temperature: 6 eV).

It was confirmed that all experimental conditions with the electron density near skin layers in Figure 5.3 belong to the regime A using transformer model analysis. [33, 120, 134–137] Consequently, P_{abs} or P_{abs}/P_{total} of each antenna in the dual antenna mode can be increased with a rise in electron density caused by another antenna. This effect leads to higher total P_{abs} and then higher the electron density in the dual antenna mode compared to those of the single

antenna mode. P_{abs}/P_{total} can be calculated using results from the global model with the transformer model. At $P_{total} = 5$ kW, P_{abs}/P_{total} are 23, 45 and 74% for planar, solenoidal and dual antenna mode, respectively. Here, densities of single frequency solenoidal antenna mode at P_{total} more than 3 kW are estimated by using global model and experimental results. Owing to higher P_{abs}/P_{total} , only dual frequency antenna mode can reach more than $8 \times 10^{10} \text{ cm}^{-3}$ at $P_{total} < 6$ kW.

5.2.2 Bi-Maxwellization enhanced by collisionless heating

To study how changes of the electron density in the single and dual frequency antenna modes can affect ICP heating and the related competition between Maxwellization and bi-Maxwellization, a qualitative analysis on the characteristic collision frequencies has been carried out. [21, 120] The dependence of the characteristic collision frequencies on the electron density at 5 mTorr H₂ is presented in Figure 5.5.

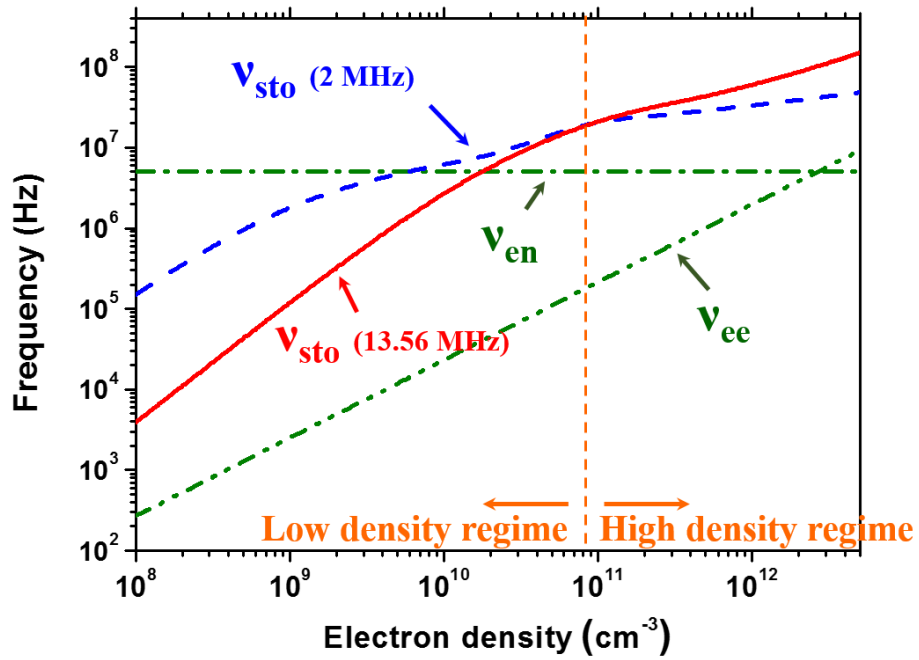


Figure 5.5 Dependence of collision frequencies, i.e., stochastic frequencies v_{sto} for $\omega = 2$ MHz and 13.56 MHz, electron – neutral collision frequency v_{en} , and electron – electron collision frequency v_{ee} on electron density at 5 mTorr H_2 .

The stochastic frequency, v_{sto} , electron – neutral collision frequency, v_{en} , and electron – electron collision frequency, v_{ee} , are parameters which represent collisionless heating, collisional heating, and Maxwellization, respectively. By comparison of these parameters, competition between Maxwellization and bi-Maxwellization of EED can be qualitatively analyzed. When stochastic frequency is higher than other frequencies, the stochastic heating dominates the heating process so that bi-Maxwellization takes place. For inverse case, Maxwellization occurs. In Figure 5.5, stochastic frequencies and electron – electron collision frequency are increased with increasing the electron density.

Of the two stochastic frequencies, stochastic frequency for $\omega = 13.56$ MHz especially increases with larger slope. The graph can be classified into two electron density regimes associated with the single and dual frequency antenna mode. The vertical dashed orange line in Figure 5.5 represents $8 \times 10^{10} \text{ cm}^{-3}$ at which two distinct regimes are divided. For the high density regime of dual frequency antenna mode, stochastic frequencies, particularly for $\omega = 13.56$ MHz, are higher than other frequencies. It implies that stochastic heating dominates the heating process, and then corresponding EEDs may have a two-temperature structure by the bi-Maxwellization. It has to be further noted here that $\omega = 13.56$ MHz is more effective, compared to $\omega = 2$ MHz, for the bi-Maxwellization in the high density regime owing to its higher stochastic frequency. This dependence on frequency ω accords with the results of Godyak *et al.* and Vahedi *et al.* [44, 120] Maxwellian EED in the low density regime, on the other hand, may be expected because stochastic heating cannot dominate the heating process.

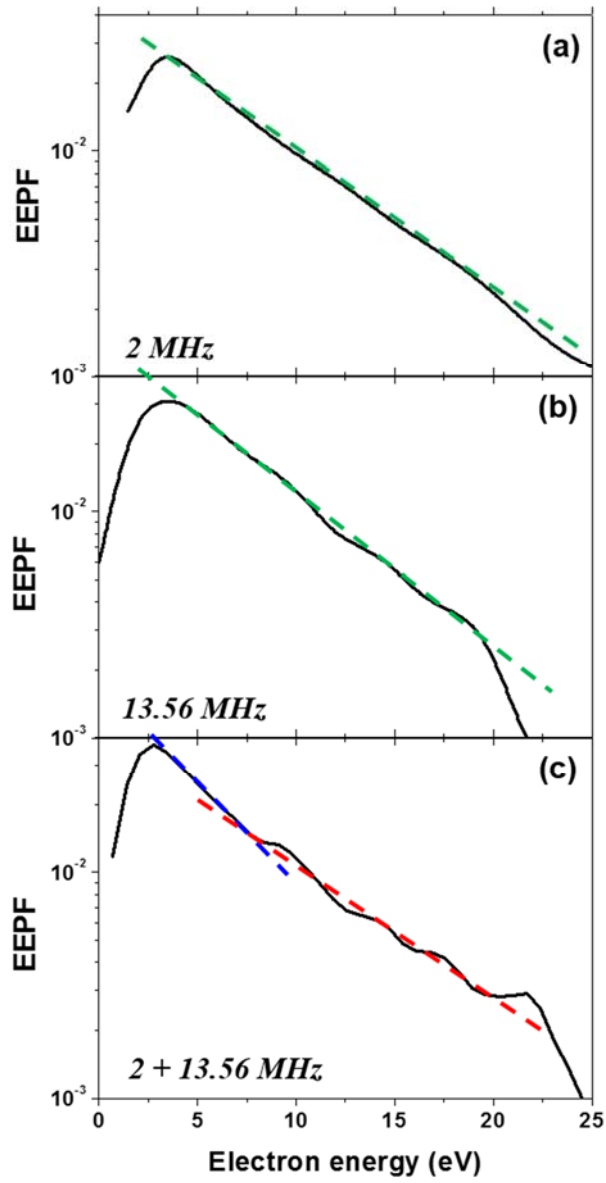


Figure 5.6 Normalized EEPFs of (a) 2 MHz single frequency antenna mode at 2 kW (b) 13.56 MHz single frequency antenna mode at 4 kW and (c) dual frequency antenna mode at 6 kW (2 MHz 2 kW + 13.56 MHz 4 kW).

The normalized EEPFs of single and dual frequency antenna modes are plotted in Figure 5.6. Conditions of 2 MHz single frequency antenna mode at 2 kW, and 13.56 MHz single frequency antenna mode at 4 kW were chosen for a comparison since their electron densities are almost the same for both conditions. It implies that P_{abs} of these two conditions are nearly the same. (see subsection 2.4.2) As expected above, EEPFs of single frequency antenna modes show the Maxwellian EEDs, while that of dual frequency antenna mode seems to be bi-Maxwellian EED with a two-temperature structure.

The normalized EEPF evolutions with RF powers at 2 and 13.56 MHz were also investigated as shown in Figure 5.7.

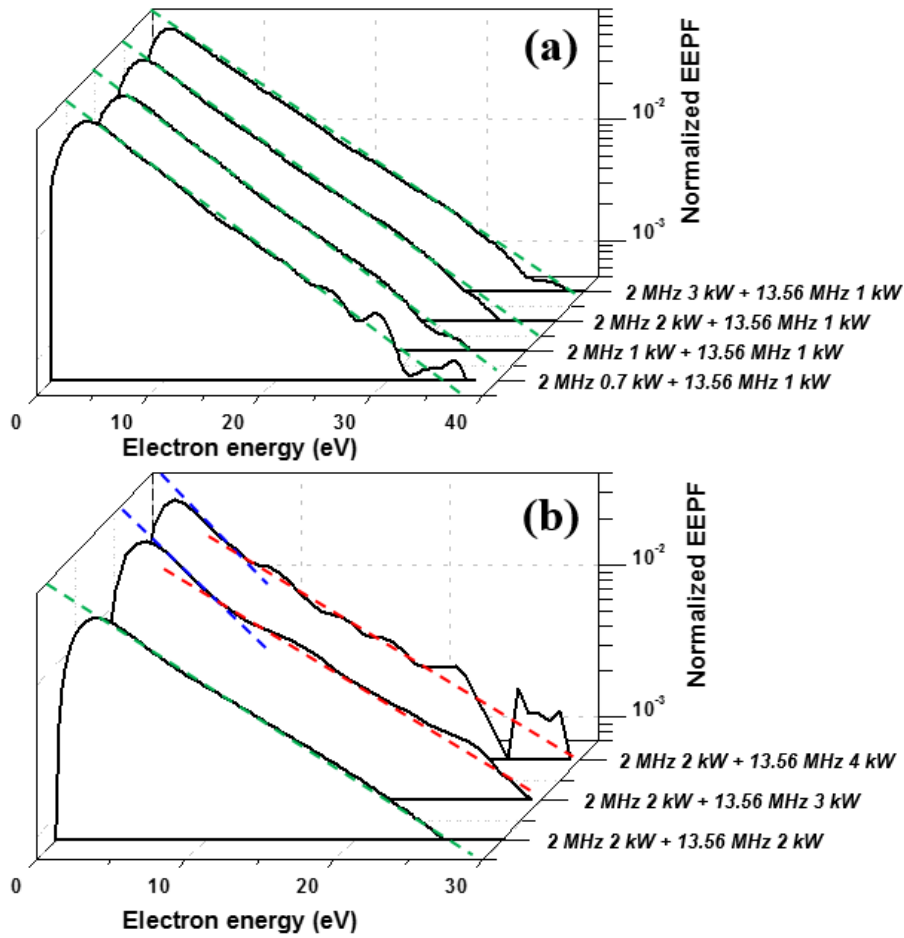


Figure 5.7 Normalized EEPF evolution with RF powers (a) at 2 MHz and (b) 13.56 MHz in the dual frequency antenna modes.

When RF power at 13.56 MHz $P_{13.56 \text{ MHz}}$, which can promote the bi-Maxwellization efficiently in the dual frequency antenna modes, is increased, EED is changed from Maxwellian ($P_{13.56 \text{ MHz}} = 2 \text{ kW}$) to bi-Maxwellian ($P_{13.56 \text{ MHz}} = 3$ and 4 kW). The characterization factors of the bi-Maxwellian EEDF are summarized in Table 5.1. During bi-Maxwellizing, $T_{e, \text{low}}$ is decreasing and T_e ,

$T_{e, high}$ and β are increasing, which proceeds toward making the EED with an apparent two-temperature structure.

TABLE 5.1 Calculated $T_{e, low}$, $T_{e, high}$, and β of EEDFs in the dual frequency antenna mode. (See Figure 5.7 (b))

<i>RF power</i> (13.56 MHz)	<i>2 kW</i>	<i>3 kW</i>	<i>4 kW</i>
$T_{e, low}$ (eV)	7.6	6.4	6.1
$T_{e, high}$ (eV)	7.6	15.0	15.0
β (%)	0	9	12

On the other hand, EED is unchanged in response to varying RF powers at 2 MHz, $P_{2\text{ MHz}}$, maintaining a Maxwellian EED shape. To clarify the driving frequency effect, the dependence of EEDF shape on electron density and ratio of $P_{13.56\text{ MHz}}$ and $P_{2\text{ MHz}}$ is depicted in Figure 5.8. Data of Figure 5.8 came from experiments relevant to Figure 5.7 and additional experiments.

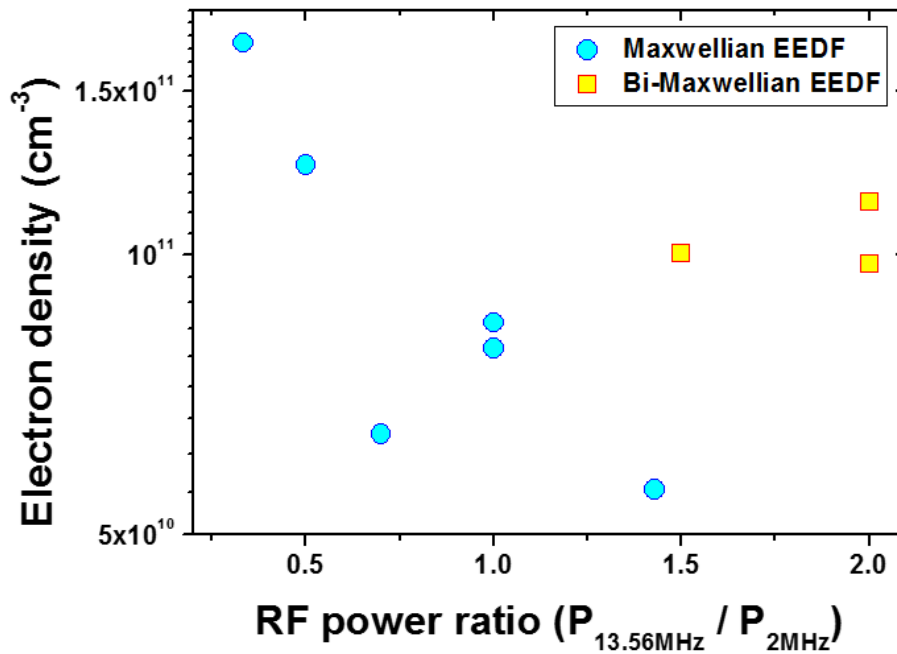


Figure 5.8 Dependence of EEDF shape on electron density and ratio of $P_{13.56\text{ MHz}}$ and $P_{2\text{ MHz}}$.

Since the RF power ratio of $P_{13.56\text{ MHz}}$ and $P_{2\text{ MHz}}$ in Figure 5.8 does not indicate the P_{abs} ratio, the quantitative analysis of the relation between EEDF shape and the power ratio is not significant. However, the experimental results have two important implications. (1) The EEDF shape can be controlled by the RF power ratio at the same pressure. (2) At the same electron density proportional to the power absorbed by plasma, the bi-Maxwellization occurs at a high $P_{13.56\text{ MHz}}/P_{2\text{ MHz}}$ ratio. This is attributed to the collisionless heating enhanced by applying a $P_{13.56\text{ MHz}}$ in dual frequency antenna mode, as predicted in Figure 5.5.

The bi-Maxwellization in the dual frequency antenna ICP depends on the pressure as well as electron density and $P_{13.56\text{ MHz}}/P_{2\text{ MHz}}$ ratio. The variation of

pressure can change the electron temperature, leading to shifts of v_{sto} , v_{en} , and v_{ee} in Figure 5.5. If it can be assumed that the degree of ionization in low-temperature plasmas is varied within the range of 0.5–5%, and the criterion of $v_{sto} > 3.6 (v_{en} + v_{ee})$ that corresponds to an onset of bi-Maxwellization in the experiments associated with Figure 5.5 and Figure 5.7 is merely applied to all conditions, the prediction of the critical electron density and pressure with regard to the bi-Maxwellization is possible. Figure 5.9 represents the critical electron density of the bi-Maxwellization in the dual frequency antenna ICP as a function of pressure.

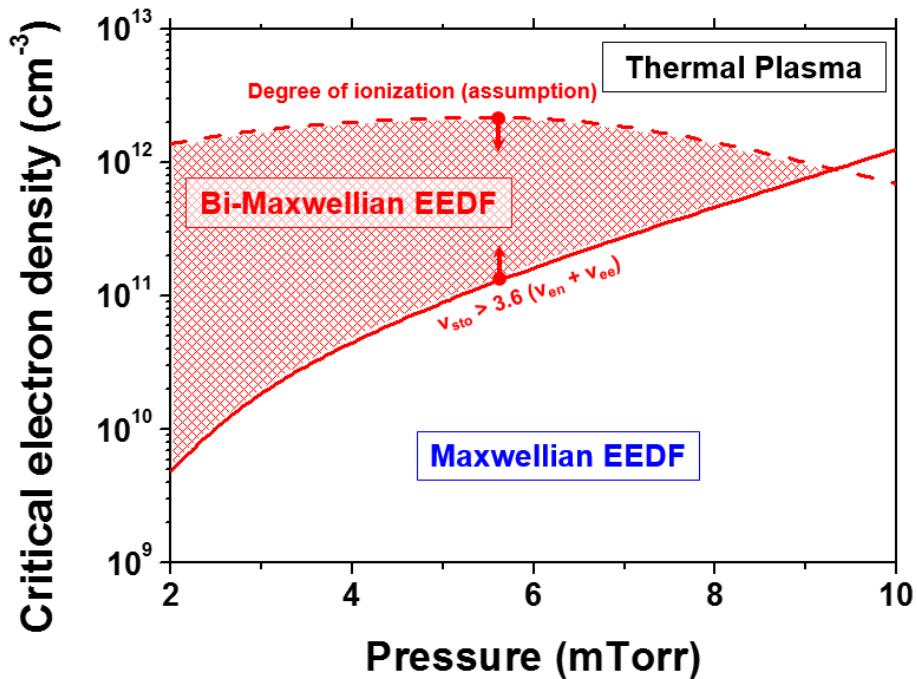


Figure 5.9 Critical electron density of the bi-Maxwellization in the dual frequency antenna ICP as a function of pressure.

Note that the bi-Maxwellization in the dual frequency antenna ICP is easily achieved at high electron density (or the RF power) and low pressure conditions.

5.3 H⁻ ion generation enhanced by bi-Maxwellization

For the evaluation of the volume-produced H⁻ ion and H atom (a precursor of the surface-produced H⁻ ion) production in the dual frequency antenna ICP, [25, 26, 138] the global model analysis using the EEDF data in Table 5.1 has been made. Figure 5.10 (a) and (b) show the comparisons of H atom and H⁻ ion densities obtained from the global model analysis with measured EEDF data in Table 5.1 and those with the assumption of Maxwellian EEDFs.

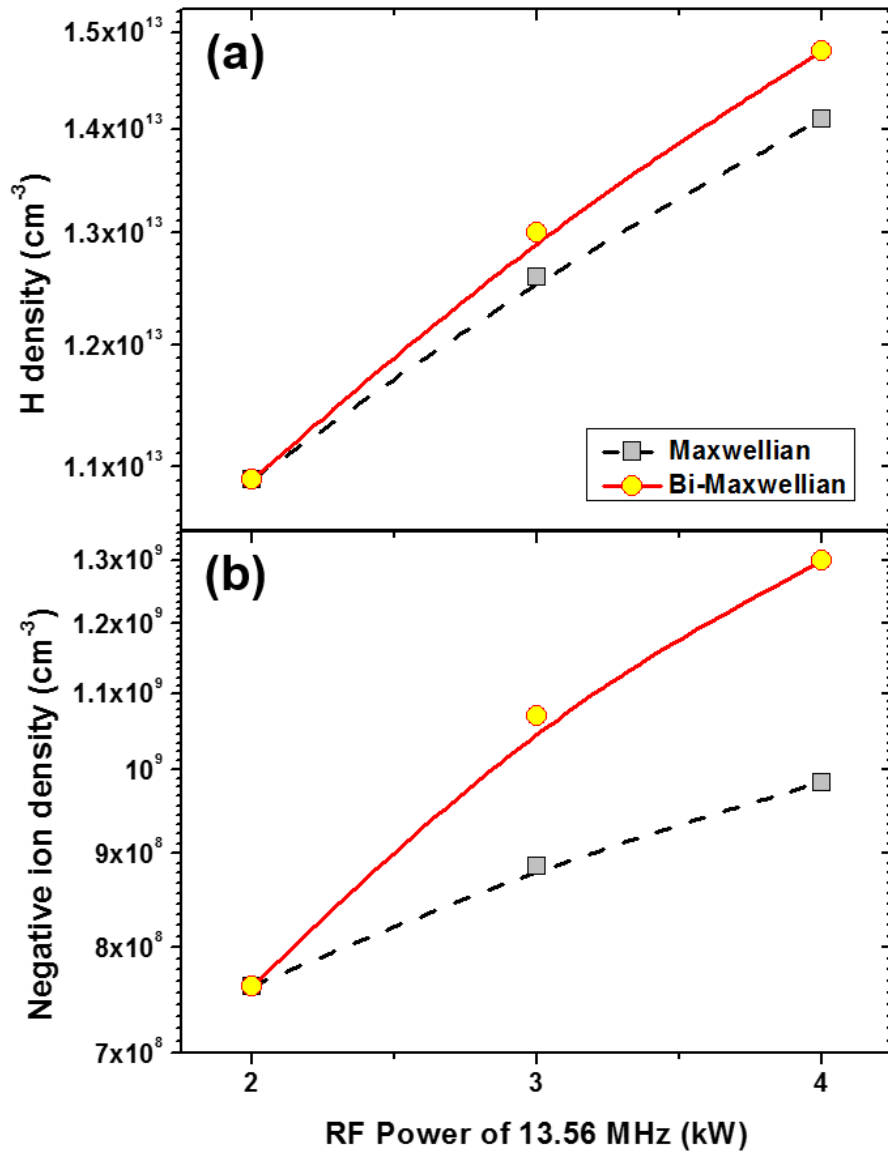


Figure 5.10 The dependence of (a) H atom density and (b) H⁻ ion density on $P_{13.56\text{ MHz}}$ in the dual frequency antenna ICP. The red solid lines represent model results obtained using measured EEDFs involving bi-Maxwellian EEDFs in Table 5.1, and the black dashed lines correspond to those with the assumption that EEDFs are Maxwellian.

Both H atom and H^- ion densities of bi-Maxwellian EED are higher than those of Maxwellian EED at more than 2 kW. (e.g., 5% and 32% higher for H atom and H^- ion densities, respectively, at $P_{13.56} = 4$ kW) At the same RF power, H atom and H^- ion density differences between the solid red and dashed black lines in Figure 5.10 mean contributions caused by the differences of electron energy distributions. As the EED becomes bi-Maxwellian with increasing $P_{13.56\text{ MHz}}$ in the dual frequency antenna mode, the differences in H atom and H^- ion densities increase. As discussed in Chapter 4, this increased H atom and H^- ion densities caused by the bi-Maxwellization is attributed to higher electron impact collision reaction rates of bi-Maxwellian electron energy distribution, compared to those of Maxwellian electron energy distribution. The presence of high energy electrons in bi-Maxwellian plasma leads to higher electron impact collision dissociation rate and then higher H atom density. Besides, it also promotes vibrational excitation rate to make higher vibrationally excited state density. Together with the abundant low energy electrons in bi-Maxwellian plasma, higher H^- ion density can be achieved.

Chapter 6. H⁻ ion generation enhanced by pulsing

Analogous to the magnetic filter, the source pulsing of the ion sources plays a role in separation of hot and cold electrons in time, resulting in the enhancement of the dissociative electron attachment. This source pulsing is called the temporal filter in the field of ion source. Several research groups studied the temporal filter, especially on the DC filament driven H⁻ ion sources, and found that H⁻ ion density increases, reaches a maximum, and then decreases in the after-glow (see Figure 6.1). [139–149]

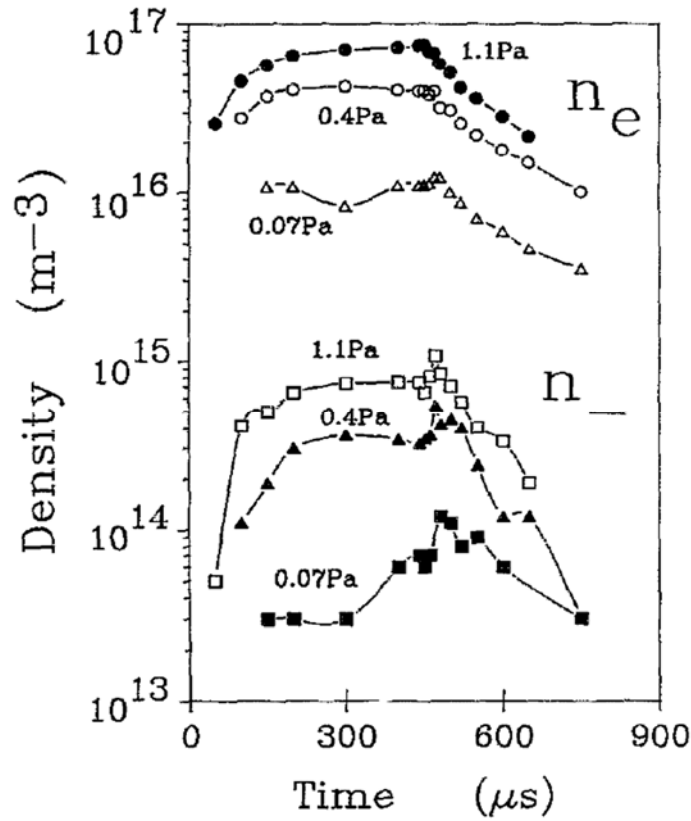


Figure 6.1 Electron and negative ion densities as a function of time, during the discharge and in the after-glow, for different source operating pressures, from [141].

The temporal filter has the merit of being simple such that there is no need to install an extra apparatus. In this chapter, in order to understand underlying physics of H^- ion generation enhanced by the temporal filter, the temporal behavior of H^- ion from an EEDF point of view will be investigated using both empirical and theoretical approaches.

central filter field strength is about 400 G. A cylindrical quartz tube in the discharge region has a diameter of 55 mm and a length of 240 mm. a copper (Cu) right hand polarized half-helical antenna is wound around the quartz tube generates a plasma. The discharge region is encircled by magnetic bucket made of permanent magnets to confine the plasma. RF power at 13.56 MHz is delivered to the antenna through RF matcher. A chamber, which has a diameter of 97 mm and a length of 176 mm, in the diffusion region was designed to accommodate laser photodetachment and Langmuir probe diagnostic systems.

For laser photodetachment technique, Nd:YAG laser of 532 nm in wavelength was injected into the center of the diffusion region. Its beam energy density was $89.9 \text{ mJ} / \text{cm}^2$ which is enough to photodetach almost all negative ions in the volume that the laser beam line passes through. (See Figure 2.22) For Langmuir probe diagnostics using boxcar sampling technique, a probe has a tungsten cylindrical tip with a diameter of 0.3 mm and a length of 9.5 mm. The time-resolved probe current with respect to bias voltage driven by programmed BOP was obtained by measuring the voltage difference across the sensing resistor, together with utilizing an oscilloscope triggered by the Q-switch signal of the laser. The triggering was double checked using a photodiode.

All experiments has been carried out at fixed RF power of 1 kW and operating pressure of 7 mTorr.

6.2 H⁻ ion generation in a pulsed ICP

6.2.1 Temporal behavior of H⁻ ions in a pulsed ICP

Figure 6.3 shows that the temporal variation of electron current and electronegativity with respect to RF power in the pulsed ICP, obtained using a time-resolved Langmuir probe and laser photodetachment technique. The pulse frequency and pulse duty cycle were 1 kHz and 50%, respectively. In the figure, numbers ①, ②, ③, and ④, indicate duration times of the initial active-glow (280 μs), the steady-state active-glow (220 μs), the initial after-glow (60 μs) and the late after-glow (440 μs), respectively, according to the variation of the electron current. It is interesting to note that the electronegativity (defined as the ratio of the H⁻ ion density to the electron density in this chapter for convenience's sake) drastically increases in the after-glow and then reaches to about 300% at 200 μs after RF power is turned off. During the period that electronegativity is over 100%, the dominant negatively charge species are H⁻ ions. It indicates that plasma is the positive ion – negative ion plasma. In the meantime, an increase in electronegativity does not necessarily mean an increase in H⁻ ions because the reduction of electron density in the after-glow can also result in the increase in electronegativity by definition. To distinguish variations of the electronegativity and H⁻ ion density, the electron density and negative ion density were measured as shown in Figure 6.4.

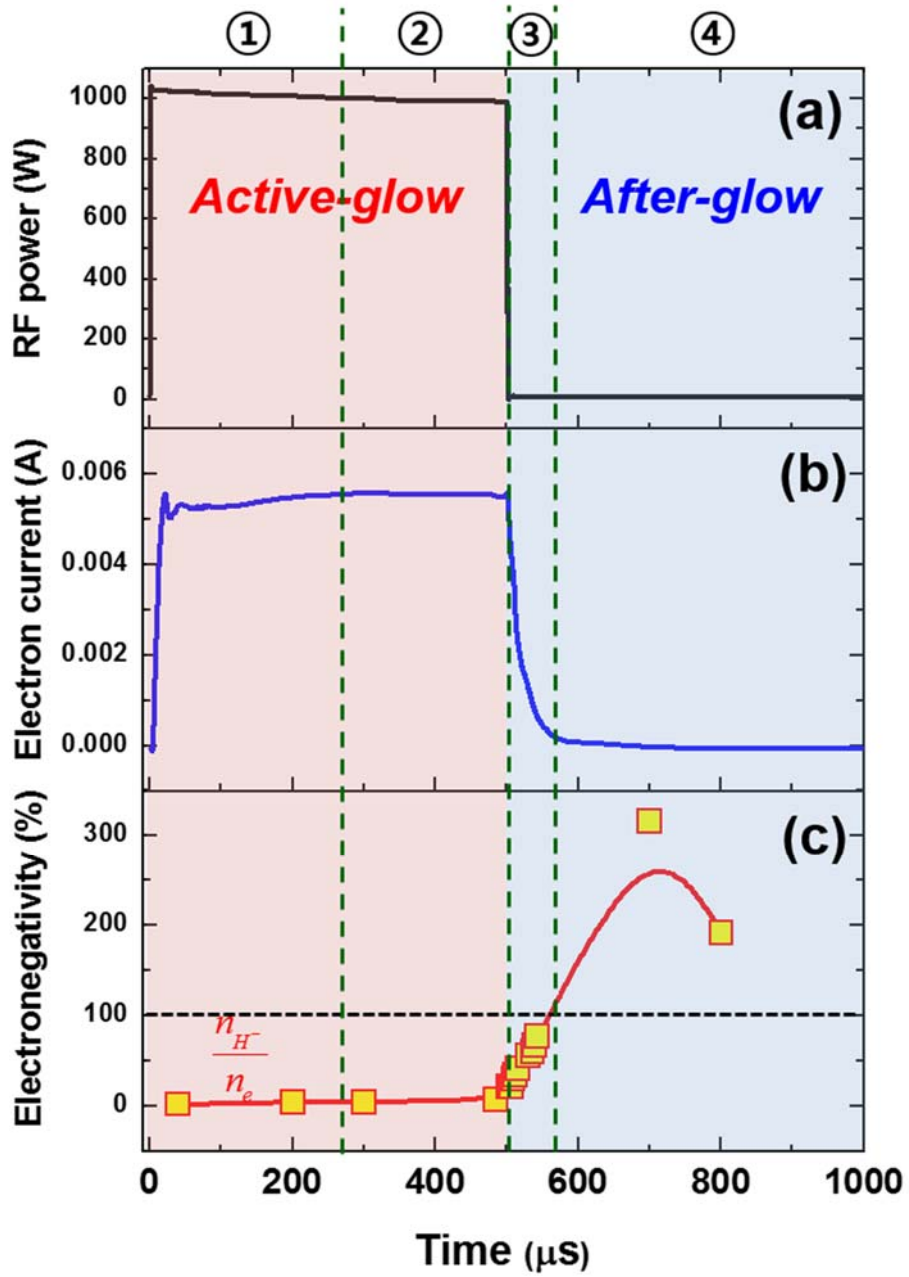


Figure 6.3 Temporal variation of (a) RF power, (b) electron current and (c) electronegativity at a pulse frequency of 1 kHz and a pulse duty cycle of 50%.

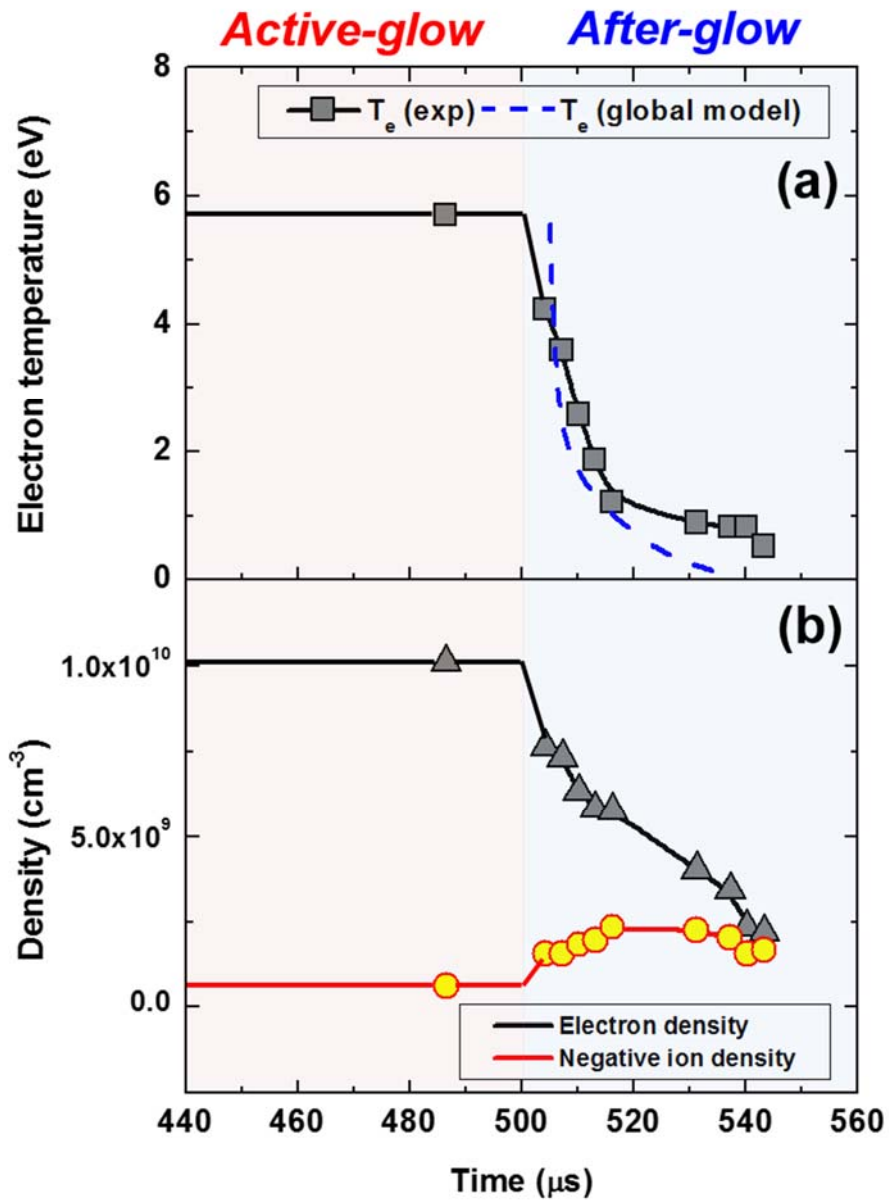


Figure 6.4 Temporal variation of (a) electron temperature (the black solid line: experimental data and the blue dashed line: global model results), (b) electron density and H^- ion density at a pulse frequency of 1 kHz and a pulse duty cycle of 50%.

Figure 6.4 presents the temporal variation of electron temperature, electron density and H^- ion density. For the time after 543 μs , experimental data were not measurable because $I - V$ characteristics of the Langmuir probe are almost out of recognition, due to low signals caused by the low plasma density. The electron temperature and electron density exponentially decreases, whereas H^- ion density increases and then decreases after RF power is turned off. Figure 6.5 is the magnified version of Figure 6.4(b).

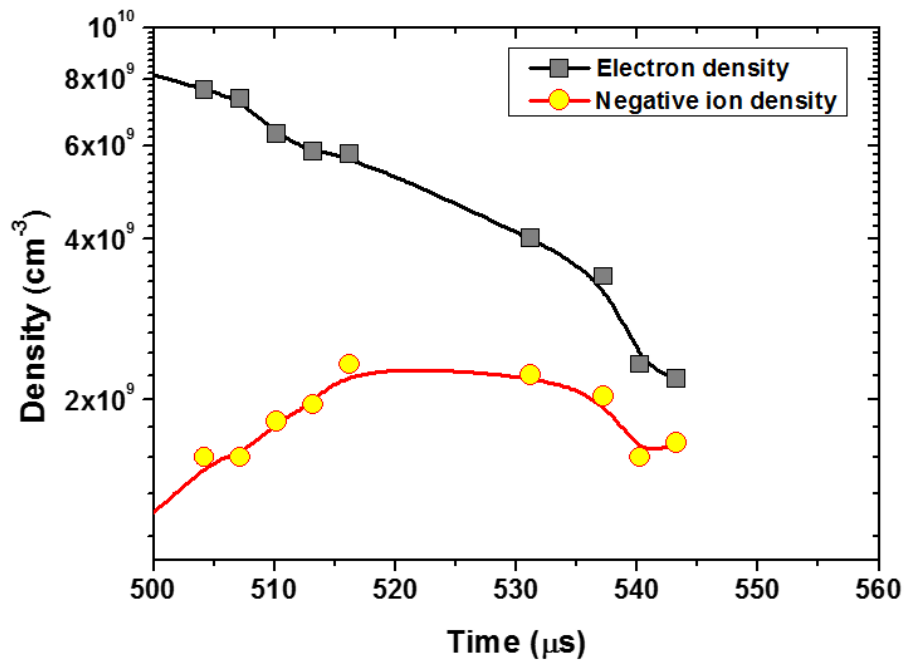


Figure 6.5 Magnified version of Figure 6.4(b) at a pulse frequency of 1 kHz and a pulse duty cycle of 50%.

As shown in Figure 6.5, the maximum H^- ion density is $2.5 \times 10^9 \text{ cm}^{-3}$ which

is about 30% of electron density and 17 times of H^- ion density in the active-glow. The corresponding time is 25 μs after RF power is turned off, and the estimate duration time that negative ion density is more than $1 \times 10^9 \text{ cm}^{-3}$ is about 60 μs . In the following subsection, temporal variation of the EEDF and $H_2(v)$ will be discussed in order to investigate the causes of the drastic increase in H^- ion density in the pulsed operation.

6.2.2 Temporal variation of EEDF and cooling mechanisms

For an in-depth discussion of the temporal EEDF variation, the $d(\text{EEDF})/dt$ – electron energy characteristic has been newly devised. (See Figure 6.6) Literally, the $d(\text{EEDF})/dt$ – electron energy characteristic can be obtained by the time differentiation of the EEDFs. The curve on the right side of Figure 6.6 shows the net electrons produced (+ sign) and lost (– sign) per unit time corresponding to energy.

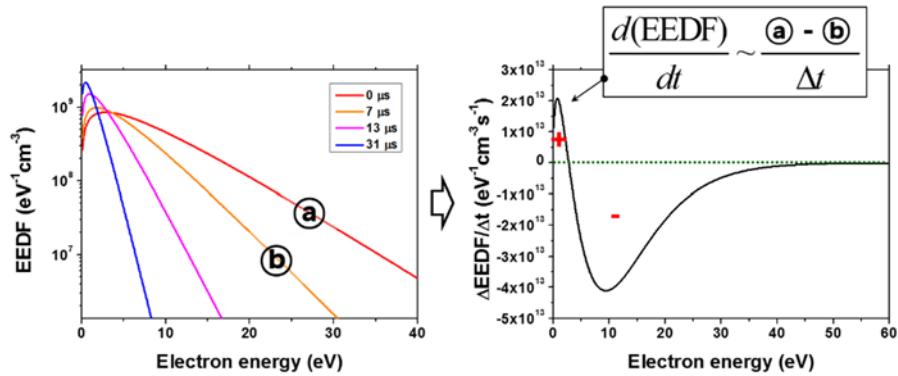


Figure 6.6 Schematic diagram for explanation of the newly devised $d(\text{EEDF})/dt$ – electron energy characteristic.

Electron densities after a certain time in the after-glow are commonly too low (i.e., low signal-to-noise ratio) to obtain clear EEDFs through the double differentiation and hence the $d(\text{EEDF})/dt$ – electron energy characteristics. In addition, the requirement of Equation (2.5.4) may not be satisfied due to large Z_{sh} caused by low electron densities, which can also yield serious distortions in the EEDFs and $d(\text{EEDF})/dt$ – electron energy characteristics. In this work, an alternative method to acquire $d(\text{EEDF})/dt$ – electron energy characteristics was used, assuming a Maxwellian EEDF. First, the electron densities and temperatures are directly attained from the I – V characteristics using a simple interpretation method outlined in Chapter 2. [48] Next, EEDFs are formulated using the Equation (2.3.3) together with the attained electron densities and temperatures. Lastly, time derivatives of the EEDFs or $d(\text{EEDF})/dt$ – electron energy characteristics are taken by performing the numerical differentiation.

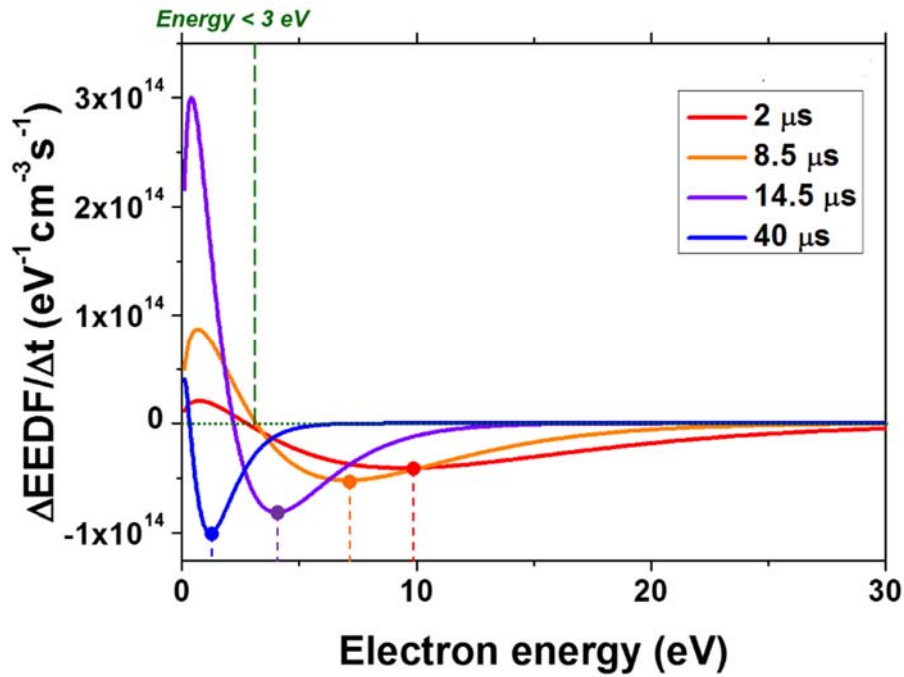


Figure 6.7 Experimental $d(\text{EEDF})/dt$ – electron energy characteristics at 2, 8.5, 14.5 and 40 μs after RF power is turned off.

Figure 6.7 shows that $d(\text{EEDF})/dt$ – electron energy characteristics, obtained using the alternative method, at 2, 8.5, 14.5 and 40 μs after RF power is turned off. For the temporal variation of $d(\text{EEDF})/dt$ – electron energy characteristic, two important features can be found. First, the most probable energy of the electron loss rate decreases as time goes by. It implies that the higher energy is, the higher loss rate of the corresponding electrons is. Second, the production rate of electrons at energies less than 3 eV (i.e., the production rate of low-energy electrons) increases till 14.5 μs and over. The rate may have its peak at a certain time between 14.5 and 40 μs . In the meanwhile, the density of low-

energy electrons continues to rise, in so far as the sign of the production rate is positive. Interestingly, despite a decrease in total electron density as shown in Figure 6.5, the low-energy electron density rather increases at early times in the after-glow. It is therefore speculated that the pulsed operation in the after-glow produces low-energy electrons as well as efficiently eliminates high-energy electrons. In this sense, *temporal filtered amplifier* rather than *temporal filter* may be a more appropriate term to describe the situation.

The two features discussed above indicate that the pulsed operation filters out high-energy electrons due to a larger loss of high-energy electrons than that of low-energy electrons and amplifies the production of the low-energy electrons due to certain favorable circumstances. The filtering and amplifying arise from the energy-dependent electron cooling. There are two electron cooling mechanisms responsible for the relaxation of the EEDF during the after-glow period, i.e., the diffusive cooling mechanism and the electron – neutral collisional cooling mechanism. [150, 151]

Most electrons are trapped in the plasma by the ambipolar potential barrier. Only high-energy electrons with a total energy larger than the potential difference between the plasma center and the wall can escape into a wall. The potential difference consists of the potential drop in the sheath and the potential drop between the plasma center and the sheath edge in the ambipolar plasma. The existence of the potential barrier gives rise to the depletion of the high-energy tail of the EEDF. As the sheath and the ambipolar potential collapse during the after-glow, the depletion of the EEDF proceeds from high-energy part to low-energy part with time. This is the diffusive cooling mechanism (see

Figure 6.8), and its cooling rate at a floating wall (or electron wall loss rate) is given by

$$\left. \frac{dn_e}{dt} \right|_{wall} = f_{EEDF}(\varepsilon) \Big|_{\varepsilon=\Phi_p(t)-\Phi_f(t)} \frac{d(\Phi_p(t)-\Phi_f(t))}{dt}, \quad (6.2.1)$$

where n_e is the electron density, f_{EEDF} is the electron energy distribution function, ε is the electron energy, Φ_p is the plasma potential, Φ_f is the floating potential, and t is time. [150]

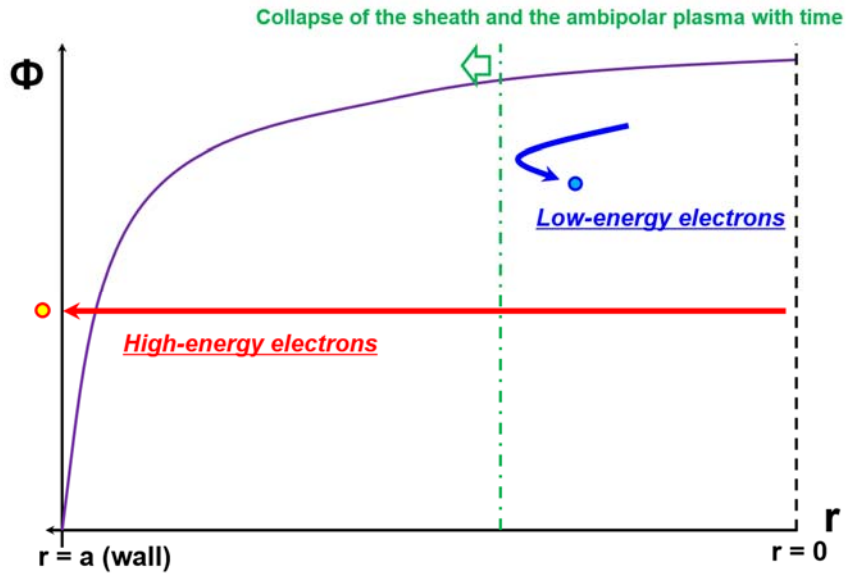


Figure 6.8 Schematic diagram of the diffusive cooling mechanism. Here, Φ is the potential, $r = 0$ is the radial position of the plasma center, and $r = a$ is the radial position of a wall in the cylindrical plasma system.

Since the potential drop in the sheath is larger than the potential drop in the

ambipolar plasma, the critical confinement energy associated with the electron wall loss (or the cutoff energy of the electron energy filtering) by the diffusive cooling is approximately equal to the potential drop in the sheath. Figure 6.9 shows the temporal evolution of the potential drop in the floating sheath (including the presheath) under the same experimental condition as in Figure 6.3 and Figure 6.4, except for a redefinition of time. For notational convenience, the initial time is redefined as the time when RF power is turned off (hereafter referred to as $t = 0$).

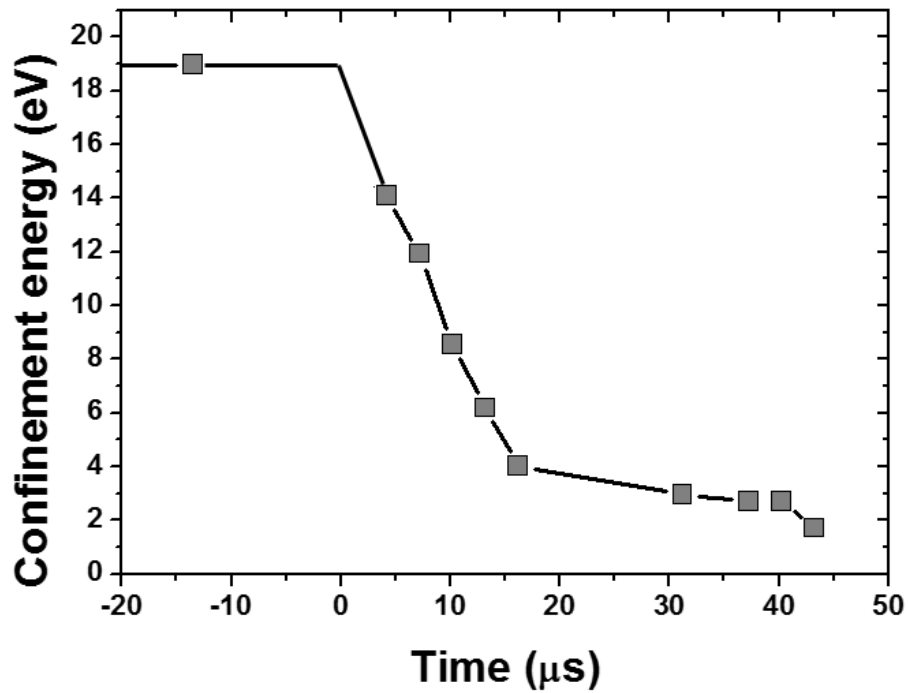


Figure 6.9 Temporal evolution of the critical confinement energy associated with the electron wall loss by the diffusive cooling at a pulse frequency of 1 kHz and a pulse duty cycle of 50%.

The critical confinement energy decreases with increasing time in the after-glow. This is ascribed to the sheath collapse due to the decrease in the electron temperature (see Figure 6.4(a)). Note that the floating sheath is proportional to the electron temperature (see Subsection 2.4.3). Figure 6.9 shows a fast decay for the first 15 μs and then a subsequent slow decay for times between 15 μs and 40 μs . In particular, the critical confinement energies for the slow decay time are maintained at values less than 3.5 eV, resulting in a proper energy filtering of electrons, i.e., the presence of low-energy (< 3.5 eV) electrons and the absence of high-energy (> 3.5 eV) electrons. Such a circumstance may promote the dissociative electron attachment and prevent the H^- ion destruction effectively. It is interesting to notice that the slow decay time nearly coincides with the period when the H^- ion density remains high in Figure 6.5. This supports the idea that the diffusive cooling contributes considerably to the H^- ion generation enhanced by the temporal electron energy filtering during the initial after-glow period.

In addition to the diffusive cooling, as mentioned previously, the electron energy relaxation caused by electron – neutral collisions, i.e., the electron – neutral collisional cooling, is another main electron cooling mechanism. The electron energy relaxation by the electron – neutral collisional cooling is a process in which electrons in higher energy part of the EEDF move to lower energy parts, without the electron loss, through the collisions. This leads to the increase of low-energy electrons, corresponding to the amplification of the low-energy electron production in the temporal filtered amplifier, and the reduction of high-energy electrons.

Figure 6.10 shows the temporal evolutions of the calculated electron – neutral elastic and inelastic collisional cooling rates besides that of the diffusive cooling rate under the same experimental condition as in Figure 6.9.

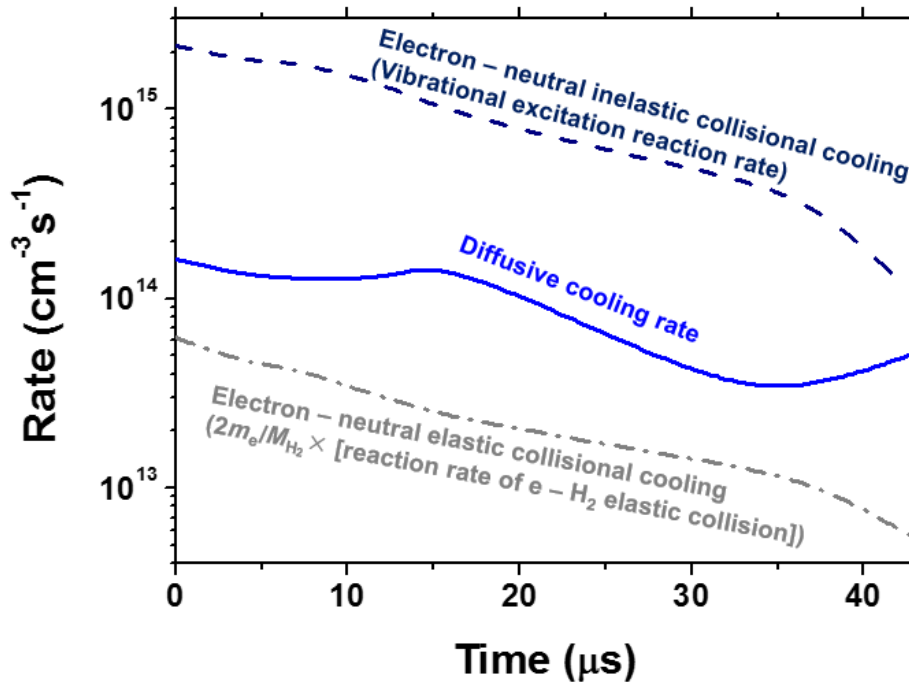


Figure 6.10 Temporal evolutions of the diffusive cooling rate (the blue solid line), the electron – neutral elastic collisional cooling rate (the grey dash-dotted line), and the reaction rate of the vibrational excitation (the $\nu = 1 \rightarrow \nu' = 2$ transition) as one of the major contributors to the electron – neutral inelastic collisional cooling (the navy dashed line) at a pulse frequency of 1 kHz and a pulse duty cycle of 50%.

For a comparison of the electron cooling rates, it is postulated that the elastic collision reaction rate multiplied by a factor of $2m_e/M_{H_2}$ that accounts for the

electron elastic loss (m_e : the electron mass and M_{H_2} : the H_2 molecule mass), the reaction rate of the vibrational excitation for the $\nu = 1 \rightarrow \nu' = 2$ transition (one of the major contributors to the electron – neutral inelastic collisional cooling), and the electron wall loss rate calculated using Equation (6.2.1) are regarded as the electron – neutral elastic collisional cooling rate, the electron – neutral inelastic collisional cooling rate, and the diffusive cooling rate, respectively. One should take note that the electron – neutral collisional cooling rates, unlike the diffusive cooling rate, represent the electron energy relaxation, not the electron loss. (Strictly speaking, the electron – neutral inelastic collisional cooling also involves the electron loss by the consumption of electrons in the electron attachment and recombination processes, but their reaction rates have only a small percentage of the total reaction rate. Thus, the electron loss by the electron – neutral collisional cooling can be neglected.) As seen in Figure 6.10, the electron – neutral inelastic collisional cooling rate is higher than the electron – neutral elastic collisional cooling rate and the diffusive cooling rate at 7 mTorr, which indicates that the electron – neutral inelastic collisional cooling dominates the electron cooling. However, this does not mean that the contribution of the diffusive cooling to the H^- ion generation enhanced by the electron energy filtering is smaller than that by the electron – neutral inelastic collisional cooling. Indeed, the electron energy filtering by the electron – neutral collisional cooling is not adequate for the H^- ion generation compared to that by the diffusive cooling. This can be explained as follows. The cutoff energy of the electron energy filtering by the electron – neutral collisional cooling can be determined by the threshold energies of the

electron – neutral collisions. Since the threshold energy of the electron – neutral elastic collisions does not exist and those of the major electron – neutral inelastic collisions, e.g., VE, IZ, and DIZ, (> 10 eV) in Figure 1.3 are much higher than the low energies favorable for the dissociative electron attachment, the electron energy filtering by the electron – neutral collisional cooling cannot effectively contribute to the H^- ion generation. For this reason, the electron energy filtering to support the H^- ion generation is due primarily to the diffusive cooling.

On the other hand, the main contribution of the electron – neutral inelastic collisional cooling to the H^- ion generation is the relaxation of high-energy electrons to produce low-energy electrons (or the amplification of the low-energy electron production). This yields an increase in the low-energy electrons relevant to (+) sign region in Figure 6.7. In consequence, it is concluded that the H^- ion generation in the pulsed ICPs is enhanced by electron energy filtering due to the diffusive cooling and by amplifying the low-energy electron production due to the electron – neutral inelastic collisional cooling.

6.2.3 Temporal variation of $H_2(v)$ molecule density

The relatively long lifetime of $H_2(v)$ molecules compared to the relaxation time of the EEDF allows sufficient highly vibrationally excited molecules produced in the active-glow to survive and thus to participate in the dissociative electron attachment during the initial after-glow period. [140, 141, 145] Together with the presence of the abundant low-energy electrons, this ensures

that high H^- ion density is maintained in the initial after-glow. In order to investigate temporal variation of $H_2(v)$ molecule density in the pulsed ICPs, the developed hydrogen plasma global model was utilized. Figure 6.11 presents the dependence of the calculated absolute $H_2(v)$ molecule density in the after-glow on the vibrational quantum number and time.

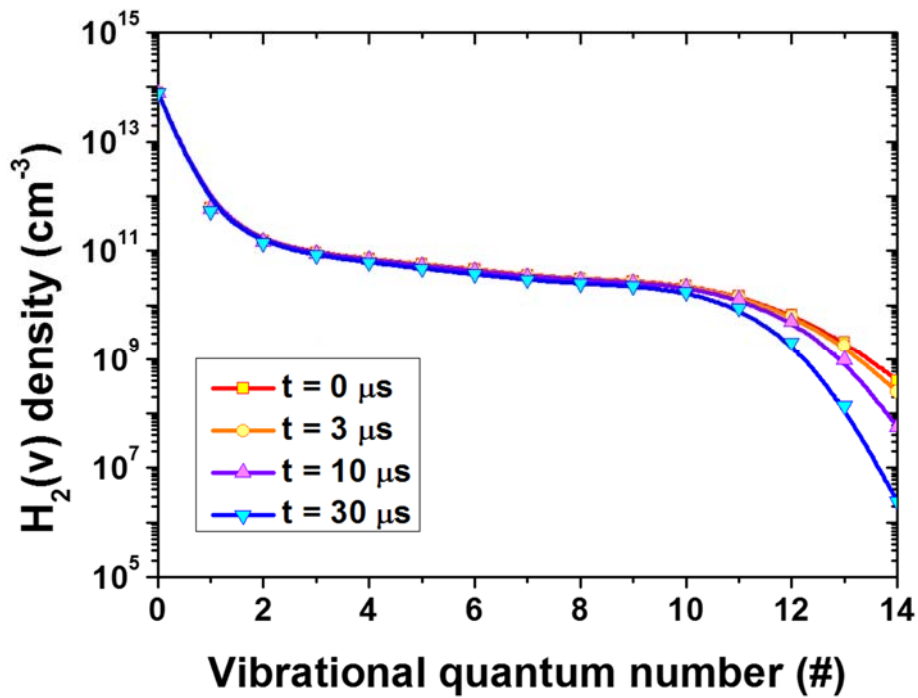


Figure 6.11 Dependence of the absolute $H_2(v)$ molecule density in the after-glow on the vibrational quantum number and time at a pulse frequency of 1 kHz and a pulse duty cycle of 50%.

The $H_2(v \leq 11)$ molecule densities hardly change with time, whereas the $H_2(v > 11)$ molecule densities do not. The $H_2(v > 11)$ molecule densities are

dramatically decreased with time, which may be ascribed to the consumption of them in the dissociative electron attachment. Note that only highly vibrationally excited states among $H_2(v)$ molecules are effective for the volume H^- ion generation (see Chapter 2). The result of Figure 6.11 specifically indicates that the effective highly vibrationally excited states are $v > 11$ states, and therefore the population of the $H_2(v)$ molecules at $v > 11$ states is crucial to determine the maximum H^- ion density in the initial after-glow.

The population of $H_2(v > 11)$ molecules may be strongly influenced by the characteristics of the active-glow (e.g., electron temperature), because plenty of high-energy electrons in the active-glow are required for the vibrational excitation of H_2 molecules via the H_2^* state to create highly vibrationally excited molecules. This is consistent with the fact that the electron temperature in the steady-state active-glow and the maximum H^- ion density in the initial after-glow of this study (6 eV and $2.5 \times 10^9 \text{ cm}^{-3}$ in Figure 6.5) are higher than those of Hopkins *et al.* [141] (< 3.3 eV and $\sim 1 \times 10^9 \text{ cm}^{-3}$ in Figure 6.1) at a similar pressure. The steady-state active-glow plasma with a higher electron temperature (or population of high-energy electrons) can provide more highly vibrationally excited molecules in the initial after-glow through the vibrational excitations. In this regard, the dual frequency antenna ICP can be employed to control the characteristics of the active-glow by the collisionless heating, i.e., the pulsed dual frequency antenna ICP. The feasibility and effectiveness of the pulsed dual frequency antenna ICP will be further explored in future work.

6.2.4 Major reactions for generation and destruction of H^- ions in the after-glow

The mutual neutralization, the dissociative electron attachment, and the electron detachment are the three most dominant reactions for the generation and the destruction of H^- ions in the after-glow. The temporal variation of reaction rates for three representative reactions with specific reactants (i.e., H_3^+ ion and H_2 ($v=8$) molecule) among these types of reactions are presented in Figure 6.12.

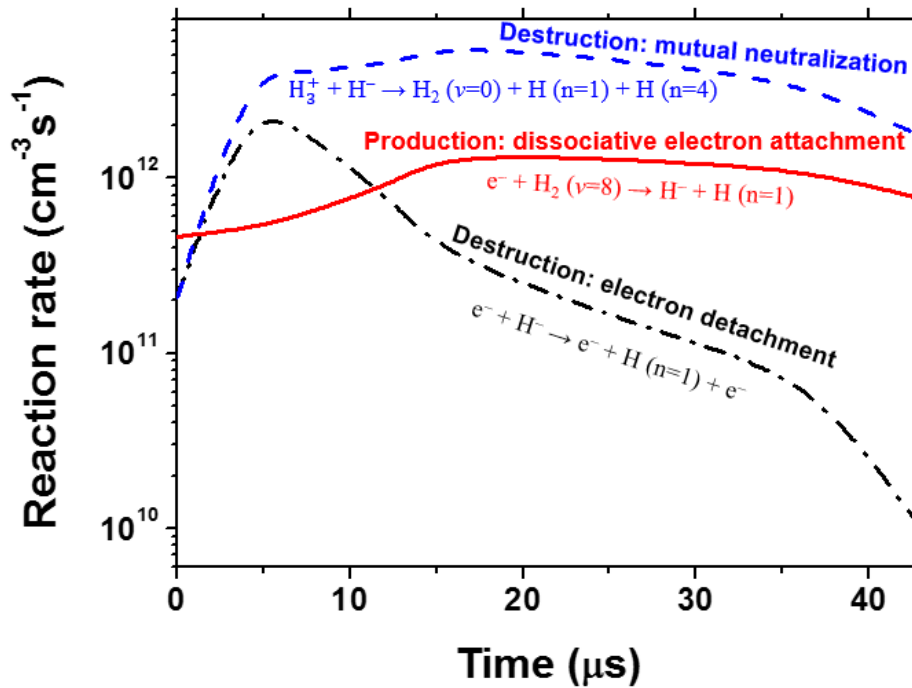


Figure 6.12 Calculated reaction rates of major reactions for the generation and the destruction of H^- ions in the after-glow as a function of time.

The ratio of H_3^+ ion density to total positive ion density and the ratio of $\text{H}_2(v=8)$ molecule density to $\text{H}_2(v=0)$ molecule density at $t > 0$ in the after-glow, which are necessary for the calculation of the reaction rates, were assumed to be equal to those at $t = 0$. It is interesting to note that the trends in the mutual neutralization and the dissociative electron attachment follow the tendency in the H^- ion density shown in Figure 6.5 that the H^- ion density increases with increasing time, reaches a peak value at 25 μs , and then begins decreasing with more increasing time. This provides evidence for a strong predominance of these two reactions in all reactions associated with the H^- ion generation and destruction during the after-glow period. On the other hand, the electron detachment (the second dominant reaction for the destruction of H^- ions) shows a different trend in its reaction rate. The electron detachment reaction rate is significantly reduced at $t > 5 \mu\text{s}$. This is attributed to decreases in the electron temperature and density presented in Figure 6.4.

6.3 The optimum pulse condition for obtaining the maximum average H^- ion density in repetitive pulsed ICPs

In the previous section, it was found that the active-glow and the after-glow are important because the densities of H_2 ($v > 11$) molecules and low-energy electrons (i.e., two precursor species of the volume-produced H^- ions) are dependent on the plasma characteristics of the active-glow and the after-glow, respectively. Accordingly, their plasma characteristics determine the maximum H^- ion density in the initial after-glow. In this section, the optimum pulse frequency, f_{opt-pf} and pulse duty cycle, $f_{opt-pdc}$, for obtaining the maximum average H^- ion density in repetitive pulsed ICPs will be investigated based on the findings described in the previous section and a postulate after-mentioned.

Figure 6.13 shows the electron current – time characteristics at different pulse frequencies and pulse duty cycles. Here again, $t = 0$ refers to the time when the RF power is turned on. The time when the RF power is turned off, $t_{power-off}$, is different depending on the pulse frequency and pulse duty cycle. The green vertical dashed lines in Figure 6.13(a) and (b) refer to the characteristic time when the electron current reaches a steady-state value at a pulse frequency of 1 kHz and a pulse duty cycle of 50%, i.e., $t_s = 280 \mu s$ (see Figure 6.3).

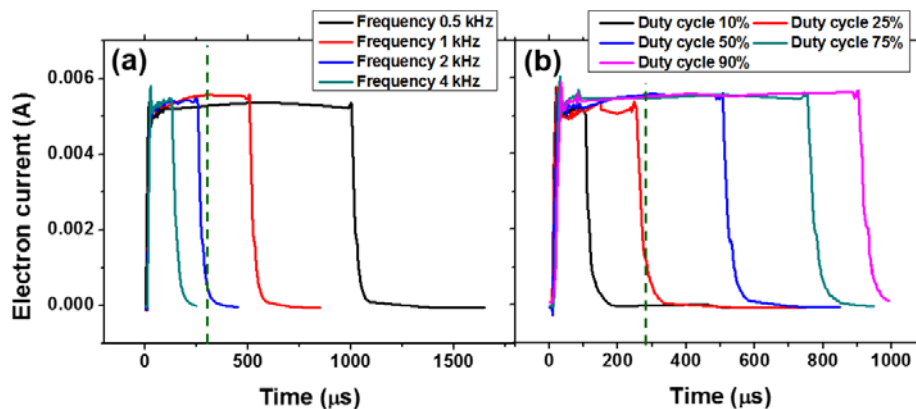


Figure 6.13 Electron current – time characteristics at different (a) pulse frequencies and (b) pulse duty cycles. Here, $t = 0$ is the time when the RF power is turned on. The green vertical dashed line refers to the characteristic time when the electron current reaches a steady-state value at a pulse frequency of 1 kHz and a pulse duty cycle of 50%.

Two notable features of the electron current – time characteristics are as follows:

- (1) The electron current cannot attain a steady-state value when $t < t_s = 280 \mu\text{s}$ (the green vertical dashed lines), regardless of the pulse frequency or the pulse duty cycle.
- (2) After the RF power is turned off, the electron currents decay at almost the same rate. It is a noteworthy fact that the rise and decay times of the electron current is not a function of the pulse frequency or the pulse duty cycle. Here, the rise time is the time during which a species density varies[†] from its minimum value at $t = 0$ to a steady-state value and the decay time is the time

[†] The reason why *varies* instead of *increases* or *decreases* was used is to include the particular rise/decay time for which a species density (e.g., the H^- ion density in the after-glow) increases from its initial value to an extent and then decreases to its final value with the conventional definition of the rise/decay time.

during which a species density varies from a steady-state value at $t = t_{\text{power-off}}$ to its minimum value.

If it can be postulated that the rise/decay times of H_2 ($\nu > 11$) molecule density and H^- ion density as well as that of the electron current are irrelevant to the pulse frequency or the pulse duty cycle, one can figure out $f_{\text{opt-pf}}$ and $f_{\text{opt-pdc}}$ for obtaining the maximum average H^- ion density in repetitive pulsed ICPs. For the volume production of H^- ions in the pulsed ICPs, the rise time of H_2 ($\nu > 11$) molecule density, $\Delta t_{r, \text{H}_2}$, and the decay time of low-energy electron population, $\Delta t_{d, e}$, may be important factors determining $f_{\text{opt-pf}}$ and $f_{\text{opt-pdc}}$ because the H_2 ($\nu > 11$) molecules and low-energy electrons are precursor species of the volume-produced H^- ions and their densities increase only during $\Delta t_{r, \text{H}_2}$ and $\Delta t_{d, e}$. When the duration time of the active-glow phase (or power-on period, $\Delta t_{\text{power-on}}$) is shorter than $\Delta t_{r, \text{H}_2}$, the H_2 ($\nu > 11$) molecule density cannot attain a steady-state value. Similarly, when the duration time of the after-glow phase (or power-off period, $\Delta t_{\text{power-off}}$) is shorter than $\Delta t_{d, e}$, a sufficient low-energy electron population required for the volume production of H^- ions in the after-glow cannot be obtained. On the contrary, when $\Delta t_{\text{power-on}} > \Delta t_{r, \text{H}_2}$ or $\Delta t_{\text{power-off}} > \Delta t_{d, e}$, an unnecessary extra time (i.e., $\Delta t_{\text{power-on}} - \Delta t_{r, \text{H}_2}$ or $\Delta t_{\text{power-off}} - \Delta t_{d, e}$) for which both H^- ions and their precursors are not further produced is given. Consequently, the optimum characteristic $\Delta t_{\text{power-on}}$ and $\Delta t_{\text{power-off}}$ that maximize the densities of H^- ions and their precursors equal to $\Delta t_{r, \text{H}_2}$ and $\Delta t_{d, e}$, respectively. The corresponding optimum pulse condition is characterized by the pulse frequency of $(\Delta t_{r, \text{H}_2} + \Delta t_{d, e})^{-1}$ and the pulse duty cycle of $\Delta t_{r, \text{H}_2} / (\Delta t_{r, \text{H}_2} + \Delta t_{d, e})$

obtained from their definitions (see subsection 2.4.3.). f_{opt-pf} and $f_{opt-pdc}$ under the experimental condition (RF power: 1 kW and operating pressure: 7 mTorr) were calculated assuming that $\Delta t_{r, H_2} \sim \Delta t_{i-active}$ (the duration time of the initial active-glow) and $\Delta t_{d, e} \sim \Delta t_{i-after}$ (the duration time of the initial after-glow) as follows: $f_{opt-pf} = 3$ kHz and $f_{opt-pdc} = 82\%$.

The characteristic $\Delta t_{r, H_2}$ and $\Delta t_{d, e}$ are typically determined by RF power, pressure, and chamber size, etc. Future work will examine the postulate by comparing values of $\Delta t_{r, H_2}$ and $\Delta t_{d, e}$ (or $\Delta t_{i-active}$ and $\Delta t_{i-after}$) obtained at different RF powers and pressures.

Chapter 7. Conclusion

The ultimate goal of RF driven H^- ion source driver developments is to enhance the generation of H^- ions and their precursors with a high RF efficiency for achieving larger extracted H^- ion beam current with less RF power. An efficient way of accomplishing the goal is to study the underlying physics of low-pressure hydrogen discharges and ICPs, which ensures understanding the relationship between chemical kinetics of hydrogen plasmas and engineering design parameters of the ion sources. In this work, characteristics of low-pressure hydrogen plasmas involved in the H^- ion production and properties of ICPs associated with the RF efficiency are investigated using theoretical and empirical approaches.

Since electron impact collision reactions dominate the collisions in low-pressure hydrogen plasmas, the EEDF is a key parameter required to characterize the generation and destruction of H^- ions and their precursors that are dependent on the power absorption and the electron heating/cooling of ICPs. The H^- ion production was found to be sensitive to changes in the EEDF shape (i.e., the bi-Maxwellization or the Maxwellization). A global model capable of calculating the electron impact collision reaction rate constants and sheath parameters under the Maxwellian and bi-Maxwellian EEDFs was developed to investigate the densities of H^- ions and other species that contribute to H^- ion generation and destruction.

In the bi-Maxwellian plasmas, $T_{e, high}$ is higher whereas $T_{e, low}$ is much lower

than T_e^{Max} in the case of Maxwellian plasmas. This is due to the selectivity of the collisionless heating that effectively heats high-energy electrons surpassing a critical energy threshold, and the ambipolar potential barrier in which only low-energy electrons are trapped outside the skin layer where the collisionless heating occurs. This bi-Maxwellization is reflected in the global model by using experimental values for $T_{e, high}$ and β as the model input parameters. High-energy electrons with higher ionization reaction rates lower the temperature of another electron group for compensation of the generation reaction rates balancing the loss rates, resulting in the presence of low-energy electrons with $T_{e, low}$. It is interesting to note that the bi-Maxwellian plasma causes two important changes in the densities of H^- ions and related species as compared to the Maxwellian plasma: (1) High-energy electrons with higher electron impact collision reaction rate constants significantly contribute to the vibrational excitation, dissociation and ionization of the hydrogen molecules. (2) Low-energy electrons lowering the effective electron temperature reduce the ion energy loss at the walls, and consequently lead to a higher electron density for keeping wall loss power density to satisfy the energy balance. The higher electron impact collision reaction rate constants and the higher electron density increase the reaction rates, which results in higher densities of H atoms, H_2 ($v = 5-14$) molecules and positive ions. H_2 ($v = 5-14$) molecules and positive ions are reactants in the major volume generation and destruction processes of H^- ions (i.e., dissociative electron attachment and mutual neutralization), respectively. The results obtained from the global model analysis, including the competition between the increased generation and destruction processes of H^-

ions by changing the EEDF, indicate that an increase in H^- ion density occurs. This is due to the fact that the dissociative electron attachments are much promoted in the presence of abundant low-energy electrons and H_2 ($v = 5-14$) molecules. It is concluded that the bi-Maxwellian EEDF in the low-pressure regime is more favorable to create H^- ions, compared to Maxwellian EEDF.

The dual frequency antenna ICP as the RF driven H^- ion source driver was proposed in order to control the EEDF shape. It has two antennas feeding RF powers at two different frequencies, i.e., 2 and 13.56 MHz. In comparison with the conventional single frequency antenna ICPs, the dual frequency antenna ICP shows two distinctive features: (1) an increase in the power transfer efficiency P_{abs}/P_{total} and (2) the bi-Maxwellization of the EEDF enhanced by the collisionless heating.

It was found that the electron density of the dual frequency antenna mode is higher than that of the single frequency antenna mode, regardless of driving frequency, at the same total RF power P_{total} . Because plasma parameters (e.g., electron density) associated with phenomena occurring in the plasmas are relevant to only power absorbed by the plasma P_{abs} , not P_{total} , this phenomena is attributed to the difference in P_{abs} of the single and dual antenna modes. In the dual antenna mode, the presence of power absorption within a skin layer near one antenna causes an increase in electron density within a skin layer near the other, and vice versa. This effect leads to an improved antenna – plasma coupling and then a high P_{abs} (or P_{abs}/P_{total}) by each antenna compared to those by a sole antenna in the single antenna mode at the same P_{total} . The increase in total P_{abs} by both of antennas in the dual antenna mode yields a higher electron

density. It suggests that the dual frequency antenna ICP compared to the conventional ICPs has a high RF efficiency, which thereby encourages the development of the efficient RF driven H^- ion source drivers.

At low pressures, the dual frequency antenna ICP can give rise to a change in the EEDF from a Maxwellian to a bi-Maxwellian shape, i.e., the bi-Maxwellization. When the electron density increases, both the collisionless selective electron heating of high-energy electrons and the electron – electron collisions are promoted. The collisionless heating and the electron – electron collisions are responsible for the bi-Maxwellization and the Maxwellization, respectively, and their competition determines the EEDF shape. Since the collisionless heating, unlike the collisional heating, is frequency-dependent, plasmas with different $P_{13.56\text{ MHz}}/P_{2\text{ MHz}}$ at the same P_{abs} differ in their collisionless power absorption and accordingly the extent of the bi-Maxwellization. Experiments and qualitative analyses on the characteristic collision frequencies reveal that the bi-Maxwellization occurs at only high $P_{13.56\text{ MHz}}/P_{2\text{ MHz}}$ values and it becomes significant with increasing the $P_{13.56\text{ MHz}}/P_{2\text{ MHz}}$ value. In other words, under these experimental conditions, $\omega = 13.56\text{ MHz}$ is more effective than $\omega = 2\text{ MHz}$ for the bi-Maxwellization enhanced by the collisionless heating. This provides compelling evidence that the EEDF shape can be controlled by varying the RF power ratio in the dual frequency antenna ICP at the same pressure.

Furthermore, enhancement of the volume-produced H^- ion and H atom (a precursor species of the surface-produced H^- ions) production due to the bi-Maxwellization in the dual frequency antenna ICP was evaluated using the

developed global model. As a result of the bi-Maxwellization, the H atom and H^- ion densities increase by a few to many tens of percent. Besides, it appears that the bi-Maxwellization also increases vibrational excitation to produce $H_2(v)$ molecules. In consequence, the dual frequency antenna ICP is a promising candidate for the efficient RF driven H^- ion source drivers with respect to the generation of H^- ions and their precursors as well as the RF efficiency.

In addition, the source pulsing for the enhancement of the dissociative electron attachment, called the temporal filter, was investigated by introducing the newly devised $d(EEDF)/dt$ – electron energy characteristic. The experimental result shows that H^- ion density increases up to $2.5 \times 10^9 \text{ cm}^{-3}$ in the initial after-glow, which is about 17 times of H^- ion density in the active-glow. This is ascribed to the electron cooling (i.e., the diffusive cooling and the electron – neutral inelastic collisional cooling) in the initial after-glow and the long lifetime of $H_2(v)$ molecules.

The electron cooling in the initial after-glow contributes to the enhancement of the volume-produced H^- ion generation by providing low-energy ($< 3 \text{ eV}$) electrons and by eliminating high-energy electrons. The diffusive cooling due to the sheath and ambipolar potential barrier play roles in confining low-energy electrons and filtering out high-energy electrons. On the other hand, the electron – neutral inelastic collisional cooling leads to the collisional relaxation of high-energy electrons, producing low-energy electrons efficiently. Because the source pulsing or temporal filter does not only filter out high-energy electrons but also amplifies the production of the low-energy electrons, a new alternative

term *temporal filtered amplifier* instead of *temporal filter* was suggested to describe electron cooling in the initial after-glow more appropriately.

The relatively long lifetime of $H_2(v)$ molecules compared to the relaxation time of the EEDF also gives aid to the enhancement of the volume-produced H^- ion generation. It allows sufficient $H_2(v)$ molecules produced in the steady-state active-glow to survive and hence to participate in the dissociative electron attachment during the initial after-glow period. By using the developed global model, it was found that the population of the $H_2(v)$ molecules, especially $H_2(v > 11)$ molecules, is important to determine the maximum H^- ion density in the initial after-glow.

Since the densities of $H_2(v > 11)$ molecules and low-energy ($< 3\text{eV}$) electrons depend on the characteristic times of the active-glow and the after-glow, respectively, the average H^- ion density in the initial after-glow of the repetitive pulsed ICPs can be controlled by varying the pulse condition (i.e., pulse frequency and pulse duty cycle). It was identified that the optimum characteristic power-on period and power-off period for maximizing the densities of H^- ions and their precursors equal to $\Delta t_{r, H_2}$ and $\Delta t_{d, e}$, respectively. Accordingly, the optimum pulse frequency is $(\Delta t_{r, H_2} + \Delta t_{d, e})^{-1}$ and the optimum pulse duty cycle is $\Delta t_{r, H_2} / (\Delta t_{r, H_2} + \Delta t_{d, e})$.

This basic study may contribute to the development of more efficient RF driven H^- ion source drivers for widespread industrial and fusion applications, and it can be applicable to plasma processes and ion source technologies using other X_2 gas (e.g., N_2 , O_2 , etc.).

Appendix A. Floating harmonics method for determination of EEDF

A new floating harmonics method has been developed to determine the EED shape in the non-Maxwellian plasmas. The slope and curvature of the EEPF at the floating potential can be obtained by measuring amplitude ratios among the first three sideband harmonics of the probe electron current. Together with the generalized EEPF formula, the EEPF shapes of the non-Maxwellian plasmas are able to be determined from the slope and curvature.

Principles of measurement

To determine the EEPF shapes in the non-Maxwellian plasmas, a formula was introduced to express the EEPF including the non-equilibrium EEPF. EEPF in a semi-logarithmic scale shows the quick visualization of a dissimilarity of the measured EEPF from a Maxwellian EEPF that is a straight line in the illustration. [35] When the velocity space is isotropic, the arbitrary normalized EEPF can be fitted as the generalized formula [36]

$$f_{EEPF}(\varepsilon) = c_1 \exp(-c_2 \varepsilon^x). \quad (\text{A.1})$$

Here, x is a parameter relevant to the EEPF shape, $c_1 \equiv x[2\Gamma(\xi_2)/3T_{e,\text{eff}}]^{3/2} / [\Gamma(\xi_1)]^{5/2}$ and $c_2 \equiv [2\Gamma(\xi_2)/3T_{e,\text{eff}}\Gamma(\xi_1)]^x$ are functions of x and $T_{e,\text{eff}}$, where $\xi_1 \equiv 3/2x$, $\xi_2 \equiv 5/2x$, Γ is the gamma function and $T_{e,\text{eff}}$ is the

effective electron temperature in eV. In Equation (A.1), $x = 1$ means the Maxwellian EEPF. Furthermore, the bi-Maxwellian-like and Druyvesteyn-like EEPFs can be expressed as $x < 1$ and $x > 1$, respectively.

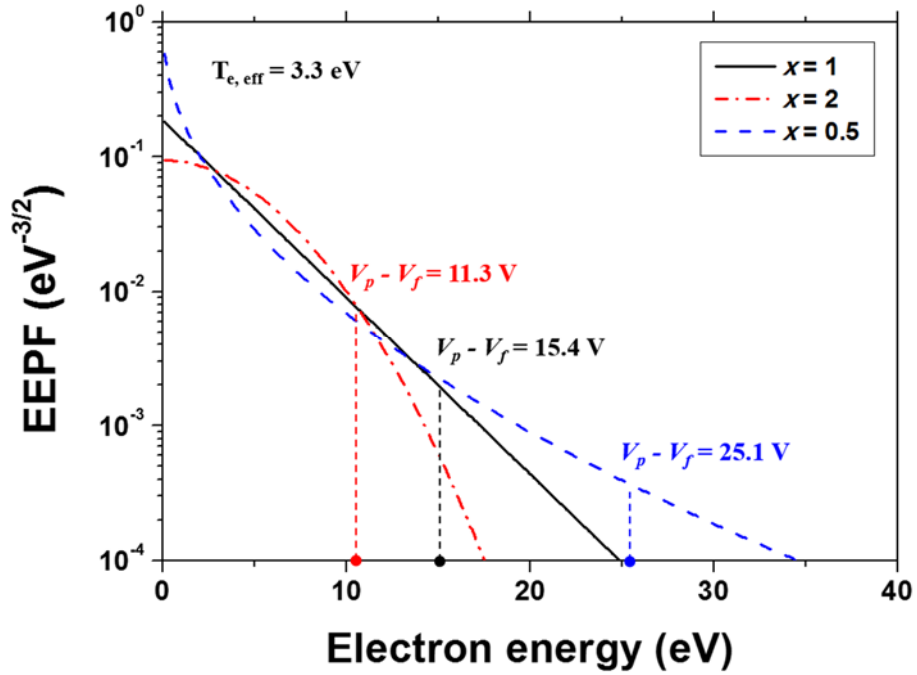


Figure A.1.1 The Maxwellian and non-Maxwellian EEPFs in a semi-logarithmic scale. (from Equation (A.1) for $T_{e, \text{eff}} = 3.3$ eV and $x = 0.5, 1, 2$) $x = 1$, $x < 1$ and $x > 1$ correspond to the Maxwellian, bi-Maxwellian-like and Druyvesteyn-like EEPFs, respectively.

As depicted in Figure A.1, $x = 1$, $x < 1$ and $x > 1$ correspond to the straight line, concave curve and convex curve, respectively. The first derivative of the EEPF curve in a semi-logarithmic scale representing the slope of the curve is given

by

$$\frac{d \ln[f_{EEPF}(\varepsilon)]}{d\varepsilon} = -c_2 x \varepsilon^{x-1}. \quad (\text{A.2})$$

In addition, the second derivative of the curve representing the curvature can be expressed as

$$\frac{d^2 \ln[f_{EEPF}(\varepsilon)]}{d\varepsilon^2} = -c_2 x(x-1) \varepsilon^{x-2}. \quad (\text{A.3})$$

The normalized EEPF can be also obtained from the I-V characteristics by the Druyvesteyn method: [152]

$$f_{EEPF}(V) = \frac{2m_e}{n_o e^2 A} \left(\frac{2e}{m_e}\right)^{1/2} \frac{d^2 i_e}{dV^2}, \quad (\text{A.4})$$

where m_e is the electron mass, n_o is the plasma density, e is the elementary charge, A is the area of the probe tip, i_e is the probe electron current, and V is the probe voltage. Here, $\varepsilon = V_p - V$, where V_p denotes the plasma potential.

In a similar way, the first and second derivatives of the EEPF curve in a semi-logarithmic scale then yield

$$\frac{d \ln[f_{EEPF}(V)]}{dV} = \frac{1}{f_{EEPF}(V)} \frac{d[f_{EEPF}(V)]}{dV} = \frac{d^3 i_e}{dV^3} / \frac{d^2 i_e}{dV^2} \quad (\text{A.5})$$

and

$$\frac{d^2 \ln[f_{EEPF}(V)]}{dV^2} = \frac{d^4 i_e}{dV^4} / \frac{d^2 i_e}{dV^2} - \left(\frac{d^3 i_e}{dV^3} / \frac{d^2 i_e}{dV^2}\right)^2, \quad (\text{A.6})$$

respectively. In the floating probe measurement using the sideband method, i_e collected by applying a small dual frequency superimposed sinusoidal voltage, $V_1 \sin \omega_1 t + V_2 \sin \omega_2 t$, can be found by the Taylor expansion if $V \gg V_1 \sin \omega_1 t + V_2 \sin \omega_2 t$: [153]

$$\begin{aligned}
i_e(V + V_1 \sin \omega_1 t + V_2 \sin \omega_2 t) &= i_e(V) + (V_1 \sin \omega_1 t + V_2 \sin \omega_2 t) \frac{di_e}{dV} \\
&+ \frac{(V_1 \sin \omega_1 t + V_2 \sin \omega_2 t)^2}{2!} \frac{d^2 i_e}{dV^2} \\
&+ \frac{(V_1 \sin \omega_1 t + V_2 \sin \omega_2 t)^3}{3!} \frac{d^3 i_e}{dV^3} + \dots,
\end{aligned} \tag{A.7}$$

where V_1 and V_2 are the amplitudes of the sinusoidal voltages, ω_1 and ω_2 are the frequencies of the sinusoidal voltages in the sideband method, and t is time. Products and powers of trigonometric functions on the first three sideband harmonics in Equation (A.7) can be rewritten in terms of trigonometric functions with combined arguments:

$$\begin{aligned}
i_e &= \dots + i_{e, \omega_1 \pm \omega_2} + i_{e, \omega_1 \pm 2\omega_2} + i_{e, \omega_1 \pm 3\omega_2} + \dots \\
&= \dots \mp \left(\frac{V_1 V_2}{2} \frac{d^2 i_e}{dV^2} + \frac{V_1 V_2}{16} (V_1^2 + V_2^2) \frac{d^4 i_e}{dV^4} + \dots \right) \times \cos[(\omega_1 \pm \omega_2)t] \\
&\quad - \left(\frac{V_1 V_2^2}{8} \frac{d^3 i_e}{dV^3} + \frac{V_1 V_2^2}{192} (3V_1^2 + 2V_2^2) \frac{d^5 i_e}{dV^5} + \dots \right) \times \sin[(\omega_1 \pm 2\omega_2)t] \\
&\quad \pm \left(\frac{V_1 V_2^3}{48} \frac{d^4 i_e}{dV^4} + \frac{V_1 V_2^3}{768} (2V_1^2 + V_2^2) \frac{d^6 i_e}{dV^6} + \dots \right) \times \cos[(\omega_1 \pm 3\omega_2)t] + \dots \\
&\approx \dots \mp \frac{V_1 V_2}{2} \cos[(\omega_1 \pm \omega_2)t] \frac{d^2 i_e}{dV^2} - \frac{V_1 V_2^2}{8} \sin[(\omega_1 \pm 2\omega_2)t] \frac{d^3 i_e}{dV^3} \\
&\quad \pm \frac{V_1 V_2^3}{48} \cos[(\omega_1 \pm 3\omega_2)t] \frac{d^4 i_e}{dV^4} + \dots,
\end{aligned} \tag{A.8}$$

where $i_{e, \omega_1 \pm \omega_2}$, $i_{e, \omega_1 \pm 2\omega_2}$, and $i_{e, \omega_1 \pm 3\omega_2}$ are the first, second and third sideband harmonics of the probe electron current, respectively. As shown in Equation (A.8), the second and higher order contributions to the sideband harmonics can be neglected if V_1 and V_2 are small. It is noted that the amplitudes of the sideband harmonics are expressed as the product of V_1 , V_2 and the derivatives of i_e . Thus, the terms on the right sides of Equation (A.5) and Equation (A.6) can be replaced by the expressions deduced from Equation (A.8):

$$\frac{d^3 i_e / dV^3}{dV^2} \approx \frac{4 |i_{e, \omega_1 \pm 2\omega_2}|}{V_2 |i_{e, \omega_1 \pm \omega_2}|} \quad (\text{A.9})$$

and

$$\frac{d^4 i_e / dV^4}{dV^2} - \left(\frac{d^3 i_e / dV^3}{dV^2} \right)^2 \approx \frac{24 |i_{e, \omega_1 \pm 3\omega_2}|}{V_2^2 |i_{e, \omega_1 \pm \omega_2}|} - \left[\frac{4 |i_{e, \omega_1 \pm 2\omega_2}|}{V_2 |i_{e, \omega_1 \pm \omega_2}|} \right]^2. \quad (\text{A.10})$$

Substituting Equations (A.2) and (A.3) to Equations (A.9) and (A.10) at the floating potential, V_f , the following two equations for the slope and curvature of the EEPF curve in a semi-logarithmic scale can finally be obtained:

$$\left(\frac{4 |i_{e, \omega_1 \pm 2\omega_2}|}{V_2 |i_{e, \omega_1 \pm \omega_2}|} \right) \Big|_{V=V_f} \approx c_2 x (V_p - V_f)^{x-1} \quad (\text{A.11})$$

and

$$\left(\frac{24 |i_{e, \omega_1 \pm 3\omega_2}|}{V_2^2 |i_{e, \omega_1 \pm \omega_2}|} - \left[\frac{4 |i_{e, \omega_1 \pm 2\omega_2}|}{V_2 |i_{e, \omega_1 \pm \omega_2}|} \right]^2 \right) \Big|_{V=V_f} \approx c_2 x (x-1) (V_p - V_f)^{x-2}. \quad (\text{A.12})$$

Here, the potential difference within the sheath between a plasma and a floating wall, $V_p - V_f$, can be numerically obtained from the next balance equation which represents that electron and ion fluxes are equal at the floating potential,

$$\frac{1}{4} \bar{v}_e c_1 \int_{V_p - V_f}^{\infty} (\varepsilon - (V_p - V_f))^{1/2} \exp(-c_2 \varepsilon^x) d\varepsilon = \left(\frac{3eT_{e, \text{eff}}}{m_i} \right)^{1/2} \frac{[\Gamma(\xi_1)]}{[\Gamma(\xi_2)\Gamma(\xi_3)]^{1/2}} \quad (\text{A.13})$$

where $\bar{v}_e = (3eT_{e, \text{eff}}/m_e)^{1/2} [\Gamma(\xi_4)^2 / \Gamma(\xi_1)\Gamma(\xi_2)]^{1/2}$ is the mean electron speed, m_i is the ion mass, $\xi_3 \equiv 1/(2x)$, and $\xi_4 \equiv 2/x$. $V_p - V_f$ can be also expressed in terms of x and $T_{e, \text{eff}}$ as shown in Equation (A.13). Therefore, two unknowns, x and $T_{e, \text{eff}}$, as the parameters to determine the EEPF shape can now be calculated by solving Equations (A.11) and (A.12) simultaneously if the amplitudes of $i_{e, \omega_1 \pm \omega_2}$, $i_{e, \omega_1 \pm 2\omega_2}$, and $i_{e, \omega_1 \pm 3\omega_2}$ at the floating

potential are given. It is noteworthy that this extended FHM can determine the parameters that characterize the whole EEPF shape including the non-Maxwellian EEPF with only information on the harmonics of the probe electron current at one point (i.e., the floating potential) by introducing the generalized EEPF formula and by interpreting the third sideband harmonics associated with the curvature of the EEPF curve. The calculation code using the built-in function, *fsolve*, in MATLAB R2013a (Mathworks Inc., Natick, MA, USA) has been developed to solve Equations (A.11) – (A.13).

Appendix B. Laser-assisted H_α spectroscopy for measurement of H^- ion density

A novel laser-assisted H_α spectroscopy for measurement of H^- ion density have been developed. The laser-induced photodetachment of H^- ions leads to the decrease in density of H ($n = 3$) atoms generated by the mutual neutralization, which results in reduced H_α intensity. From the reduced H_α intensity, H^- ion density can be measured quantitatively using the relation between reduced H_α intensity and H^- ion density.

Principles of measurement

Since H_α is a spectral line in the Balmer series emitted by an H atom when an electron in the atom transits from the $n = 3$ state to the $n = 2$ state, its intensity is closely related to the density of H ($n = 3$) atoms. Production processes for H ($n = 3$) atoms include the electron impact direct excitation of H atoms, recombination of H^+ ions, dissociative excitation of H_2 molecules, dissociative recombination of H_2^+ ions, and the mutual neutralizations by collisions of H^- ions with positive ions. [15, 154] Note that the variation of H^- ions causes the change in H_α intensity associated with the mutual neutralization. Using this principle, Ikeda *et al.* proposed H_α imaging spectroscopy which can diagnoses H^- ion behavior. [154, 155] They observed the spatial variation of H^- ions by measuring ΔH_α due to H^- ion beam extraction. Similar to the beam

extraction, the photodetachment induced by a laser beam can make a change of H^- ion density and then ΔH_α . When a laser beam is injected across a plasma chamber so that H^- ions in the laser path are photo-detached by the laser, the contribution of mutual neutralization to H_α intensity is lost. This principle of laser-assisted H_α spectroscopy is illustrated in Figure B.1.

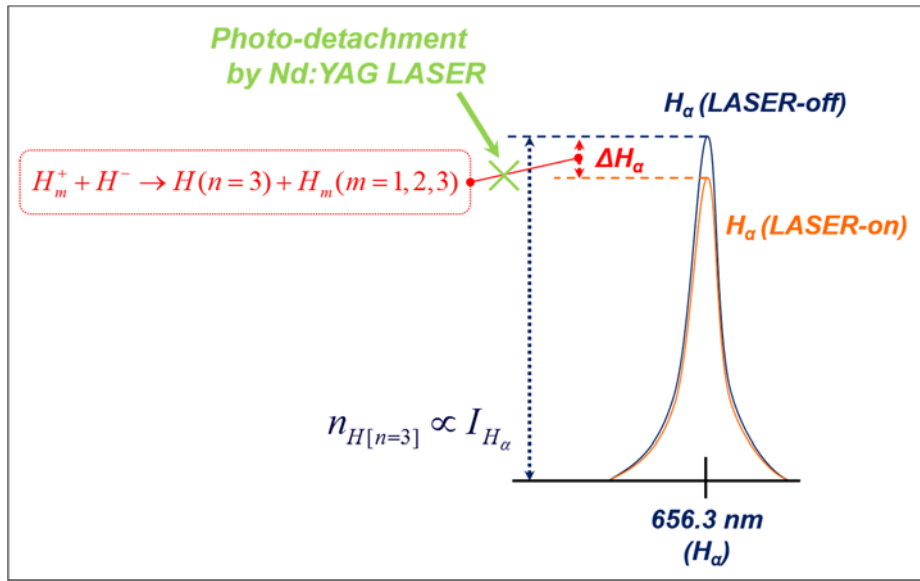


Figure B.1 Schematic diagram showing the principle of laser-assisted H_α spectroscopy.

For the lost $H(n=3)$ atoms by the nonoccurrence of the mutual neutralization owing to laser-induced photodetachment, a particle balance equation can be expressed as

$$\sum_{p < 3} \theta_{3p} A_{3p} \Delta n_{H(n=3)} = \sum_m (n_{H_m^+} n_{H^-} \langle \sigma_{MN, m} v \rangle), \quad (\text{B.1})$$

where θ_{3p} is the optical escape factor of the radiative transition from the $n=3$

state to the $n = p < 3$ state, A_{3p} is the radiative transition probability from the $n = 3$ state to the $n = p < 3$ state, $\Delta n_{H(n=3)}$ is the reduced density of H ($n = 3$) atoms by laser-induced photodetachment, $n_{H_m^+}$ is the hydrogen positive ion density for H_m^+ ($m = 1, 2$ and 3) ions, n_{H^-} is the H^- ion density, $\sigma_{MN, m}$ is the cross section of the mutual neutralization between H_m^+ ions and H^- ions which produces H ($n = 3$) atoms, v is the magnitude of the relative velocity, and the triangular brackets denote averaging over the distribution of v . The terms on the left- and right-hand sides of Equation (B.1) represent the radiative destruction and the generation (by the mutual neutralization) of H ($n = 3$) atoms, respectively. In this regard, there are two destruction mechanisms of H ($n = 3$) atoms, i.e., the radiative and collisional destructions. It is confirmed that the radiative destruction dominates in our experimental conditions by using global model analysis in which H ($n = 1-4$) atoms are included, and therefore only the radiative destruction is considered in Equation (B.1). For $H^+ - H^-$ mutual neutralization (i.e., $H^+ - H^- \rightarrow H(n=1) + H(n)$), the process into $H(n=1) + H(n=3)$ dominates over the entire energy range. [156, 157] Hence, total mutual neutralization cross section is approximately equal to one of the process into $H(n=1) + H(n=3)$. Unfortunately, the reaction mechanisms and cross sections on mutual neutralizations of H_2^+ ions and H_3^+ ions with H^- ions have not been investigated sufficiently, as compared to the $H^+ - H^-$ mutual neutralization. Moreover, $H_3^+ - H^-$ mutual neutralization has a complexity regarding predissociation channels of H_3 into $3 H$ and $H_2 + H$ (i.e., $H_3^+ - H^- \rightarrow H_2 + 2 H$ or $4 H$). [93] To calculate n_{H^-} using Equation (B.1), the following two assumptions were made: (1) All the mutual neutralizations make one H (n

= 3) atom; (2) $\sigma_{MN, m}$ is almost same to the total mutual neutralization cross section. The total cross section data were taken from Refs. 91, 93 and 156.

The relation between ΔH_α and $\Delta n_{H(n=3)}$ is given by

$$\Delta H_\alpha = C \theta_{32} A_{32} \Delta n_{H(n=3)}, \quad (\text{B.2})$$

where ΔH_α is the reduction in H_α intensity due to the laser-induced photodetachment and C is a constant which describes the characteristics of laser and optical emission spectroscopy (OES) system. The constant C contains sensitivities of OES, and spatial and temporal factors of measurement system. The sensitivities of OES are determined by the sensitivity of a charge-coupled device in the spectrometer and the transmission loss of H_α in the quartz windows and an OES fiber.

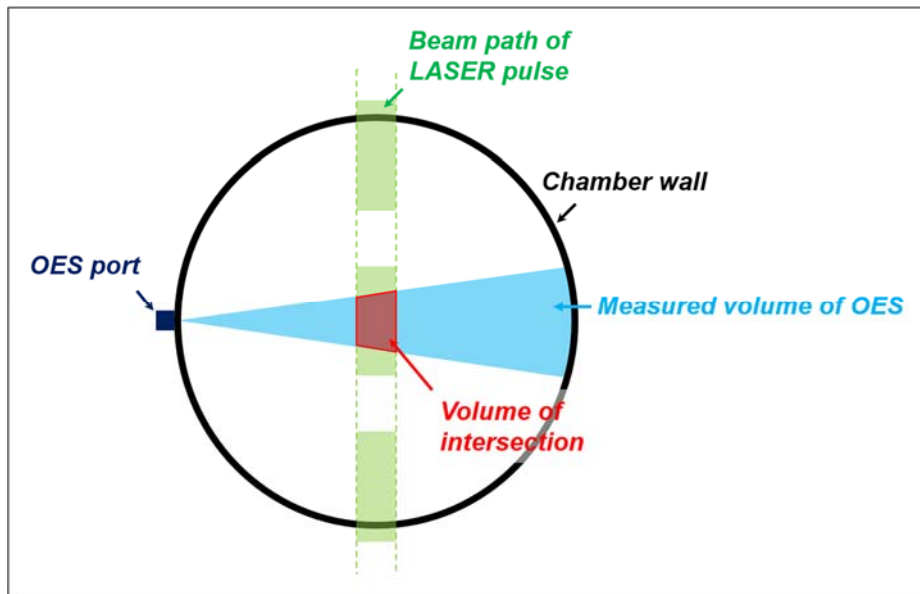


Figure B.2 Schematic diagram showing the definition of the spatial factor. (The blue region: V_{OES} , the red region: V_{int}).

As shown in Figure B.2, the spatial factor can be defined as the ratio of V_{int} to V_{OES} , where V_{OES} is the volume of the plasma region where OES can accept the emission light with a specific numerical aperture, and V_{int} is the intersection volume between V_{OES} and the volume where laser beam is injected across. The temporal factor denotes the ratio of total on-time of laser pulses during the integration time of OES (t_{OES}) to t_{OES} .

Substituting Equation (B.2) to Equation (B.1), the following Equation (B.3) on the relation between ΔH_α and n_{H^-} can be obtained:

$$\Delta H_\alpha = \frac{C \theta_{32} A_{32}}{\sum_{p < 3} \theta_{3p} A_{3p}} \sum_m (n_{H_m^+} n_{H^-} \langle \sigma_{MN, m} v \rangle). \quad (\text{B.3})$$

Since our experimental chamber (which will be presented in more detail below) is small, θ_{3p} is nearly one, and then the constants in Equation (B.3) can be rewritten as a constant K :

$$K \equiv C \frac{\theta_{32} A_{32}}{\sum_{p < 3} \theta_{3p} A_{3p}}. \quad (\text{B.4})$$

Bibliography

- [1] B. Anthony, L. Breaux, T. Hsu, S. Banerjee, and A. Tasch, *J. Vac. Sci. Technol.* **B7** 621 (1989).
- [2] R. P. H. Chang, C. C. Chang, and S. Darack, *J. Vac. Sci. Technol.* **20** 45 (1982).
- [3] P. K. Chu, S. Qin, C. Chan, N. W. Cheung, and L. A. Larson, *Materials Science and Engineering* **R17** 207 (1996).
- [4] U. Fantz, P. Franzen, W. Kraus, H. D. Falter, M. Berger, S. Christ-Koch, M. Fröschle, R. Gutser, B. Heinemann, C. Martens, P. McNeely, R. Riedl, E. Speth, and D. Wunderlich, *Rev. Sci. Instrum.* **79** 02A511 (2008).
- [5] M. Bacal, A. Hatayama, and J. Peters, *IEEE Trans. Plasma Sci.* **33**, No. 6, 1845 (2005).
- [6] B. Worf (ed), *Handbook of Ion Sources*, Boca Raton, FL: CRC Press, 1995.
- [7] R. S. Hemsworth and T. Inoue, *IEEE Trans. Plasma Sci.* **33**, No. 6, 1799 (2005).
- [8] W. Kraus, U. Fantz, P. Franzen, M. Fröschle, B. Heinemann, R. Riedl, and D. Wunderlich, *Rev. Sci. Instrum.* **83** 02B104 (2012).
- [9] P. Franzen, H. D. Falter, U. Fantz, W. Kraus, M. Berger, S. Christ-Koch, M. Fröschle, R. Gutser, B. Heinemann, S. Hilbert, S. Leyer, C. Martens, P. McNeely, R. Riedl, E. Speth, and D. Wunderlich, *Nucl. Fusion* **47** 264 (2007).
- [10] E. Speth and NBI Team, *Plasma Sci. Technol.* **6** 2135 (2004).

- [11] D. Riz and J. Paméla, *Rev. Sci. Instrum.* **69** 914 (1998).
- [12] J. Peters, *Rev. Sci. Instrum.* **71** 1069 (2000).
- [13] M. Bacal, *Rev. Sci. Instrum.* **79** 02A516 (2008).
- [14] F. Barnett, “Collisions of H, H₂, He and Li atoms and ions with atoms and molecules”, Oak Ridge National Laboratory Report ORNL-6086, 1990.
- [15] U. Fantz, H. Falter, P. Franzen, D. Wunderlich, M. Berger, A. Lorenz, W. Kraus, P. McNeely, R. Riedl, and E. Speth, *Nucl. Fusion* **46** S297 (2006).
- [16] U. Fantz, P. Franzen, W. Kraus, M. Berger, S. Christ-Koch, H. Falter, M. Fröschle, R. Gutser, B. Heinemann, C. Martens, P. McNeely, R. Riedl, E. Speth, A. Stäbler, and D. Wunderlich, *Nucl. Fusion* **49** 125007 (2009).
- [17] E. Speth, H. D. Falter, P. Franzen, U. Fantz, M. Bandyopadhyay, S. Christ, A. Encheva, M. Fröschle, D. Holtum, B. Heinemann, W. Kraus, A. Lorenz, Ch. Martens, P. McNeely, S. Obermayer, R. Riedl, R. Süß, A. Tanga, R. Wilhelm, and D. Wunderlich, *Nucl. Fusion* **46** S220 (2006).
- [18] A. Stäbler, U. Fantz, P. Franzen, M. Berger, S. Christ-Koch, H. D. Falter, M. Fröschle, R. Gutser, B. Heinemann, D. Holtum, W. Kraus, C. Martens, P. McNeely, R. Nocentini, S. Obermayer, R. Riedl, E. Speth, and D. Wunderlich, *Fusion Eng. Des.* **84** 265 (2009).
- [19] P. Franzen, U. Fantz, *Fusion Eng. Des.* **89** 2594 (2014).
- [20] R. Nocentini, U. Fantz, P. Franzen, M. Fröschle, B. Heinemann, R. Riedl, and the NNBI-Team, *IEEE Trans. Plasma Sci.* **42**, No. 3, 616 (2014).
- [21] P. McNeely, S. V. Dudin, S. Christ-Koch, U. Fantz, and the NNBI Team, *Plasma Sources Sci. Technol.* **18** 014011 (2009).
- [22] M. Bacal, *Nucl. Fusion* **46** S250 (2006).

- [23] J. R. Hiskes, A. M. Karo, and P. A. Willmann, *J. Vac. Sci. Technol. A* **3** 1229 (1985).
- [24] J. R. Hiskes, *Appl. Phys. Lett.* **57** 231 (1990).
- [25] M. Bacal, *Chem. Phys.* **398** 3 (2012).
- [26] Y. Takeiri, *Rev. Sci. Instrum.* **81** 02B114 (2010).
- [27] St. Kolev, G. J. M. Hagelaar, G. Fubiani, and J. P. Boeuf, *Plasma Sources Sci. Technol.* **21** 025002 (2012).
- [28] J. P. Boeuf, B. Chaudhury, and L. Garrigues, *Phys. Plasmas* **19** 113509 (2012).
- [29] J. P. Boeuf, J. Claustre, B. Chaudhury, and G. Fubiani, *Phys. Plasmas* **19** 113510 (2012).
- [30] H. G. Demars and R. W. Schunk, *J. Phys. D: Appl. Phys.* **12** 1051 (1979).
- [31] U. Kortshagen, C. Busch, and L. D. Tsendin, *Plasma Sources Sci. Technol.* **5** 1 (1996).
- [32] G. J. M. Hagelaar and L. C. Pitchford, *Plasma Sources Sci. Technol.* **14** 722 (2005).
- [33] M. A. Lieberman and A. J. Lichtenberg, *Principles of Plasma Discharges and Materials Processing*, 2nd ed. New York, NY, USA: Wiley, 2005.
- [34] V. A. Godyak, *IEEE Trans. Plasma Sci.* **34**, No. 3, 755 (2006).
- [35] V. A. Godyak and V. I. Demidov, *J. Phys. D: Appl. Phys.* **44** 233001 (2011).
- [36] J. T. Gudmundsson, *Plasma Sources Sci. Technol.* **10** 76 (2001).
- [37] P. Chabert and N. S. J. Braithwaite, *Physics of Radio-Frequency Plasmas*, Cambridge University Press, 2011.
- [38] F. F. Chen, "Capacitor tuning circuits for inductive loads", UCLA Report

- PPG-1401, 1992.
- [39] M. A. Lieberman and V. A. Godyak, IEEE Trans. Plasma Sci. **26**, No. 3, 955 (1998).
- [40] M. M. Turner, J. Phys. D: Appl. Phys. **42** 194008 (2009).
- [41] V. A. Godyak, R. B. Piejak, and B. M. Alexandrovich, Plasma Sources Sci. Technol. **11** 525 (2002).
- [42] Y. An, W. Cho, K.-J. Chung, K. Lee, S. Jang, S.-G. Lee, and Y. S. Hwang, Rev. Sci. Instrum. **83** 02A727 (2012).
- [43] J. Peters, AIP Conf. Proc. **763** 214 (2005).
- [44] V. A. Godyak, R. B. Piejak, and B. M. Alexandrovich, Phys. Rev. Lett. **80**, No. 15, 3264 (1998).
- [45] V. A. Godyak, Phys. Plasmas **12** 055501 (2005).
- [46] S. Banna, A. Agarwal, G. Cunge, M. Darnon, E. Pargon, and O. Joubert, J. Vac. Sci. Technol. A **30** 040801 (2012).
- [47] S. Linnane and M. B. Hopkins, Plasma Sources Sci. Technol. **18** 045017 (2009).
- [48] N. Hershkowitz, in O. Auciello and D. L. Flamm (Eds.), *Plasma Diagnostics, Volume 1: Discharge Parameters and Chemistry*, Academic Press, New York, 1989, Chapter 3.
- [49] F. Magnus and J. T. Gudmundsson, Rev. Sci. Instrum. **79** 073503 (2008).
- [50] I. D. Sudit and F. F. Chen, Plasma Sources Sci. Technol. **3** 162 (1994).
- [51] T. E. Sheridan and M. A. Hayes, Rev. Sci. Instrum. **59** 1081 (1988).
- [52] M. Bacal, Plasma Sources Sci. Technol. **2** 190 (1993).
- [53] M. Bacal, Rev. Sci. Instrum. **71** 3981 (2000).

- [54] D. D. Monahan and M. M. Turner, *Plasma Sources Sci. Technol.* **18** 045024 (2009).
- [55] R. Zorat, J. Goss, D. Boilson, and D. Vender, *Plasma Sources Sci. Technol.* **9** 161 (2000).
- [56] R. Zorat and D. Vender, *J. Phys. D: Appl. Phys.* **33** 1728 (2000).
- [57] T. Kimura and H. Kasugai, *J. Appl. Phys.* **107** 083308 (2010).
- [58] A. T. Hjartarson, E. G. Thorsteinsson, and J. T. Gudmundsson, *Plasma Sources Sci. Technol.* **19** 065008 (2010).
- [59] D. Pagano, C. Gorse, and M. Capitelli, *IEEE Trans. Plasma Sci.* **35**, No. 5, 1247 (2007).
- [60] F. Taccogna, R. Schneider, S. Longo, and M. Capitelli, *Phys. Plasmas* **14** 073503 (2007).
- [61] F. Taccogna, R. Schneider, S. Longo, and M. Capitelli, *Phys. Plasmas* **15** 103502 (2008).
- [62] Ts. Paunskaa, H. Schlüter, A. Shivarova, and Kh. Tarnev, *Phys. Plasmas* **13** 023504 (2006).
- [63] G. J. M. Hagelaar, G. Fubiani, and J. P. Boeuf, *Plasma Sources Sci. Technol.* **20** 015001 (2011).
- [64] J. P. Boeuf, G. J. M. Hagelaar, P. Sarrailh, G. Fubiani, and N. Kohen, *Plasma Sources Sci. Technol.* **20** 015002 (2011).
- [65] J. Sun, X. Li, C. Sang, W. Jiang, P. Zhang, and D. Wang, *Phys. Plasmas* **17** 103505 (2010).
- [66] E. Chacon-Golcher and K. J. Bowers, *Commun. Comput. Phys.* **4** 659 (2008).

- [67] T. Kimura and K. Ohe, *J. Appl. Phys.* **89**, No. 8, 4240 (2001).
- [68] N. Kang, F. Gaboriau, and S.-G. Oh, *J. Appl. Phys.* **112** 103303 (2012).
- [69] J. T. Gudmundsson, A. T. Hjartarson, and E. G. Thorsteinsson, *Vacuum* **86** 808 (2012).
- [70] IAEA AMDIS ALADDIN database: <http://www-amdis.iaea.org/ALADDIN/>
- [71] I. Bray and A. T. Stelbovics, *Adv. At., Mol., Opt. Phys.* **35** 209 (1995).
- [72] R. K. Janev and J. J. Smith, *Atomic and plasma-material interaction data for fusion Vol. 4*, International atomic energy agency, Vienna, 1993.
- [73] R. K. Janev, W. D. Langer, K. Evans Jr. and D. E. Post Jr., *Elementary processes in hydrogen-helium plasmas*, Springer, Berlin, 1987.
- [74] R. K. Janev, D. Reiter, and U. Samm, “Collision processes in low-temperature hydrogen plasmas”, Forschungszentrum Jülich Report JUEL 4105, 2003.
- [75] R. J. Bieniek, *J. Phys. B: At. Mol. Phys.* **13** 4405 (1980).
- [76] J. S. Yoon, M. Y. Song, J. M. Han, S. H. Hwang, W. S. Chang, B. J. Lee, and Y. Itikawa, *J. Phys. Chem. Ref. Data* **37**, No. 2, 913 (2008).
- [77] V. A. Shakhatov and Yu. A. Lebedev, *High Temp.* **49**, No. 2, 257 (2011).
- [78] M. Allan, *J. Phys. B: At. Mol. Phys.* **18** L451 (1985).
- [79] U. Fantz and D. Wunderlich, *Atomic Data and Nuclear Data Tables* **92** 853 (2006).
- [80] H. Gao, *Phys. Rev. A* **45**, No.9, 6895 (1992).
- [81] M. Capitelli, R. Celiberto, F. Esposito, A. Laricchiuta, K. Hassouni, and S. Longo, *Plasma Sources Sci. Technol.* **11** A7 (2002).

- [82] J. Horáček, M. Čížek, K. Houfek, P. Kolorenč, and W. Domcke, *Phys. Rev. A* **73** 022701 (2006).
- [83] R. Celiberto, A. Laricchiuta, M. Capitelli, R.K. Janev, J. Wadehra, and D.E. Atems, “Cross section data for electron-impact inelastic processes of vibrationally excited hydrogen molecules and their isotopes”, International atomic energy agency, International nuclear data committee Report INDC(NDS)-397, 1999.
- [84] R. Celiberto, R. K. Janev, A. Laricchiuta, M. Capitelli, J. M. Wadehra, and D. E. Atems, *At. Data Nucl. Data Tables* **77**, No.2, 161 (2001).
- [85] R. Celiberto, M. Capitelli, and A. Laricchiuta, *Phys. Scr.* **T96** 32 (2002).
- [86] D. Wunderlich and U. Fantz, *At. Data Nucl. Data Tables* **97** 152 (2011).
- [87] P. S. Krstić, *Phys. Rev. A* **66** 042717 (2002).
- [88] H. Tawara, Y. Itikawa, H. Nishimura, and M. Yoshino, *J. Phys. Chem. Ref. Data* **19**, No. 3, 617 (1990).
- [89] M. J. J. Eerden, M. C. M. van de Sanden, D. K. Otorbaev, and D. C. Schram, *Phys. Rev. A* **51**, No. 4, 3362 (1995).
- [90] T. Mosbach, *Plasma Sources Sci. Technol.* **14** 351 (2005).
- [91] C. L. Liu, J. G. Wang, and R. K. Janev, *Adv. At., Mol., Opt. Phys.* **39** 1223 (2006).
- [92] I. F. Schneider and A. E. Orel, *J. Chem. Phys.* **111**, No. 13, 5873 (1999).
- [93] R. K. Janev, C. L. Liu, J. G. Wang, and J. Yan, *Europhys. Lett.* **74** (4) 616 (2006).
- [94] W. Biel, M. Bröse, M. David, H. Kempkens, and J. Uhlenbusch, *Plasma Phys. Control. Fusion* **39** 661 (1997).

- [95] M. E. Mandy and P. G. Martin, *J. Chem. Phys.* **110** 7811 (1999).
- [96] A. A. Matveyev and V. P. Silakov, *Plasma Sources Sci. Technol.* **4** 606 (1995).
- [97] M. Green, K. R. Jennings, J. W. Linnett, and D. Schofield, *Trans. Faraday Soc.* **55** 2152 (1959).
- [98] B. J. Wood and H. Wise, *J. Phys. Chem.* **66** 1049 (1962).
- [99] Y. Abe, A. Fukushima, K. Takeda, H. Kondo, K. Ishikawa, M. Sekine, and M. Hori, *J. Appl. Phys.* **113** 013303 (2013).
- [100] ⁶¹Y. Abe, K. Takeda, K. Ishikawa, H. Kondo, M. Sekine, and M. Hori, in *Measurement of surface loss probabilities of hydrogen radicals in plasma-enhanced Si CVD process for solar cell 2010: Proceedings of the 63rd Annual Gaseous Electronics Conference and 7th International Conference on Reactive Plasmas*, Paris, France, 4–8 October 2010, p. 160.
- [101] J. R. Hiskes and A. M. Karo, *Appl. Phys. Lett.* **54** (6) 508 (1989).
- [102] F. Taccogna, S. Longo, M. Capitelli, and R. Schneider, *IEEE Trans. Plasma Sci.* **36**, No. 4, 1589 (2008).
- [103] R. S. Devoto and J. D. Hanson, “SIGV - a code to evaluate plasma reaction rates to a specified accuracy”, California University, Lawrence Livermore Laboratory Report UCRL-52559, 1978.
- [104] V. Rat, P. André, J. Aubreton, M. F. Elchinger, P. Fauchais, and D. Vacher, *J. Phys. D: Appl. Phys.* **35** 981 (2002).
- [105] J. R. Stallcop, E. Levin, and H. Partridge, *J. Thermophys. Heat Transfer* **12** 514 (1998).

- [106] J. R. Stallcop, H. Partridge, and E. Levin, *Chem. Phys. Lett.* **254** 25 (1996).
- [107] N. Hershkowitz, C. S. Yip, and G. D. Severn, *Phys. Plasmas* **18** 057102 (2011).
- [108] N. Hershkowitz, G. D. Severn, S. D. Baalrud, C. C. Hegna, and J. D. Callen, *Phys. Rev. Lett.* **108** 139501 (2012).
- [109] D. Lee, G. Severn, L. Oksuz, and N. Hershkowitz, *J. Phys. D: Appl. Phys.* **39** 5230 (2006).
- [110] G. D. Severn, C. S. Yip, and N. Hershkowitz, *JINST* **8** C11020 (2013).
- [111] H. Amemiya, *J. Phys. Soc. Japan* **67**, No. 6, 1955 (1998).
- [112] N. St. J. Braithwaite and J. E. Allen, *J. Phys. D: Appl. Phys.* **21** 1733 (1988).
- [113] N. Hershkowitz, K. N. Leung, and T. Romesser, *Phys. Rev. Lett.* **35**, No. 5, 277 (1975).
- [114] D. D. Monahan and M. M. Turner, *Phys. Plasmas* **17** 045003 (2008).
- [115] S. Kim, M. A. Lieberman, A. J. Lichtenberg, and J. T. Gudmundsson, *J. Vac. Sci. Technol. A* **24** 2025 (2006).
- [116] C. Lee and M. A. Lieberman, *J. Vac. Sci. Technol. A* **13** 368 (1995).
- [117] J. E. Allen, *Plasma Sources Sci. Technol.* **13** 48 (2004).
- [118] J. I. Fernández Palop, J. Ballesteros, M. A. Hernández, and R. Morales Crespo, *Plasma Sources Sci. Technol.* **16** S76 (2007).
- [119] J. E. Allen, *Plasma Sources Sci. Technol.* **18** 014004 (2009).
- [120] V. Vahedi, M. A. Lieberman, G. DiPeso, T. D. Rognlien, and D. Hewett, *J. Appl. Phys.* **78** 1446 (1995).

- [121] F. F. Chen, *Introduction to Plasma Physics and Controlled Fusion, Volume 1*, 2nd ed. New York: Plenum Press, 1984.
- [122] J. D. Huba, NRL plasma formulary, NRL/PU/6790--07-500 (Washington, DC: Naval Research Laboratory), 2007.
- [123] B. K. Jung, J. J. Dang, Y. H. An, K. J. Chung, and Y. S. Hwang, *Rev. Sci. Instrum.* **85** 02B112 (2014).
- [124] K. J. Chung, B. K. Jung, Y. H. An, J. J. Dang, and Y. S. Hwang, *Rev. Sci. Instrum.* **85** 02B119 (2014).
- [125] J. Y. Bang and C. W. Chung, *Phys. Plasmas* **16** 093502 (2009).
- [126] H. C. Lee, M. H. Lee, and C. W. Chung, *Appl. Phys. Lett.* **96** 041503 (2010).
- [127] S. H. Seo, J. I. Hong, and H. Y. Chang, *Appl. Phys. Lett.* **74** 2776 (1999).
- [128] C. W. Chung and H. Y. Chang, *Appl. Phys. Lett.* **80** 1725 (2002).
- [129] M. H. Lee, H. C. Lee, and C. W. Chung, *Appl. Phys. Lett.* **93** 231503 (2008).
- [130] V. A. Godyak, R. B. Piejak, and B. M. Alexandrovich, *J. Appl. Phys.* **73** 3657 (1993).
- [131] M. Kronberger, D. K uchler, J. Lettry, Ø. Midttun, M. O’Neil, M. Paoluzzi, and R. Scrivens, *Rev. Sci. Instrum.* **81** 02A708 (2010).
- [132] R. F. Welton, J. Carmichael, N. J. Desai, R. Fuga, R. H. Goulding, B. Han, Y. Kang, S. W. Lee, S. N. Murray, T. Pennisi, K. G. Potter, M. Santana, and M. P. Stockli, *Rev. Sci. Instrum.* **81** 02A727 (2010).
- [133] R. B. Piejak and V. A. Godyak, and B. M. Alexandrovich, *Plasma Sources Sci. Technol.* **1** 179 (1992).

- [134] K. Suzuki, K. Nakamura, H. Ohkubo, and H. Sugai, *Plasma Sources Sci. Technol.* **7** 13 (1998).
- [135] V. A. Godyak, R. B. Piejak, and B. M. Alexandrovich, *J. Appl. Phys.* **85** 3081 (1999).
- [136] J. T. Gudmundsson and M. A. Lieberman, *Plasma Sources Sci. Technol.* **6** 540 (1997).
- [137] J. T. Gudmundsson and M. A. Lieberman, *Plasma Sources Sci. Technol.* **7** 83 (1998).
- [138] U. Fantz, P. Franzen, and D. Wunderlich, *Chem. Phys.* **398** 7 (2012).
- [139] C. Gorse, M. Capitelli, M. Bacal, J. Bretagne, and A. Laganà, *Chem. Phys.* **117** 177 (1987).
- [140] M. B. Hopkins and K. N. Mellon, *Phys. Rev. Lett.* **67**, No. 4, 449 (1991).
- [141] M. B. Hopkins, M. Bacal and W. G. Graham, *J. Appl. Phys.* **70** (4) 2009 (1991).
- [142] C. Gorse and M. Capitelli, *Phys. Rev. A* **46** No. 4, 2176 (1992).
- [143] C. Michaut, M. Bacal, Yu. I. Belchenko, J. Auvray, C. Konieczny, and J. P. Stephan, *Rev. Sci. Instrum.* **65** 1207 (1994).
- [144] O. Fukumasa and M. Shinoda, *Rev. Sci. Instrum.* **69**, No. 2, 938 (1998).
- [145] T. Mosbach, H.-M. Katsch, and H. F. Döbele, *Plasma Sources Sci. Technol.* **7** 75 (1998).
- [146] M. Capitelli and C. Gorse, *IEEE Trans. Plasma Sci.* **33**, No. 6, 1832 (2005).
- [147] P. Diomede, S. Longo, and M. Capitelli, *Phys. Plasmas* **13** 113505 (2006).
- [148] M. Capitelli, M. Cacciatore, R. Celiberto, O. De Pascale, P. Diomede, F.

- Esposito, A. Gicquel, C. Gorse, K. Hassouni, A. Laricchiuta, S. Longo, D. Pagano and M. Rutigliano, Nucl. Fusion **46** S260 (2006).
- [149] P. Diomede, S. Longo, D. J. Economou, and M. Capitelli, J. Phys. D: Appl. Phys. **45** 175204 (2012).
- [150] A. Maresca, K. Orlov, and U. Kortshagen, Phys. Rev. E **65** 056405 (2002).
- [151] S.-H. Seo and H.-Y. Chang, J. Korean Phys. Soc. **48**, No. 3, 414 (2006).
- [152] J. Y. Bang, A. Kim, and C. W. Chung, J. Appl. Phys. **107** 103312 (2010).
- [153] S. H. Jang, G. H. Kim, C. W. Chung, Thin Solid Films **519** 7042 (2011).
- [154] K. Ikeda, H. Nakano, K. Tsumori, M. Kasaki, K. Nagaoka, M. Osakabe, Y. Takeiri and O. Kaneko, Plasma Fusion Res. **8** 1301036 (2013).
- [155] K. Ikeda, H. Nakano, K. Tsumori, M. Kasaki, K. Nagaoka, M. Osakabe, Y. Takeiri, and O. Kaneko, New Journal of Physics **15** 103026 (2013).
- [156] D. Fussen and C. Kubach, J. Phys. B: At. Mol. Phys. **19** L31 (1986).
- [157] M. Stenrup, Å. Larson and N. Elander, Phys. Rev. A **79** 012713 (2009).

초 록

핵융합 분야 및 산업 플라즈마에서 요구되는 더 효율적인 RF 수소 음이온원 개발을 위해서는 반드시 수소 플라즈마 내 화학 반응 및 유도 결합형 플라즈마에 대한 근본적인 물리 이해가 필수적이다. 저압 RF 수소 음이온원 플라즈마 내에서 대부분 반응은 전자 충돌 반응이며, 음이온 생성 및 소멸 관련 반응의 충돌 단면적은 전자 에너지에 대한 특이성을 갖기 때문에 본 연구는 전자 에너지 분포 함수를 바탕으로 수소 유도 결합형 플라즈마 내 음이온 생성 반응 특성을 연구하였다.

전자 에너지 분포 함수와 음이온 밀도간의 상관 관계를 분석하기 위하여 비 Maxwellian 전자 에너지 분포 함수 하에서 수소 내 다양한 종의 입자 밀도와 전자 온도를 계산할 수 있는 수소 플라즈마 글로벌 모델을 개발하였다. 저압 조건에서 나타나는 bi-Maxwellian 전자 에너지 분포는 Maxwellian 전자 에너지 분포의 전자 온도에 비해 더 높은 온도의 전자군과 더 낮은 온도의 전자군으로 구성되어 있다. 고온 전자군은 Maxwellian 전자 에너지 분포의 전자들보다 수소 분자와의 진동 여기 반응에 의해 높은 진동 양자 수의 여기 수소 분자들을 효율적으로 만든다. Bi-Maxwellian 플라즈마 내 고밀도의 높은 진동 양자 수 여기 수소 분자와 저온 전자군은 해리 전자 부착 반응을 크게 증가시켜 많은 음이온을 만든다. 수소 플라즈마 글로벌 모델 분석으로, bi-Maxwellian 전자 에너지 분포의 플라즈마가 Maxwellian 전자 에너지

분포의 플라즈마보다 음이온 생성 반응에 유리함을 밝혀냈고, 실험적으로 확인하였다.

음이온 생성에 유리한 bi-Maxwellization 현상은 주로 운전 압력을 낮추어 만들 수 있는데 운전 압력은 보통 음이온원의 빔인출 조건에 의하여 제한된다. 유도 결합형 플라즈마의 가열에 대한 이해를 바탕으로 bi-Maxwellization을 강화할 수 있는 이중 주파수 안테나 유도 결합형 플라즈마 장치를 제작하였다. 장치는 각각 2 MHz 그리고 13.56 MHz, 서로 다른 주파수의 두 안테나로 구성되어 있다. 이중 주파수 안테나 유도 결합형 플라즈마는 기존 단일 주파수 안테나 유도 결합형 플라즈마에 비해 두 가지 다른 플라즈마 특성을 보인다. 첫째, 이중 주파수 안테나 유도 결합형 플라즈마의 플라즈마 흡수 전력은 단일 주파수 안테나 유도 결합형 플라즈마의 플라즈마 흡수 전력보다 높다. 플라즈마 흡수 전력의 상승으로 같은 인가 전력에 대하여 이중 주파수 안테나 유도 결합형 플라즈마 장치의 밀도는 단일 주파수 안테나 유도 결합형 플라즈마의 밀도보다 높다. 둘째, 이중 주파수 안테나 유도 결합형 플라즈마의 고밀도 조건에서 13.56 MHz 전력에 의한 비충돌성 가열로 Maxwellization 구현이 가능하다. 실험 및 분석 결과, 13.56 MHz 전력이 증가할수록 전자 에너지 분포 함수가 Maxwellian 전자 에너지 분포 함수에서 bi-Maxwellian 전자 에너지 분포 함수로 천이함이 밝혀졌다. 이중 주파수 안테나 유도 결합형 플라즈마의 bi-Maxwellization으로 음이온 밀도는 약 30% 정도 증가하였다.

플라즈마 공간 내 음이온 생성은 전력 펄스 조절로 더욱 증대될 수 있다. 측정된 시간 미분 전자 에너지 분포 함수 그래프를

바탕으로 펄스 운전의 음이온 생성을 측정하고 분석하였다. 전력 인가가 중단된 after-glow 영역에서 전자 에너지 분포 함수 내 고온 전자군은 급격히 감소하며, 3 eV 이내 저온 전자군은 오히려 급격히 증가하였다. 이는 확산성 전자 냉각과 충돌성 전자 냉각 때문이며, 여기 수소 분자의 긴 생존 시간과 더불어 after-glow 영역에서 해리 전자 부착 반응을 제고한다. 실험을 통해 전력 펄스 조절 전보다 약 17배 정도 증가된 음이온 밀도를 관찰하였다. 마지막으로 active-glow 및 after-glow 특성 시간을 분석하여 평균 음이온 밀도가 최대가 되는 최적 전력 펄스 조건을 도출하였다.

본 수소 유도 결합형 플라즈마에 대한 기초 연구는 효율적인 RF 수소 음이온원 개발에 활용될 수 있을 뿐만 아니라, 다른 이원자 분자 (N_2 , O_2 , Cl_2 등)와 수소 간 유사성에 의거하여 이원자 분자를 사용하는 플라즈마 응용에도 기여할 수 있을 것으로 기대한다.

주요어: 수소, 플라즈마, 유도 결합형 플라즈마, 음이온, 펄스,
전자 에너지 분포 함수

학 번: 2009-30262